Numerical Analysis of the Thermal Performance of Energy Diaphragm Walls

Rúben André Matos Sirgado

Thesis to obtain the Master of Science Degree in

Civil Engineering

Supervisors: Prof. Dr. Peter John Bourne-Webb
Prof. Dr. Teresa Maria Bodas de Araújo Freitas

Examination Committee

Chairperson: Prof. Dr. Rui Pedro Carrilho Gomes
Supervisor: Prof. Dr. Peter John Bourne-Webb
Member of the Committee: Prof. Dr. Jaime Alberto dos Santos

March 2022

Declaration

I declare that this document is an original work of my own authorship and that it fulfills all the requirements of the Code of Conduct and Good Practices of the Universidade de Lisboa.

Acknowledgments

I would like to thank to my supervisors: Prof. Peter Bourne-Webb and Prof. Teresa Freitas for their constant inspiration, enthusiasm and support. Their experience and knowledge always inspired me to think, question and seek for perfection through our discussions. I am deeply grateful to be able to work in this demanding subject and to be advised by two of the best in the field. I will take that for life.

This work would not have been possible without DHI, for providing an educational license for the MIKE Powered by DHI Software FEFLOW, that allowed me to perform the numerical analysis presented in this thesis.

I would also like to thank to the Department of Civil Engineering and Foundation for Science and Technology for the scholarship for this research, the financial support is greatly appreciated.

I would like to thank to my beloved TUIST - Tuna Universitária do Instituto Superior Técnico, for the teaching and providing good moments that helped me grow as a person.

To my friends and housemates Mário Oliveira and Eduardo Nogueira, for the fellowship and support throughout all these years. To João Sousa, Vicente Pinto and João Ramalho for the companionship, music and trust over these years. To Miguel Mendes, João Leal, João Soares and to all my friends that i made along the way, and contributed to make my six years in Técnico one of the best times of my life.

Lastly, i would like to thank to Raquel for all the love, support and caring. To my parents António and Justina, sister Tatiana and brother in law Maarten for investing and never giving up on me. To all of you i apologize if I haven't been the person that you deserve. But I want you to know, in my way, I love you all.

Abstract

The use of the energy stored inside the earth, know as low-enthalpy geothermal energy is increasing due to the global energy demand and need to decrease the consumption of fossil fuels. The exploitation of this renewable energy occurs with the help of ground source energy systems, within which underground structures such as, energy piles, tunnel linings or energy walls can be utilised. These geostructures are equipped with heat exchanger pipes with a circulating fluid that allows heat exchange with the ground. Studies relating to the use of energy walls are scarce due to their complexity and numerical demand. Using the finite element software FEFLOW, several three-dimensional thermal analyses were performed and compared to existing numerical and field studies to understand the software viability. Subsequently, a parametric study was performed to analyse the thermal impact of the mesh, heat exchanger layout, thermal conductivity of the soil, thermal conductivity of the wall and the geometry of the wall. The findings present that walls with greater exposure to the excavated space present greater heat transfer rate, followed by thermal conductivity of the soil and wall.

Keywords

Energy walls; geothermal energy; renewable energy; finite element analysis; heat exchangers;

Resumo

A utilização da energia armazenada dentro da terra, mais conhecida como energia geotérmica de baixa entalpia tem aumentado devido á exigência de mais energia e necessidade de diminuir o consumo de combustíveis fosseis. A extração desta energia renovável ocorre através de sistemas de bombas de calor geotérmicas incorporados em estruturas subterrâneas como por exemplo, estacas termo-ativas, túneis ou paredes termo-ativas. Estas estruturas geotécnicas são equipadas com tubos que possuem um fluido que permite troca de calor com o solo. Vários estudos mencionam que o uso de paredes termo-ativas é escasso devido á sua complexidade e exigência numérica. Utilizando o programa de elementos finitos FEFLOW, várias analises tridimensionais foram executadas e comparadas com estudos numéricos e campo existentes de modo a compreender a viabilidade do programa. De seguida, um estudo paramétrico foi desenvolvido de modo a analisar o impacte térmico provocado pela malha, configuração dos tubos, condutividade térmica do solo, condutividade térmica da parede e geometria da parede. Os resultados obtidos apresentam que paredes com maior exposição para o espaço escavado apresentam maior transferência de calor seguidas pela condutividade térmica do solo e parede.

Palavras Chave

Paredes termo-ativas; energia geotérmica; energia renovável; análises de elementos finitos; bombas de calor;

Contents

List of Figures

List of Tables

Acronyms

1D	One-dimensional
2D	Two-dimensional
3D	Three-dimensional
CFA	Continuous flight auger
DGE	deep geothermal energy
FEA	Finite element analyses
GSES	Ground Source Energy Systems
GSHP	Ground source heat pump
HDPE	High-density polyethylene pipes
NHF	No heat flux
SGE	Shallow geothermal energy

Nomenclature

α_L	Longitudinal dispersivity
α_T	Transversal dispersivity
η	Soil porosity
λ_{conc}	concrete thermal conductivity
λ_{fluid}	Fluid thermal conductivity
λ_{soil}	Soil thermal conductivity
ρ	Bulk density
ρ_1	Bulk density of soil
ρ_2	Bulk density of fluid
ρ_3	Bulk density of air
ρ_{fluid}	Fluid density
ρ_{soil}	Solid phase density
A	Cross sectional area
A_w	Total wall surface area on the retained soil side
C	Concrete cover
c	Specific heat capacity
c_1	Specific heat capacity of the soil
c_2	Specific heat capacity of the water
c_3	Specific heat capacity of the air

c_w	Water specific heat capacity
cp	Heat capacity
d_i	Pipe inner diameter
d_o	Pipe outer diameter
G_s	Solid particle density
k_r	Horizontal hydraulic conductivity
k_{xx}	Horizontal hydraulic conductivity
k_{yy}	Vertical hydraulic conductivity
k_{zz}	Horizontal hydraulic conductivity
L	Pipe length
m	Mass flow rate
n	Porosity
Q	Fluid flow rate
q_L	Heat transfer rate per meter of pipe
R	Wall to excavation depth ratio
S	Specific storage coefficient
S_1	Saturation ratio for full saturation
S_L	Longitudinal spacing between pipe branches
S_r	Saturation ratio
T_{bot}	Porosity
$T_{farfield}$	Porosity
T_{in}	Porosity
T_{out}	Outlet temperature
T_o	Undisturbed ground temperature
T_{soil}	Soil temperature

T_{top}	Porosity
T_w	Wall temperature
V	Total volume of soil
v	Fluid velocity
V_v	Volume of voids
w	Water content

Chapter 1

Introduction

1.1 Overview

In recent decades, we have seen an increase in global energy demand caused by the growth of the world's population and due to the pursuit of a better quality of life. To fulfill this demand the consumption of fossil fuels in the last forty years doubled, and since these fuels have a negative impact on the environment, there is the need to find a more environmentally sustainable energy sources. For the long term, the use of renewable resources has been an option, thanks to the fact that they can be replaced at the same rate at which the resource is used. As a result, to replace this energy the use of the heat stored in the ground most commonly known as shallow geothermal energy, if adequately managed, can be a viable source to replace the non-ecological energies.

Geothermal energy can be divided into two different categories, Shallow geothermal energy (SGE), and deep geothermal energy (DGE). The later, is characterized for higher depths and temperature gradients, which allows generation of electric power. However the costs of extraction are substantially higher when compared to the SGE. The SGE plays an important role since it can be found in a range of depths of lesser than 300 m and can be deployed almost anywhere. That makes it an accessible source that is always available to extract, weather and time of the day do not influence this availability.

SGE is exploited with the help of Ground Source Energy Systems (GSES), which can be classified as closed-loop or open-loop. Open-loop systems is extract energy directly from the groundwater, while in closed-loop systems heat extraction is made through pipes in contact with in the ground. These pipes have a circulating fluid with lower temperature than the ground, which allows energy extraction to provide heating. There is also the possibility to inject heat into the ground, if the temperature of the circulating fluid is higher than the soil temperature, to provide cooling.

This thesis is focused on closed-loop systems incorporated in energy geostructures. These structures consist of underground structures such as energy piles, energy tunnels and energy walls. In the recent decades a considerable number of tests and projects were designed for energy piles, that makes it most used and installed energy geostructure around the world, when compared with the other types of energy geostructure. However, in recent years the interest in energy walls have seen a significant increase Laloui and Loria (2019), both in numerical studies and cumulative number of projects. This type of geostructure has a more complex geometry when compared to energy piles, and similarly to energy tunnels, thermo-active diaphragm walls have one side exposed to air, and that leads to a different behaviour in both field and numerical studies.

The aim of this thesis, is to investigate the thermal behaviour of thermo-active diaphragm walls through numerical analyses. To study this phenomena a Three-dimensional (3D) numerical study is required since the planar geostructure embedded with distinct heat exchanger pipes does allow a reduced dimensional analysis. 3D analyses are way more expensive and difficult to perform that e.g. 2D or 1D analysis, due to its complexity and computational requirements. The analyses carried out for this thesis undertaken using the finite element software FEFLOW by MIKE powered by DHI, with an educational licence provided by DHI.

1.2 Motivations and objectives

The lack of field, laboratory and numerical data characterising the thermal behaviour of this energy geostructure leads to the need for further investigation. Considering that energy diaphragm walls will have a possible role in the future, this thesis is driven by the need to better understand the thermal behaviour and energy performance of energy diaphragm walls. This study presents different and complex Finite element analyses (FEA) with 3D models to evaluate and gather numerical data.

Therefore, the aims of this research include:

- A background reading, to identify the different cases and scenarios studied as well as the most important parameters and the ones that might influence the thermal behaviour of energy walls;
- A reproduction of different meshes, with triangular elements with non-identical elements with the aim to reproduce the numerical study performed by Sailer (2020) and to understand the thermal behaviour of a finite element software with 3D model;
- Formulation of accurate and complex 3D analysis that allow a reproduction of the thermal field test performed by Xia et al. (2012) at the Shanghai museum of natural history and evaluate the impact of a different set of parameters;
- Evaluating the thermal performance for short and long-term, given the variation of a different set of parameters.

1.3 Thesis outline

Chapter 2 provides information about the two types of geothermal energy, SGE and DGE, ways to extract and usage of each one. Subsequently, several details about Ground source heat pump (GSHP) systems are presented, main function, application examples and the way it operates. All the three main components of this device are addressed in this chapter, the primary circuit, heat pump and secondary circuit. The last part of the chapter includes a review of the advantages and different types of energy geostructures, it also summarises the research and applications of energy piles and energy tunnels.

Chapter 3 focus around the energy geostructure studied in this thesis, energy diaphragm walls. Initially, a characterization and operation modes of these foundation elements are presented as well as the main advantages and disadvantages when compared to energy piles and energy tunnels. Lastly, some field and numerical studies that were carried out to date are summarised in order to understand the different data gathered since the beginning of the use of energy walls as ground heat exchangers.

Chapter 4 consists on the introduction of the finite element software used in this thesis, FEFLOW and model generation using it. Subsequently, a numerical validation of the model is performed with the help of a numerical study performed by Sailer (2020). Adopting the values and model geometry of the author, different types of meshes are produced in order to replicate the results presented. Lastly, a validation against a field test is performed, with the field test reported by Xia et al. (2012) at the Shanghai Museum of Natural History. In this study, several values of different parameters were varied. These two studies were established in order to understand the viability and sensitivity of the software.

In Chapter 5, the response of the mesh is evaluated one more time for a long term analysis with different parameters and geometries. The main objective of this chapter is to understand the influence of each of the parameters and geometries, on the heat transfer rate of the wall.

Lastly, in Chapter 6, the main conclusions and results of this research are summarised and recommendations for future work are suggested.

Chapter 2

Geothermal energy and ground heat exchangers

2.1 Geothermal Energy

Geothermal energy is known as 'Earth's heat' is the energy that is generated and stored by the earth itself and it is considered a renewable environmentally-friendly energy source. Consequently, it can support the change towards a more viable long-term type of energy and reduce dependence on nonrenewable energy sources, such as fossil fuels. The amount that can be extracted is not constant since it depends on a lot of different factors, such as, depth, location, and geothermal gradient. Within geothermal two different concepts can be identified: deep geothermal energy and SGE.

2.1.1 Deep geothermal energy

The name “deep geothermal” is not entirely related to the factor depth but more to threshold temperatures for geothermal resources where depth usually exceeds 500 m Agemar et al. (2014). As a result, deep geothermal energy is available at lower depths in regions where volcanic activity is more frequent (e.g. Iceland, Azores, etc.) whereas for deeper locations it can be almost anywhere. Extracting deep geothermal energy from areas without volcanic activity is possible but remains challenging because drilling and exploring these deep resources requires a huge investment. The reason why is because wells kilometers in length need to be drilled in order to install the technology that will extract this energy.

2.1.2 Shallow geothermal energy

Shallow geothermal energy can easily be found in a considerable amount, almost anywhere at any given time. According to Brandl (2006) ground temperature tends to be constant below 10-15 m depth with values between 10ºC and 15ºC in European soils, although in the tropics it can reach 25ºC as illustrated in Figure 2.1. The phenom illustrated shows that direct heat exchange with the ground can be achieved with the help of thermo-active ground structures more commonly known as ground heat exchange. During the year, there could be substantial temperature variations, and that leads to a reduction of the heat pump efficiency. Brandl (2006) While during the cold weather season the heat is extracted from the soil providing better thermal conditions to the buildings, in the summer the opposite occurs, heat is injected into the ground to have a better cooling temperature in the infrastructure. For this thesis, SGE harvest is considered and the heat extraction occurs with a GSHP.

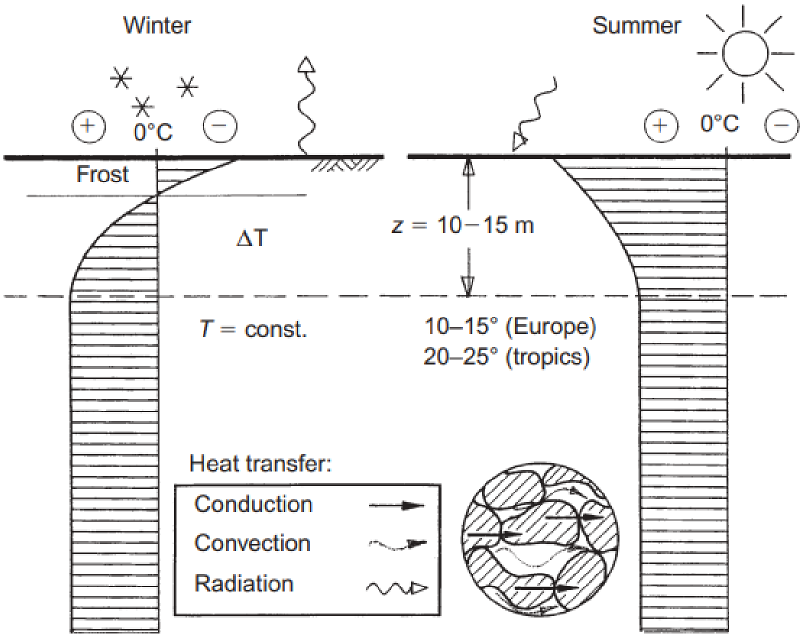

Figure 2.1: Ground temperature profile for shallow depths (Brandl, 2006).

2.2 Ground Source Heat Pump

GSHP are technological systems that harvest SGE. Most, GSHP systems exchange heat with the ground using absorber pipes installed either horizontal or vertical, but increasingly structural foundation elements are being used as an intermediary element to place the tubes, mainly due to the capital savings involved. Brandl (2006) This system can provide a significant amount of energy for heating or cooling in locations such as airport runways, road pavements, bridge decks, and multipurpose buildings amongst others. Brandl (2006) As illustrated in Brandl (2006), this equipment is composed of three components: a primary circuit, a secondary circuit, and, between them, an electrically driven machine, the heat pump or reversable heat pump is installed.

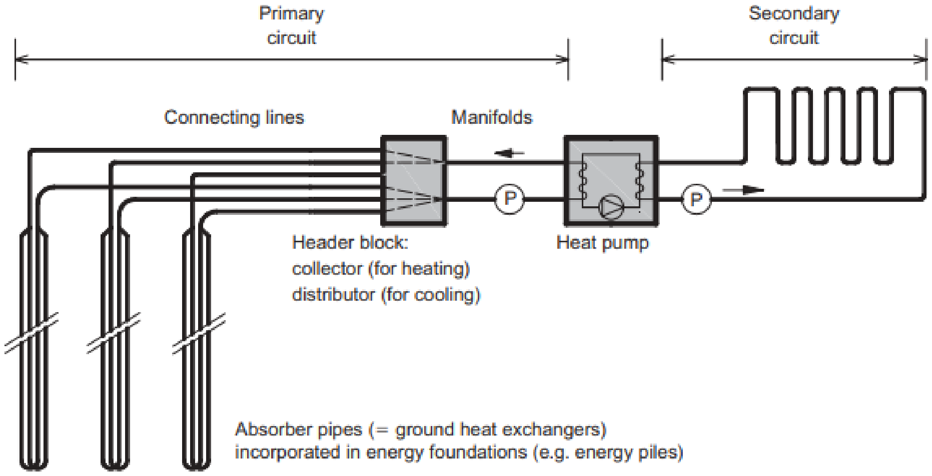

Figure 2.2: Schematic representation of a ground source heat pumo system (Brandl, 2006).

2.2.1 Heat pumps

Heat pumps are an equipment used to transfer heat between spaces with different temperatures. This thermal device can be used in different scenarios but for this thesis, we will focus on heat extraction from the soil to the building itself. This specific process consists in circulating a refrigerant fluid in a closed loop, around a compression–expansion cycle, where the flowing substance keeps alternating between vaporous and liquid states because it undergoes variations in temperature and pressure. The main components of this type of system are the evaporator, the compressor, the condenser, and the expansion valve all represented in Figure 2.3

At the beginning of a cycle, the refrigerant substance is in its liquid state in the evaporator and its temperature is lower than the ground's temperature. Consequently, the heat from the primary circuit warms the fluid which leads to its evaporation into a low pressure and temperature gas. This process requires huge amounts of energy transfer decreasing the primary circuit heat carrier fluid temperature. Thus, this liquid located in the primary circuit needs to be re-injected into the ground to heat up again. Once the fluid is in its vaporous state, as a low temperature and pressure gas, its temperature is not high enough to heat the water, so the compressor is needed. This device compresses the gas with the help of external energy (e.g. electrical energy) increasing the temperature originating a high pressure and temperature gas. After this, the compressor forces the gas to move into the condenser which is in contact with the secondary circuit. The high pressure and temperature gas supply the heat to the heat carrier fluid of the secondary circuit, meaning its temperature decreases. As the heat moves away from the gas refrigerant, it cools off below its condensation point allowing the gas to change to a high-pressure liquid state. Next, the liquid refrigerant passes through an expansion valve whose main function is to reestablish the temperature and pressure of the liquid to the initial conditions. At last, the refrigerant moves to the evaporator, to start a new cycle.

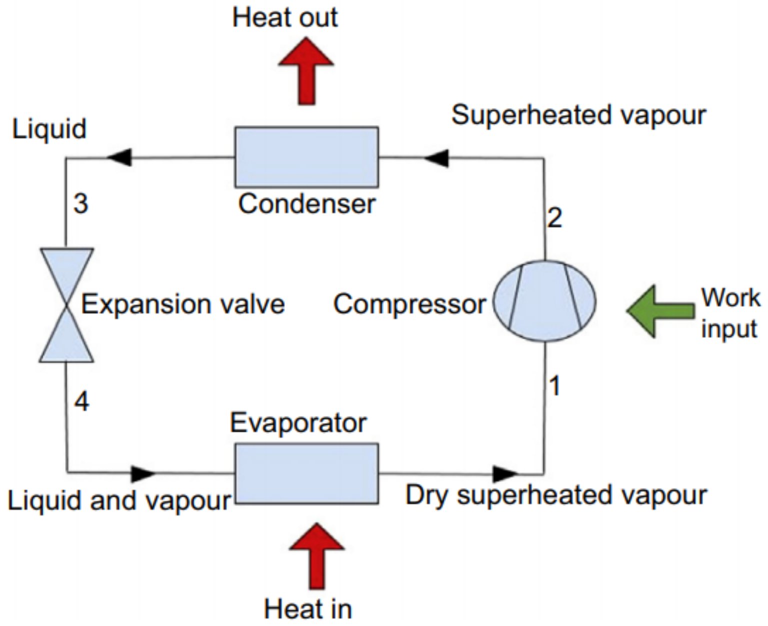

Figure 2.3: Schematic representation of heat pump device Rees (2016)

2.2.2 The primary circuit

The main function of the primary circuit is to exchange heat between the ground and the heat pump. This happens because this circuit contains closed pipework that is in contact with the ground. In fact, the heat exchange occurs via the heat carrier fluid circulating in the absorber pipes that are embedded into the ground. (Laloui and Loria (2019)) This fluid can be water, water with glycol, or a saline solution. Brandl (2006)

The primary circuit can have different types of configurations, usually open-loops or closed-loops. Open-loop systems extract water from the ground and deliver it to the heat pump so that the heat exchange occurs which requires a complex design of the circuit. Ideally, the water can be used on the surface, serving as potable water for washing purposes for example, or it can go back into the ground but sometimes it is necessary to inject the water back down to the ground making this process less economically viable. Nevertheless, this system extracts heat by forced convection meaning it extracts more heat than closed-loop systems. (Banks (2012))

Closed-loop systems do not require extraction of water to exchange heat with the ground meaning it can be installed almost everywhere, in any soil. These systems can be categorized into two types: direct circulation systems and indirect circulation systems. The first one consists of a metal tube, typically in cobber, that runs a high-pressure refrigerant fluid buried into the ground which makes it less used due to environmental concerns and high capital costs. As for the indirect circulation systems, their usage is more frequent. Here, the fluid runs through High-density polyethylene pipes (HDPE), creating a closed circuit that exchanges heat at the heat pump evaporator with the GSHP own circuit. Since closed loop systems are the most suitable ones to be installed in energy geostructures, this thesis is focused on these.

2.3 Energy geostructures

Energy geostructures tend to be in contact with the ground and can be described as underground structures with heat exchangers. These foundation elements can be piles, barrettes, base slabs, or earth retaining structures like diaphragm walls, anchors, and tunnel linings presented in Figure 2.4

All these elements are innovative, multi-functional technologies that can provide structural support while being able to exchange heat with the ground. These structures are commonly made of reinforced concrete, and the main difference, when compared to conventional construction, is that the pipes are placed inside the filling material or fixed through the reinforcing cage This is the preferred solution because this ensures that the reinforcing cage is totally covered with concrete. Brandl (2006) In addition, there are plenty of advantages regarding the thermo-active ground structures, such as:

- Reduction of fossil fuel as a source of energy due to its similarity to other technologies that harvest renewable geothermal energy, hence greenhouse gas emissions.
- Heat exchange with the ground on a larger scale is more efficient because of the use of concrete since it has good thermal conductivity and thermal storage capacity.
- Lower costs because the bending radius of HDPE pipes in many energy geostructures is increased which originates a lower flow resistance of the circulating fluid inside the pipes and this results on a reduce of the pumping power.

Laloui and Loria (2019) reviewed the amount of applications of energy-geostructures that are operational at the moment. This review was based on data obtained from available literature and a survey targeting companies involved in this subject. As a result, the following energy geostructure projects were reported: 157 using energy piles, 17 using energy walls, 11 using energy tunnels and 7 energy slabs. Figure 2.5 a), shows that the number of energy geostructures is increasing in a significant amount, with a predominant application of energy piles over any other types. In addition, the investment in these

Figure 2.4: Examples of heat exchanger pipes in a) energy piles, b) energy slabs, c)energy tunnels and d) energy walls, (Laloui and Rotta Loria, 2020).

innovative constructions leads to a reduction of carbon dioxide CO_2 as illustrated in 2.5 b), it is also exemplified the amount of carbon dioxide saved according to the type of energy geostructure.

2.3.1 Energy Piles

Energy piles are the most used energy geostructures around the world. This foundation element plays a role in both ground support and energy exchange, thus the mechanical behavior of energy piles is different from traditional piles because energy piles are exposed to thermal and mechanical loads. (Wu et al. (2020)) Both bored and driven pile types of a wide range of dimensions have been thermally-activated. The majority of these foundations used to be prefabricated driven piles of reinforced concrete

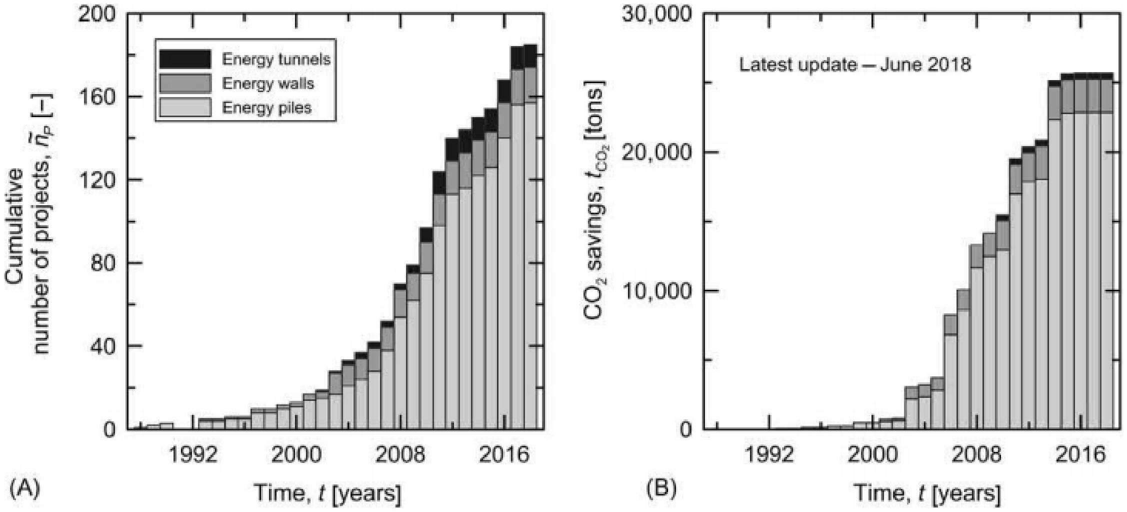

Figure 2.5: Cumulative number of a) energy geostructure projects globally and b) amount of carbon dioxide savings around the world (Laloui and Rotta Loria, 2020).

with an embedded heat exchanger. Since the year 2000, the number of large-diameter bored piles has been increasing significantly Brandl (2006), because large diameter piles can be built, allowing numerous heat exchanger pipes to be installed, achieving a better performance in energetic values. The decrease in the number of driven piles can also be sustained by the increase of ductile cast iron piles with embedded heat exchangers. Brandl (2006) states that the usage of a Continuous flight auger (CFA) requires submerging the reinforcement cage in wet concrete with the HDPE heat exchangers connected to it and this may affect the integrity of the pipes. Consequently, the rotary bored technique should be preferred over CFA as well as the installation of a stiff reinforcement cage. Many pipe configurations can be foreseen for energy piles since these elements have a geometry similar to boreholes. Consequently, every design will influence the type of installation, the operating costs of the energy system, considering that the pipe length may vary as well as the speed of installation. Laloui and Loria (2019) The most common pipe configurations include U-shaped pipe layouts, such as U-shaped pipe, bent U-shaped, series double U-shaped pipe, parallel double U-shaped pipe, and multi U-shaped pipe. These heat exchanger pipes can have different shapes like indirect double pipe, W-shaped pipe, spiral or helix pipe and coaxial pipe configurations. To have a more practical and easy installation, spiral configurations are not installed despite their efficiency in heat transfer potential.

2.3.2 Tunnel linings

The concept of an energy tunnel is typically, the installation of heat exchanger pipes as a closed-loop system in the tunnel linings. (Rees (2016)) The construction of these underground geostructures is increasing since there are multiple benefits associated with its usage, such as:

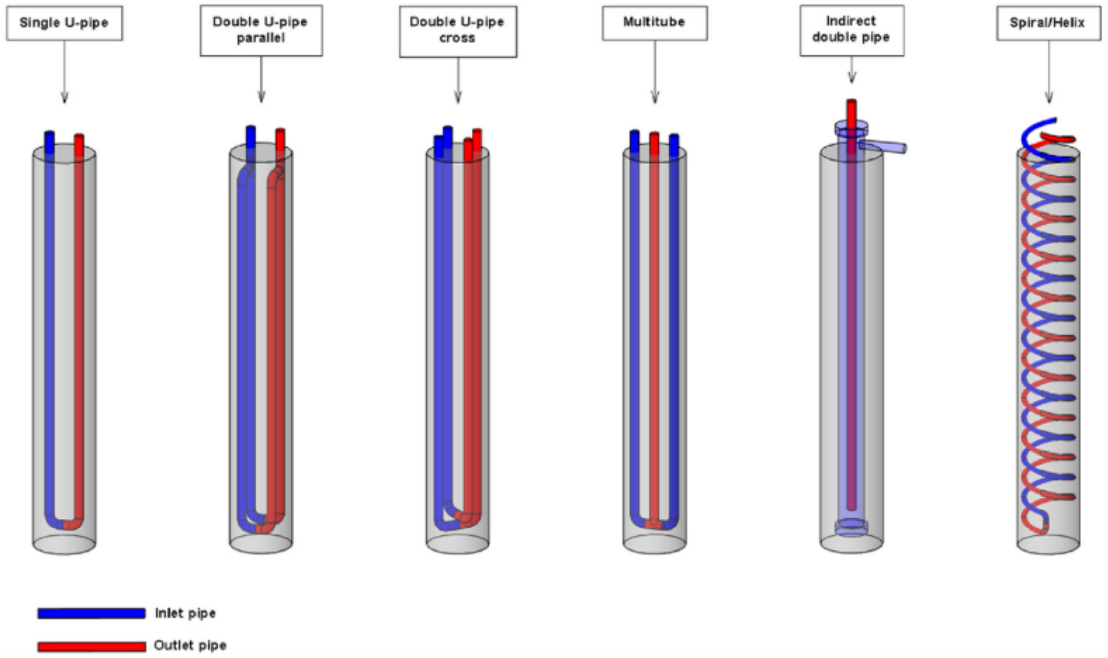

Figure 2.6: Schematic representation of different pipe configurations of energy piles (Fadejev et al., 2017)

- The ability to extract heat from the ground and from the interior space of the tunnel.

- Constant ground temperature because tunnels are normally situated in a depth where the ground temperature is constant. Brandl (2006)

- Maximization of the geothermal energy extraction because tunnels have a huge length of contact between ground and structure, which facilitates the extraction.

- This energy extraction is environmentally friend and economical, this leads to political support making the approval process of this kind of project easier. [Brandl, 2006]

Acording to Rees (2016) the efficiency of an energy tunnel depends on the interior energy environment as well as on the surrounding ground. This is the reason why there are two types of tunnels: cold tunnels and hot tunnels.

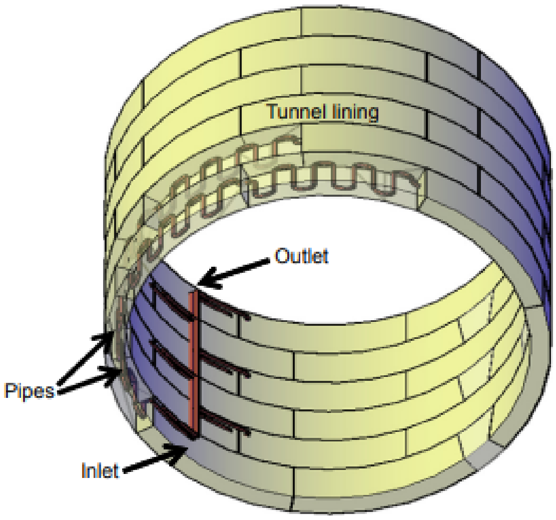

Figure 2.7: Schematic representation of a energy tunnel (Rees, 2016).

Hot tunnels have internal air temperatures higher than the air temperature at the surface. This occurs when there is a lot of internal activity and poor ventilation. An example of a hot tunnel is a deep underground metro system, where a large amount of heat is provided by the train operations even in the winter months. During summer, the heat extraction in metro tunnels will decrease the temperature inside the tunnel which increases passenger comfort and improves the transport's efficiency. As for the winter, the tunnel lining extracts the heat to cool down the soil side, which leads to cooling the tunnel in the following summer.

When the internal air temperature is similar to the surface air temperature these underground structures are named 'cold tunnels' and this usually happens due to good ventilation and a short tunnel length. All of this originates different operational modes and Rees (2016) states that if the ground around the tunnel is used to store heat around the summer season, the efficiency of the tunnel increases with the insulation of the inside section. However, when the interior of the energy tunnel is not insulated the temperature in the interior may vary which can create discomfort for the users of this kind of infrastructure.

According to Rees (2016), tunnel linings for shield-driven tunnels are commonly prefabricated in segments and then installed on the local. During this procedure the prefabricated segments are installed and bonded together to create a tunnel lining ring as illustrated in Figure 2.7. This tunnel lining has integrated heat-exchangers pipes connected to the reinforcement cage. When the installation is concluded, the ends of each tube segment are connected to the ends of the other segments to create a circuit.

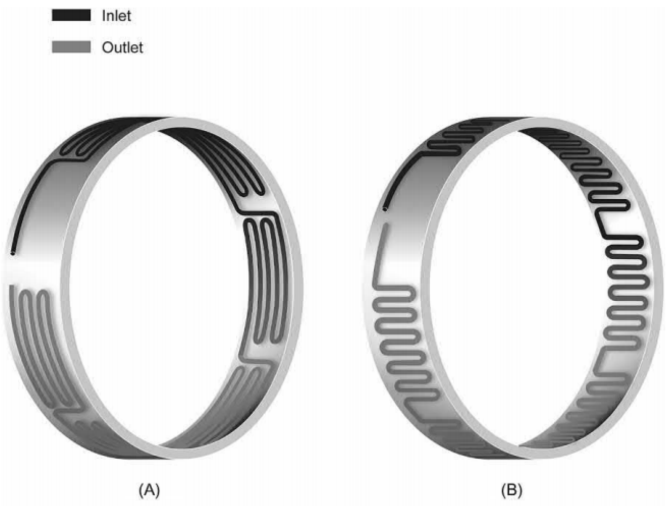

Figure 2.8: Schematic representation of pipe configurations in energy tunnels (Laloui and Rotta Loria, 2020).

A lot of different pipe configurations can be foreseen for this energy geostructure. The main configurations are presented in Figure 2.8 and they can involve pipes with a parallel or perpendicular orientation to the axial direction of the tunnel. Laloui and Loria (2019) These design solutions need to be installed taking into consideration the position of the header pipes.

Chapter 3

Energy geostructures: Energy walls

3.1 Energy walls

Energy walls are a multi-functional technology that can behave as a foundation element and a heat exchanger at the same time. Similar to energy piles, increased caution is required since they are exposed to mechanical and thermal loads. As mentioned before, the number of projects of this underground structure is increasing among energy geostructures. The large surface area of this construction enables a large heat transfer potential. However, limited research has been conducted in energy walls, the implementation of these structures in practice has been thermal analysis with the help of numerical methods. Equally to tunnel linings, energy walls can have one side exposed to air and the other side covered by soil, whereas an energy pile is surrounded by soil. This difference makes the design of these constructions more challenging. According to Rees (2016), energy walls may have two operating modes: heating and cooling or just heating. For the first one, to achieve this, the interior side of the wall must be insulated to guarantee that the heat moves to the soil rather than to the interior environment. As for the heating only, this installation can consider both of the walls sides non-insulated but only for some specific cases, such as underground metro systems. The excessive heat produced by the trains can be an advantage as well, being transferred to the soil and stored to be used later on.

Heat exchanger pipes are inserted in the same way as it is inserted in energy piles, by fixing the pipes to the structural reinforcement cage. In most energy walls, the pipes are fixed closer to the soil side in order to improve the thermal performance of the wall and consequently, reduce the thermal resistance of the concrete Rees (2016). One of the main advantages of energy walls, is the fact that a huge variety of pipe configurations can be considered as shown in Figure 3.1. However, different layouts can provide different heat exchange performance due to aspects, such as variation in pipe length, pipe spacing, energy costs, or even area covered.

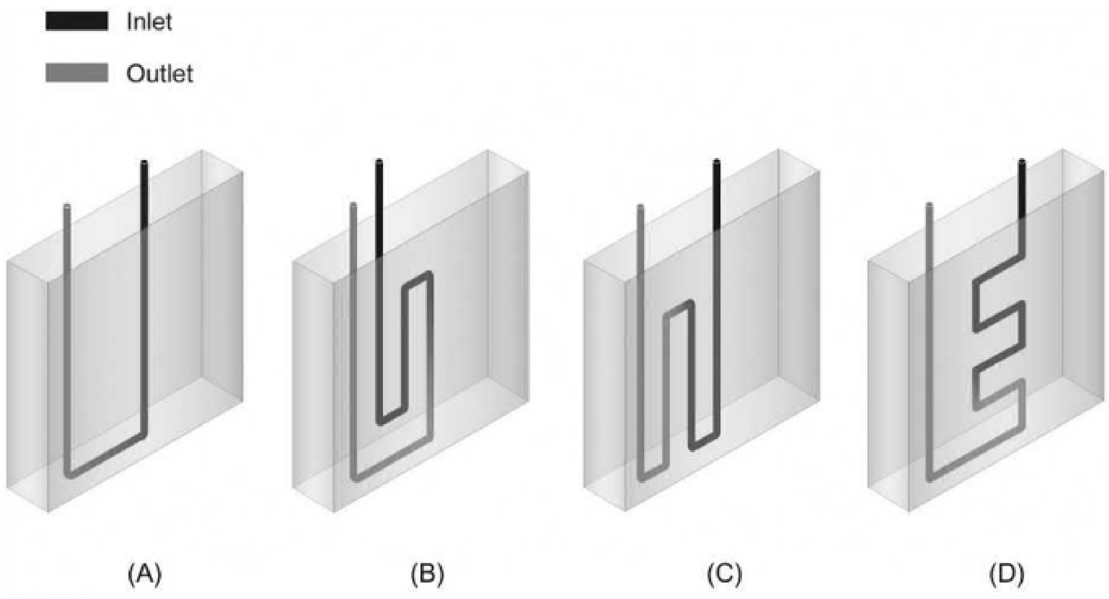

Figure 3.1: Schematic pipe configurations for energy walls: a) U-shaped pipe, b) warped U-shaped pipe, c) W-shaped pipe and d) repeatedly warped pipe (Laloui and Rotta Loria, 2020)

3.2 Field monitoring data

3.2.1 Taborstraße station

As mentioned before, since this energy geostructure is not that common, the amount of long term operational data is lacking. Nevertheless, some literature reports real life applications of this technology. Brandl (2006) states one particular case in Vienna, Austria, at the U2/2 metro line. This case had a major contribution in the energy geostructures field because it provided the insertion of approximately 103 km of heat exchanger pipes. The main project consisted of the extension of the U2 metro line and the execution of four different stations, it included a variety in energy geostructures such as slabs, tunnel linings, and diaphragm walls. The first piece of equipment was installed in Taborstraße station Brandl (2006). The injection of heat into the ground was a primary objective, but in 2008 the station opened with the ability to supply heating and cooling. The station that was thermally-activated and composed of diaphragm walls and energy slabs with a total of 1865 m^2 and 1640 m^2 respectively, each of them containing heat exchanger pipes with 10 m^3 of fluid volume capacity diameter of 25 mm [Brandl, 2006]. Therefore, the U2/2 station uses equipment that can allow a maximum power of 95 and 67 $[kw]$ for heating and cooling, this equipment are two heat pumps and one cooling machine. Brandl (2006)

According to Brandl (2006), enough heat is transmitted into the earth to chill the underground metro station for the entirety of the year, for this to happen energy injection and extraction for cooling and heating average 175 $[MWh/year]$ for the first and 437 $[MWh/year]$ for the later. Over the year of 2009, the fluid temperature inside the absorber pipes was recorded and it is presented in 3.2. According to Brandl (2006), the cooling of the entire metro station is ensured all year due to the fact that there is enough heat being transferred into the ground to achieve this objective.

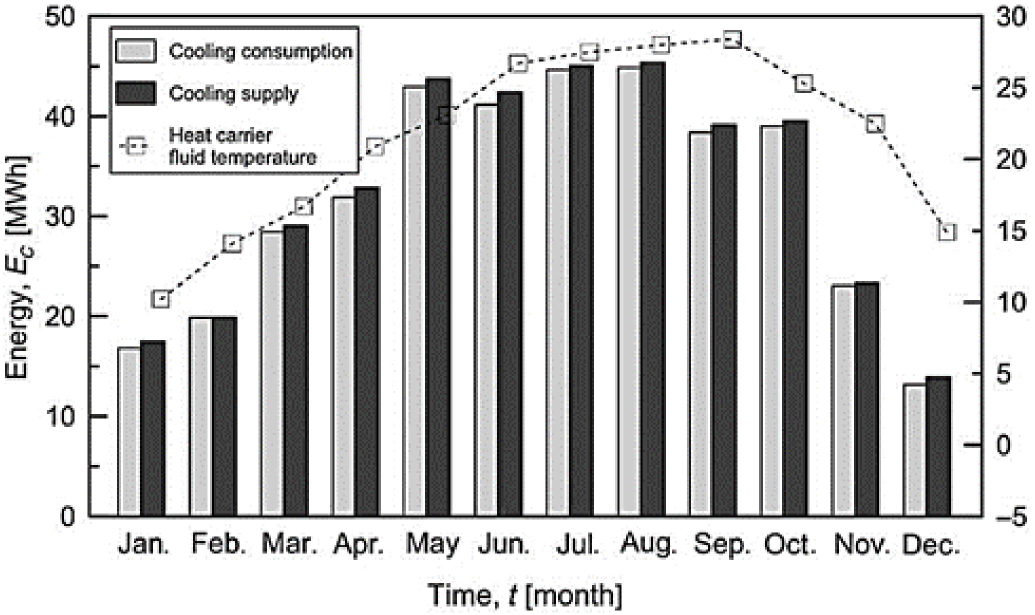

Figure 3.2: Fluid temperature and energy associated with the cooling operation at the Taborstraße station (Laloui and Rotta Loria, 2020

3.2.2 Shanghai museum of natural history

Another real life application of energy geostructures is the Shanghai museum of natural history, located in China (Xia et al. (2012)). This building is public and has two different types of foundation elements: piles and diaphragm walls. The piles were placed under the base slab and the walls were introduced underneath the museum in the metro line 13 and at the museum. A total of 452 W-shaped heat exchangers were introduced in the diaphragm walls with depths between 30 and 38 m. These pipes had a diameter of 25 mm and a wall thickness of 2.3 mm, it is important to notice that each W loop is made by connecting a series of U-shaped loops.

Xia et al. (2012) present an analysis with the objective of reaching an efficient geothermal design. Therefore, in situ tests were performed with a constant temperature method, this method can be described when both heating and cooling have constant inlet temperature. The three energy wall panels that had these tests carried out, had different pipe configurations, illustrated in Figure 3.3. The wall panels had the same depth of 38 m, thickness of 1 m and excavation depth of 18.5 m. The author points out that the base slab was not built when the tests were performed as well as the inner lining and the waterproofing layer. At the beginning of the tests, the average temperature of the soil was reported as

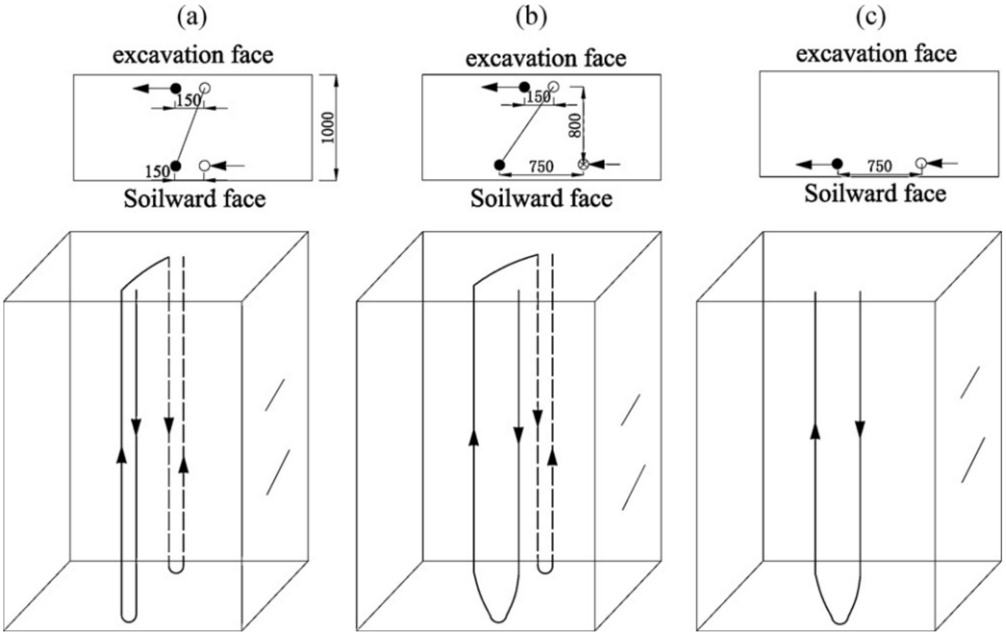

Figure 3.3: Heat exchanger pipe configurations used in the experiment: a) W-shaped pipe, b) improved W-shaped pipe, c) U-shaped pipe (single), (Xia et al., 2012).

16.3ºC and the wall, 23.0ºC. Four groups of tests were conducted in order to study four different parameters that can impact the performance of the heat exchange of the wall. The parameters studied were the velocity of the water and its inlet temperature, the heat exchanger layout, and the operation mode on the transfer rate. Table 3.1 summarises the parameter variations investigated in the tests.

Table 3.1: Different scenarios adopted by Xia et al. 2012 at the field tests.

No.	Influence factors	Factor levels	Other conditions
1	Heat exchanger types	Tubes type (a), (b), (c)	Velocity 0.6 m/s; inlet temperature 35 ℃
2	Water velocity (m/s)	0.25, 0.45, 0.6, 0.75, 0.90, 1.05, 1.30, 1.5	Tubes type (b); inlet temperature 7 ℃
3	Intet water temperature (ºC)	32.0, 35.0, 38.0	Tube type (a), (b), (c); velocity 0.6 m/s
4	Operation modes	Intermittent operation (1:1), Continuous operation	Tubes type (b); velocity 0.6 m/s; inlet temperature 35ºC

For the results, Xia et al. (2012) conclude that the increase of pipe water velocity had a major impact on the heat exchange rate. This is proven when the water velocity is below 0.9 $[m/s]$, however, this changes when it is larger than 0.9 $[m/s]$. Therefore, the author concludes that the ideal velocity is between 0.6 and 0.9 $[m/s]$. For the heat exchangers, the heat transfer rate of the W-shaped loops in the walls is 25% to 40% higher than U-shaped loops. The inlet temperature of the water increases 1ºC and consequently, the heat transfer rate changes linearly with the inlet water temperature, and an intermittent operation mode with 12h working and 12h stopped leads to an improvement of the heat transfer rate by almost 15% as well.

3.3 Numerical Analysis

The use of numerical analysis has been increasing, in part due to the lack of field monitoring data. This method is commonly used to reproduce thermal and mechanical behaviours, and, the following will focus on recent case studies found in the literature about energy walls.

3.3.1 Barla et al. (2020)

An interesting analysis was reproduced by Barla et al. (2020), in order to investigate the behaviour of different types of pipe configurations, study the structural and thermal behaviour of the energy wall and the soil impacts and to understand the amount of extractable and injectable heat into the ground. The wall had heat exchanger pipes embedded and were installed on the ground side. the geometry of this geostructure represented a 15.5 m deep, 0.8 thick and 2.5 m wide of the diaphragm wall panel. The authors mention that preliminary numerical analyses were made to reach the design of the diaphragm wall. Using the finite element software FEFLOW, it was possible to do thermo-hydro simulations. It is mentioned that Darcy's velocity law is used to describe the fluid flow, and the pipes used to run the fluid had a diameter of 25 mm and 2.3 mm of thickness.

The initial temperature of the whole domain was set to 14ºC. Adiabatic boundary conditions were imposed considering that they would be far enough not to influence the results, these were the bottom and farfield boundaries. For the top boundary, it was considered the external air temperature of the city of Torino with a sinusoidal configuration from 0 days to 1460 days.

Lastly, the wall boundary condition is what makes this energy geostructure different from energy piles, since the latter are fully surrounded by soil. Therefore, an adiabatic condition was imposed on this side of the model as the author argued that the heat exchange between the wall and the air is neglected. Finally, there was the insertion of groundwater 5m below the ground surface, after that, the project was simulated for a time frame of one year. For the first simulation, the authors focused on doing simulations to discover which pipe configuration was more effective. So, for this case, the heat exchanger pipes had an inlet temperature of 4ºC, and fluid velocity of 0.6 m/s for one month, and different lengths and pipe configurations, as illustrated in Figure 3.4. For configuration A, a total pipe length of 55.5 m was considered, 68 m for case B and 50.0 m for case C. The authors concluded that configuration C was the most favorable. However, the authors point out that placing the pipes in the horizontal may have disadvantages due to the difficulty of installing them in the configuration, and this can affect the way the concrete is placed compared to vertical placement.

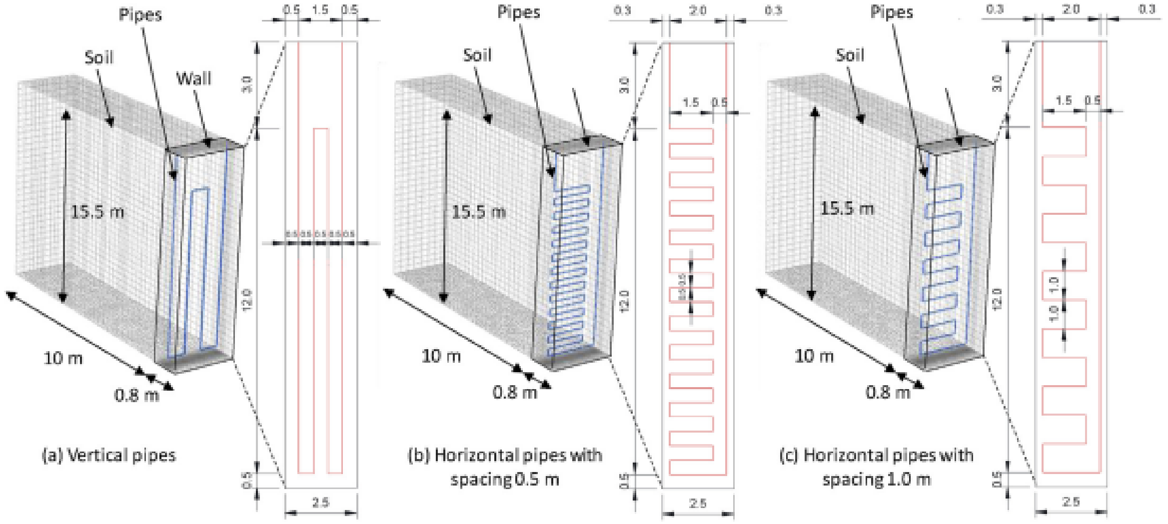

Figure 3.4: Schematic representation of pipe configurations used in the study: a) W-shaped pipe b) Horizontal pipes with a spacing of 0.5 m c) Horizontal pipes with a spacing of 1.0 m, Barla et al. (2020).

For the heat injection/extraction comparison, the authors present results for two different scenarios. In the first, no groundwater flow is considered, and in the other, a ground water flow velocity of 1.5 $[m/d]$ was considered. Furthermore, the analysis was run for total of 4 years, with the first year representing the situation before the geothermal plant was active, this means, only the external surface temperature variation was active. For the subsequent 3 years, the heating-cooling mode was considered. After the simulation, the results obtained show that the groundwater flow has a significant impact on the heat exchange, this value was also reviewed for winter and summer conditions. Based on the results, the authors conclude that for zero groundwater flow, the energy wall will be allowed to exchange 20 and 25$[W/m^2]$, in Winter and Summer respectively. However, when the groundwater flow exists, the values increase to 40 and 50 $[W/m^2]$ respectively. Another analysis executed by the authors, had the main objective to look at the structural and thermal behaviour of the wall. For this analysis, the mesh characteristics and dimensions were 14880 quadrilateral elements, all the geotechnical parameters adopted are presented in Table 3.2.

Different stages are established in order to differ the mechanical loading and the thermal loading leading to different conclusions, the authors present that the thermal activation originated by the pipes led to an increase of 16% of the bending moment and horizontal displacement at the top of the wall. However, the variations are compatible with strength limits.

Table 3.2: Material properties of the wall and soil presented by Barla et al. 2020

Property	Heat carrier fluid	Ground	Concrete
Horizontal hydraulic conductivity, $k_x = k_z [m/s]$	-	$4.15 * 10^{-4}$	10^{-16}
Vertical hydraulic conductivity, $k_y [m/s]$	-	$2.075 * 10^{-4}$	10^{-16}
Specific storage coefficient, S $[m^{-1}]$	-	10^{-4}	10^{-4}
Porosity $n[-]$	-	$0.25 \div 0.3$	0.0
Heat capacity, $c\rho[MJm^{-3}K]$	4.2	2.55	2.19
Thermal conductivity, $\lambda[Wm^{-1}K^{-1}]$	0.65	$2.26 \div 2.8$	2.3
Longitudinal dispersivity, $\alpha_L [m]$	-	3.1	-
Transversal dispersivity, $\alpha_T [m]$	-	0.3	-

3.3.2 Di Donna et al. (2017)

Di Donna et al. (2017) performed a parametric study with the main objective of determining which design parameters are more effective in order to increase the energy performance of the energy wall. Firstly, a numerical study was established with the assistance of a finite element software named FEFlow, based on data from Xia et al. (2012) and Sun et al. (2013), Figure 3.5 illustrates the geometry of the energy wall and pipe configuration used in the numerical model .

The initial temperatures for this model were applied as follows: 23ºC in the wall and 16.3ºC in the soil part, as reported by Xia et al. (2012). For the boundary conditions of the model, the external air temperature was field constant at 10.6ºC and on the soil boundaries, 16.3ºC.

The pipes were reproduced by special One-dimensional (1D) elements, so their thermal resistance was not considered, a diameter of 25 mm and 2.3 mm of thickness was applied. The circulating fluid velocity was set as 0.6 $[m/s]$. The time frame of the simulation was set to two days, and no groundwater flow was considered for this model. Additionally, the thermal properties of both concrete and soil used are those used in the analysis of Xia et al. (2012) and Sun et al. (2013), Table 3.3.

Table 3.3: Material properties of the wall and soil presented by Barla et al. 2020

	Bulk Density, ρ	Bulk Thermal cond., λ	Bulk Specific heat capacity, c
	$[kg/m^3]$	$[W/(mK)]$	$[J/(kgK)]$
Concrete	2500	2.34	1046
Soil	1800	1.74	1690
Heat Carrier fluid	1000	0.58	4200

After confirming the field test could be reproduced by the software, a parametric analysis was performed with the objective of understanding the impact of different parameters on the heat exchange. For

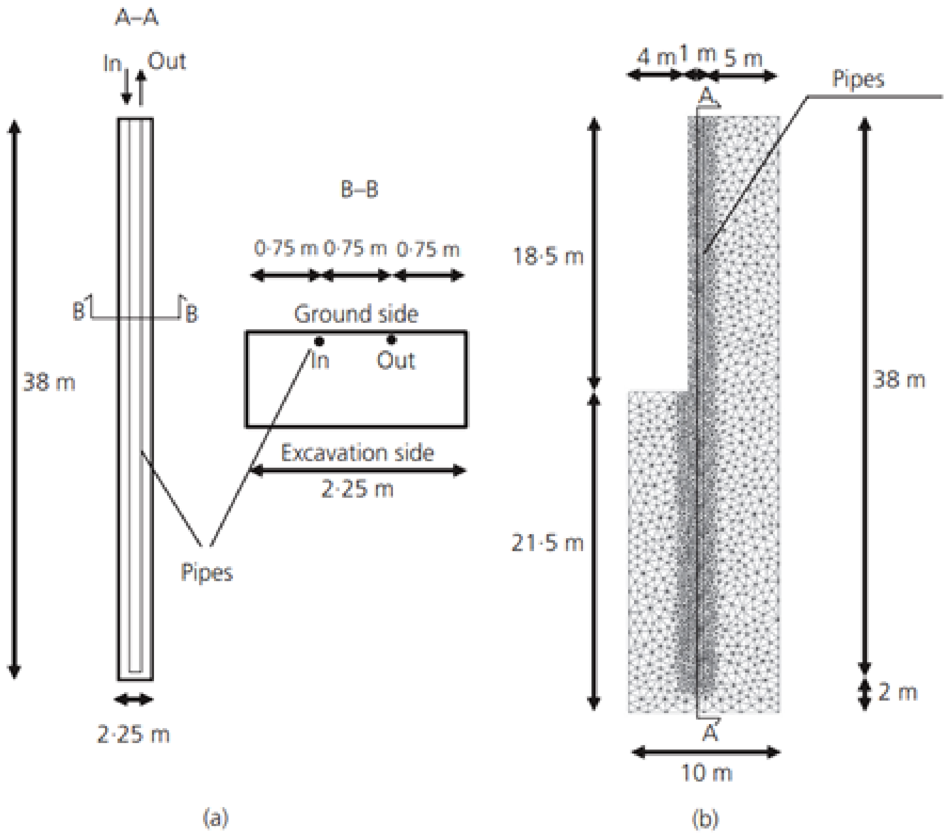

Figure 3.5: Project assumptions: a) pipe configuration single U-shaped b) geometry of the diaphragm wall, Di Donna et al. (2017).

this, eight analyses were run and the parameter settings for each run were determined using a statistical technique and are represented in Table 3.4.

The wall geometric parameters were considered thickness (Tw), the ratio between the excavation and wall depth (R), and cover to the pipes (C). Pipe parameters that were varied included the heat transfer fluid velocity (v), and the pipe spacing (Sp). Finally, the thermal parameters were the initial temperature difference between the soil and the air in contact with the exposed wall surface (ΔT), and concrete thermal conductivity (λ). In all cases, the depth of the wall panel was held constant at 20 m and the half-width (in the plane of the wall) was 1.5 m. The heat exchange pipes were oriented vertically and two pipe spacings were considered, 0.25 m and 0.75 m, Figure 3.6. They were introduced in the soil side of the wall only and had a external diameter of 25 mm. The thermal properties of the soil and concrete are summarised in Table 3.5 and the initial temperature of the soil was set to 12ºC. Boundary conditions applied for the wall side and top depending on the run were equal to 14ºC and 18ºC (yielding δT= 2 or 6ºC, and for the excavation side constant external air temperature was set. The simulation was set to have a duration of 60 days with an inlet temperature of 20ºC and fluid flow velocity according to

Table 3.4: Parameter values for each run of the parametric study by Di Donna et al. (2017)

	Parameter						
Run number	$T_w[m]$	$R[-]$	$S_L[m]$	$C[mm]$	$v[m/s]$	$\Delta T[^\circ C]$	$\lambda_{conc}[W/(mK)]$
1	0.8	1.25	0.25	50	0.2	2.0	1.5
2	0.8	1.25	0.25	100	1.2	6.0	3.0
3	0.8	2.0	0.75	50	0.2	6.0	3.0
4	0.8	2.0	0.75	100	1.2	2.0	1.5
5	1.2	1.25	0.75	50	1.2	2.0	3.0
6	1.2	1.25	0.75	100	0.2	6.0	1.5
7	1.2	2.0	0.25	50	1.2	6.0	1.5
8	1.2	2.0	0.25	100	0.2	2.0	3.0

Table 3.4.

Table 3.5: Model properties assumed in the parametric study from (Di Donna et al. 2017).

	Bulk Density, ρ	Bulk Thermal cond., λ	Bulk Specific heat capacity, c
	$[kg/m^3]$	$[W/(mK)]$	$[J/(kgK)]$
Concrete	2210	Depends on the run	1600
Soil	1900	2.00	1600
Heat Carrier fluid	1000	0.60	4200

Figure 3.7 presents the results of the study after 60 days. The author also presented the results after three, five, and thirty days of operation and ranked all parameters for all the four time-frames. For very short term, pipe spacing (S_L), concrete (λ_c, panel thickness (T_w), and fluid velocity (v) were the dominant parameters. However, as time progresses the difference in temperature between the air inside the excavation and the soil (δT) becomes the most influential parameter.

Pipe spacing reduced in importance as time progresses but still remains in the top three parameters. According to these results, it was suggested to install both sides of the wall with pipes all over the wall's depth to increase the energy efficiency. This proposal also proves that the insertion of energy walls in 'hot excavations' such as metro stations and shallow rail tunnels are a good investment since in long term the temperature between the air inside the excavation and the soil becomes an influential parameter. Finally, another important result tends to be the thermal conductivity of the concrete as it is presented in Figure 3.7. This work highlight the influence of each parameter for the first 60 days of simulation and which parameters can be more important in numerical studies.

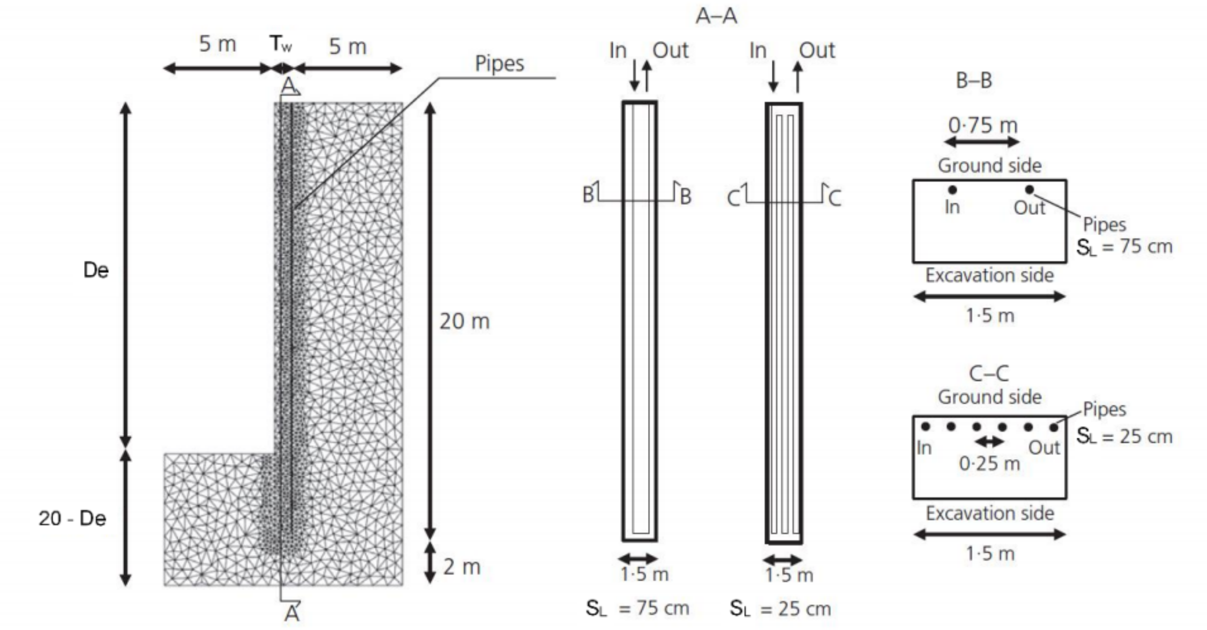

Figure 3.6: Schematic representation: a) geometry of the wall used in the parametric study b) pipe configurations adopted, Di Donna et. al. 2017

3.3.3 Di Donna et al. (2020)

Di Donna et al. (2021) performed numerical analysis with the finite element software FEFLOW with the objective of understanding the impact of ground properties, such as hydraulic and thermal conductivities and ground conditions also known has groundwater temperature and flow velocity. The model established was in three dimensions and the pipes considered were reproduced by special 1D elements. The mesh used in this model had a total of 405460 triangular prismatic six-node elements, 224191 nodes, and the slices of this model had a 0.25 m distance between each other. Figure 3.8 illustrates the model reproduced in the software and all the dimensions adopted, the model is 60 m high and 120 m long. For the wall dimensions, a panel depth of 20 m, panel thickness of 1 m and a panel width of 2.5 m were modelled.

Drawing on the results of Di Donna et al. (2017) which suggested that the ratio between the panel height and the excavation depth does not influence the energy performance of the wall, a constant excavation depth of 10 m was used. For the pipe configuration, a W-shape configuration with 80 m total length was assumed for this model. The pipes are applied in the retained soil side of the wall with a diameter of 25 mm and thickness of 2.3 mm, and are oriented vertically with a spacing of 0.5 m. The concrete cover of the pipes adopted was 50 mm, as illustrated in Figure 3.8. As mentioned before, the pipes and heat carrier fluid were represented by 1D elements with a Hagen-Poiseuille law. The author adopted a value of 0.4 $[m/s]$ to the fluid velocity and an inlet temperature of 4ºC for winter and 28ºC for

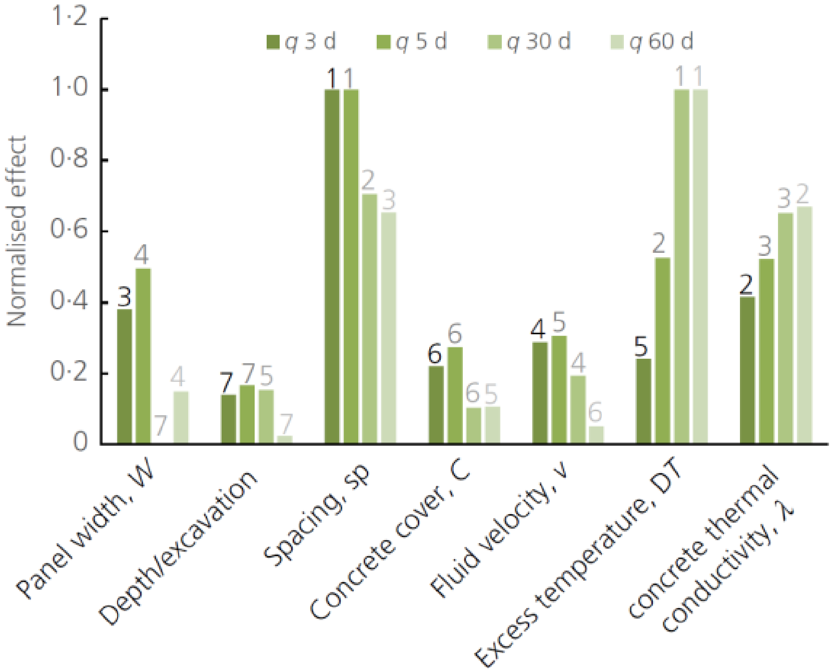

Figure 3.7: Schematic representation of each parameter importance for multiple time frames (Di Donna et al. (2017).

summer were adopted. The simulation was set to run for 30 days.

The soil and concrete properties are presented in Table 3.6 with parametric variations presented in Table 3.7. Groundwater flow tends to have a significant impact in the heat transfer, so this was varied as indicated in Table 3.7.

The temperature of the ground surface was adopted considering the seasonal temperature, for the winter a constant value of 2ºC was set, and for the summer 30ºC. For the front and back vertical sides, an adiabatic condition is assumed and for the excavation side two different conditions were studied: one with fixed constant temperature, for the summer 20ºC were applied and 10ºC for the winter, the second condition was when a convective heat transfer through the wall and slab was imposed also known as Cauchy boundary condition.

The results presented by the author after 30 days of simulation mentioned that the fixed temperature boundary condition showed a difference in temperature between the outlet and inlet of the tubes, 1.9ºC for the summer and 1.4ºC for the winter. The associated values of the exchanged heat were 21.2 $[W/m^2]$ and 15.3 $[W/m^2]$ for the summer and winter respectively. However, for the heat convective boundary this difference was lower for both seasons, 1.7ºC for the summer and 1.2ºC for the winter that leads to a value of injected exchanged heat of 19.1 $[W/m^2]$ and 13.6 $[W/m^2]$ for extracted heat. The efficiency corresponding to the constant boundary condition decreases between 10 to 12%.

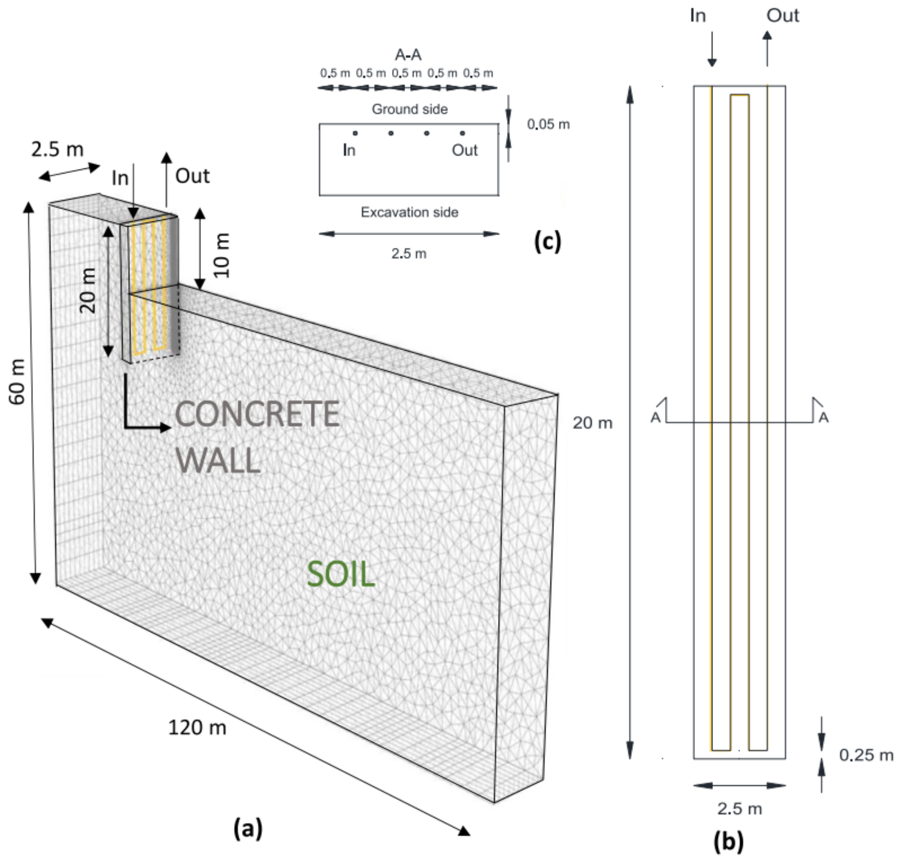

Figure 3.8: Schematic representation of: a) 3D model of diaphragm wall as well as its geometry, b) W-shaped pipe configuration, Di Donna et al. 2020.

The author compared these results with field monitoring data provided by Xia et al. (2012) and Angelotti and Sterpi (2018), and got a good agreement with both of them. In the case of understanding the influence of ground temperature. The simulation was set to be run multiple times in order to vary the undisturbed ground temperature. The results showed that the increase of the undisturbed ground temperature leads to a reduction of efficiency in the summer. However, the opposite happens in the winter season when the heat is being extracted. Additionally, the heat transfer boundary condition decreases the total heat exchange, because in the summer the temperature increases, and in the winter the temperature decreases. Therefore, the values are in good agreement with the values presented by Angelotti and Sterpi (2018).

The next parameter investigated, was the bulk thermal conductivity of the soil 3.7, all the values were compared with Angelotti and Sterpi (2018), and the values show great similarity, the author concludes that the increase in heat exchange is independent of the boundary condition assumed and the heat convective boundary seems to be better reproduced. Therefore, the author concludes that this parameter can increase the energy availability by up to 150%.

Table 3.6: Fixed material properties presented by Di Donna et al. 2020

Property	Concrete	Soil
Horizontal hydraulic conductivity, $k_x = k_z[m/s]$	10^{-16}	$4.15 * 10^{-3}$
Vertical hydraulic conductivity, $k_y[m/s]$	10^{-16}	$2.1 * 10^{-4}$
Specific storage coefficient, S $[m^{-1}]$	10^{-4}	10^{-4}
Porosity $n[-]$	0.0	0.25
Effective heat capacity, $c\rho[MJm^{-3}K]$	2.19	2.55
Effective thermal conductivity, $\lambda[Wm^{-1}K^{-1}]$	2.3	Table 3.7
Longitudinal dispersivity, $\alpha_L[m]$	-	3.1
Transversal dispersivity, $\alpha_T[m]$	-	0.3

Table 3.7: Variable material properties presented by Alice Di Donna et al. 2020

Property	Soil lower bound	Soil reference case	Soil upper bound
Effective thermal conductivity, $\lambda[Wm^{-1}K^{-1}]$	0.9	2.26	3.9
Undisturbed ground temperature, $T_o[T[°C]$	8	14	18
Groundwater flow velocity, $v[m/day]$	0	0	2

The final parameter analyzed was the impact of the groundwater flow velocity, the effect of this variable showed that the exchanged heat increases in a non-linear way and can increase the energy available by 150% compared to the case with no flow.

3.3.4 Markasis and Narsilio (2020)

Markasis and Narsilio (2020) developed a study with the main objective of providing more information about the geothermal design of energy walls. Several factors were studied by the authors, such as pipe configuration, ground thermal properties and geometry of the wall. To achieve this, a finite element software was used to perform a numerical analysis. The mesh was composed by free tetrahedral elements which were refined smaller near the structural elements. The diaphragm wall model geometry is presented in Figure 3.9, this model included a top and bottom slab that typically enclose the underground space.

Therefore, the boundary conditions established for the model were adiabatic for the top and bottom surfaces, this assumption was applied because it is was considered a normal phenom within the city center under buildings. Additionally, the inner surfaces boundary conditions were also adiabatic, and the farfield boundary had a constant temperature of 18.33ºC applied (Figure 3.9). The authors evaluated two pipe configurations, vertical and horizontal, Figure 3.10, and the thermal properties adopted in Table 3.8. Concrete cover to the pipes was set at 0.275 m for the retained soil face, 0.3m above the bottom of

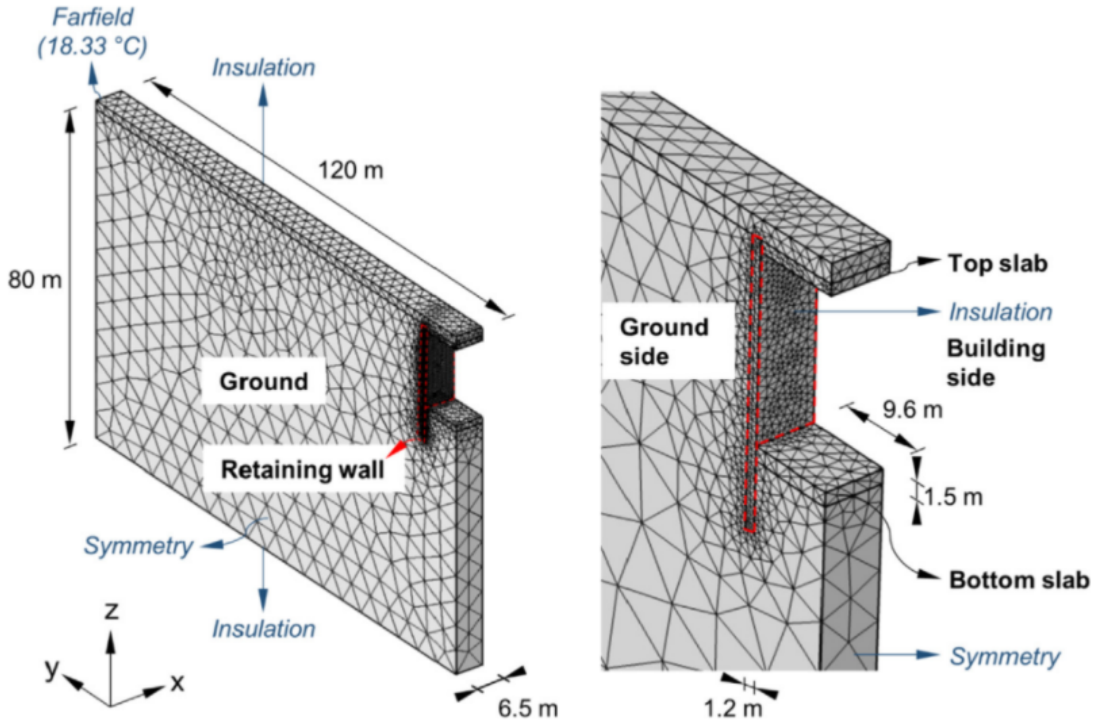

Figure 3.9: Schematic representation: Left) geometry and boundary conditions adopted for the energy wall and Right) boundary conditions and geometry adopted to the slab, Markasis and Narsilio (2020).

the wall panel and 0.4 m from the sides of the 6.5 m wide panel. The depth of embedment of the wall is 25% of the wall depth, represented in Figure 3.10

Table 3.8: Material properties presented by Markasis and Narsilio (2020)

Parameter	Value	Unit	Description
λ_{ground}	2.2	$[W/(m*K)]$	Thermal conductivity of ground
ρ_{ground}	2400	$[kg/m^3]$	Density of ground
$C_{pground}$	830	$[J/(kg*K]$	Specific heat capacity of ground
$T_{farfield}$	18.33	$[°C]$	Average ground temperature
$\lambda_{concrete}$	2.1	$[W/(m*K)]$	Thermal conductivity of concrete
$\rho_{concrete}$	2250	$[kg/m^3]$	Density of concrete
$C_{pconcrete}$	890	$[J/(kg*K]$	Specific heat capacity of concrete
λ_{fluid}	0.6	$[W/(m*K)]$	Thermal conductivity of carrier fluid
ρ_{fluid}	1000	$[kg/m^3]$	Density of carrier fluid
C_{pfluid}	4180	$[J/(kg*K]$	Specific heat capacity of carrier fluid

The outer diameter of the pipe was set to 25 mm and the refrigerant fluid flow rate was set at 5.5 $[L/min]$. The authors mention that thermal load defines the thermal energy that the energy geo-structure stores or extracts from the ground to the building. For this study, two different ground thermal distributions are considered, unbalanced and balanced. The first one has in mind data centers that can have cooling demands with minimal heating requirements during the winter. The later, considers equal amounts of heating and cooling energy across the year, and has the advantage of facilitating the optimal usage of the GSHP system.

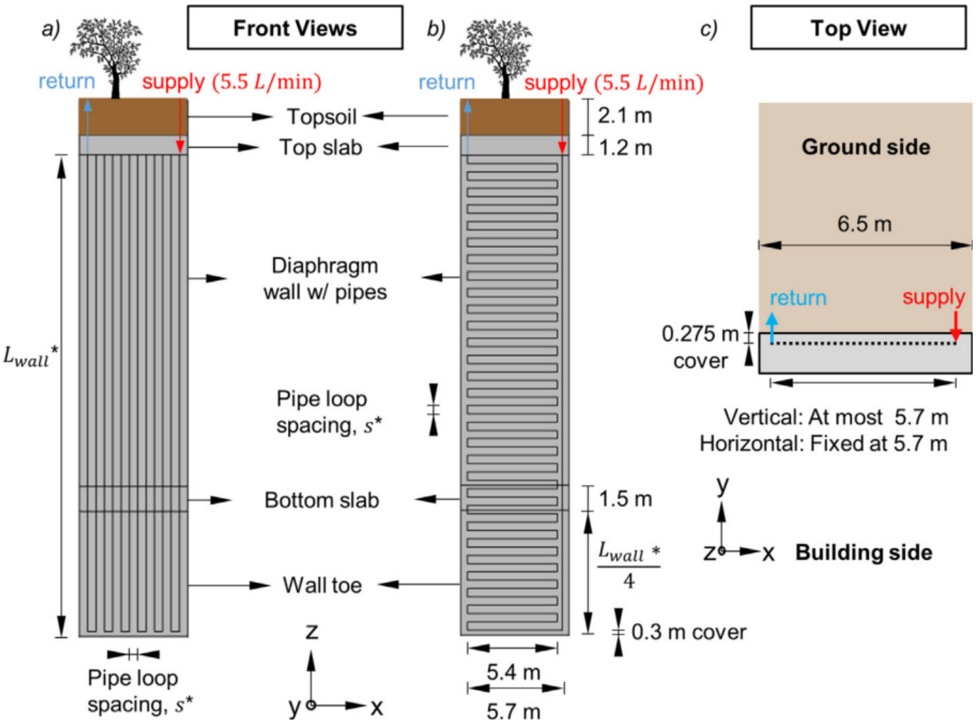

Figure 3.10: Layout of the enhanced heat exchanger pipes: Left) vertical, b) horizontal (Markasis and Narsilio et al., 2020).

For the results, the author refers that the thermal conductivity has a major impact on thermal performance for shallow walls. The vertical pipe configuration showed a better performance than the horizontal one. However, the vertical configuration needs to have the piped jointed between diaphragm wall sections, therefore it can lead to significant delays to the project. The horizontal configuration is more suitable when delays can be very costly. The pipe spacing for deeper walls is not that significant, this can allow higher pipe spacing that leads to lower capital costs, the author presented results about a ratio of optimal spacing over wall depth which shows that the larger the spacing, the more thermal performance discrepancies between the two pipe configurations will occur. Markasis and Narsilio (2020) also conclude that introducing a pipe spacing lower than 300 mm has no performance increase since the pipe spacing is independent of the soil thermal conductivity. Finally, it is mentioned that balanced thermal load distributions can allow higher pipe spacing and less total length of the pipes.

3.3.5 Markasis et al. 2020

Markasis et al. (2020) performed a study with the main objective of investigating how to increase the thermal performance of energy retaining walls. Therefore, the author focused on the efficiency of the heat transfer for energy retaining walls with an embedded pile as presented in Figure 3.12. With the help of the 3D computational finite element software, a long term transient analyses were performed where the heat transfer was modelled by conduction in the soil materials and convection in the pipes. Groundwater flow was not considered, and pipe fluid flow was reproduced with 1D elements. First, the author validated the model with experimental data, from a field test run by the University of Melbourne. The experimental data consisted of a thermal response test performed over 18.5 days. A constant power of 5.5 kW was applied to the pile. The validation of the numerical model consists of a single 40 m deep geothermal pile that is installed within a soldier pile retaining wall with 20 m of excavation depth presented in Figure 3.11

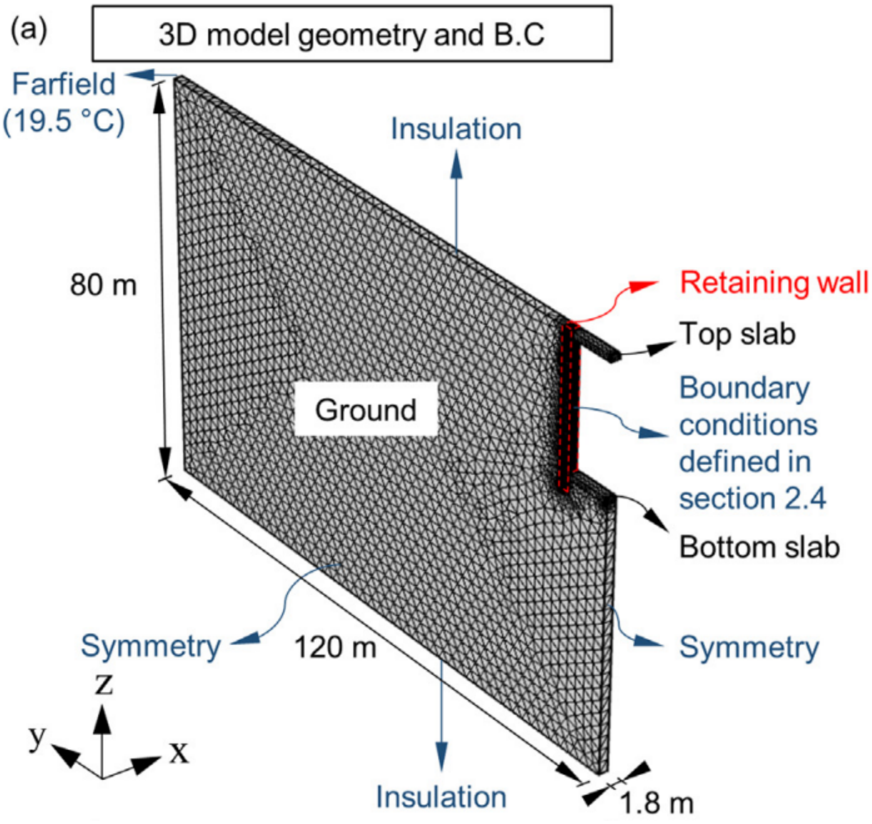

Figure 3.11: Schematic representation of the model geometry and boundary conditions applied, Markasis et. al. 2020.

The installation of a pipe configuration of 4 U-loops connected in at the bottom and top of the pile, with one inlet and one outlet. The connected series has a total length of 220 m. For the boundary conditions of the model, the farfield boundary was set to have a constant temperature equal to the

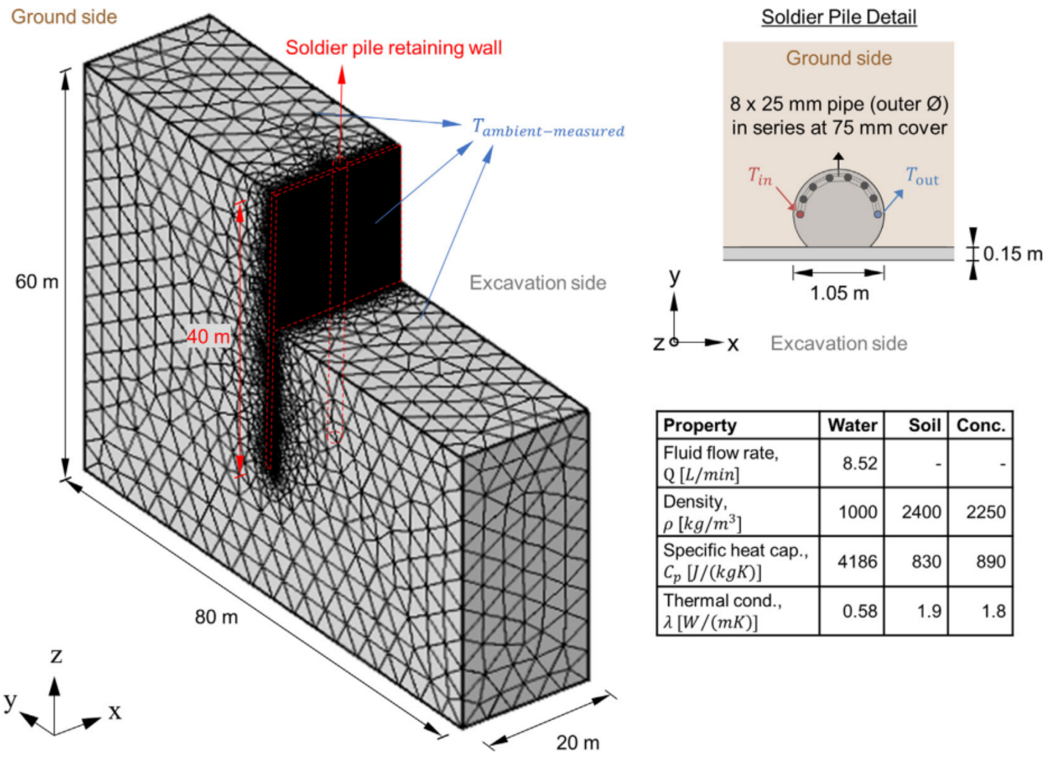

Property	Water	Soil	Conc.
Fluid flow rate, $Q\ [L/min]$	8.52	-	-
Density, $\rho\ [kg/m^3]$	1000	2400	2250
Specific heat cap., $C_p\ [J/(kgK)]$	4186	830	890
Thermal cond., $\lambda\ [W/(mK)]$	0.58	1.9	1.8

Figure 3.12: Schematic representation of the model generated and material properties by Markasis et al. 2020

measured annual ground temperature of 19.5ºC, the side and top boundary where measured ambient temperature was considered. The experimental results and their comparison to the model showed a good agreement.

For the study, all the geometry and boundary conditions are presented in Figure 3.11. The material properties are presented in Table 3.9. For the thermal loads, the same strategy as used by Markasis and Narsilio (2020) was applied, balanced and unbalanced thermal loads.

It is important to notice that the top and bottom boundaries, the author chose insulation to replicate a more realistic scenario. However, the author decided to investigate which boundary should be placed at the slab and at the excavation side, since this part of the wall it is important to ensure a realistic numerical model. Therefore, three different approaches for these locations were performed:

- Thermal insulation, to prevent heat transfer to the underground space
- Assuming that the operation of the system hasn't impact on the wall, there is an establishment of constant or varying temperature with time.
- Model the air-wall interaction, which means modelling the air space as a fluid volume.

The three approaches were performed and the author mentions that between concrete and modeled air there can be heat transfer, which happens when modeling the inner wall and slab surfaces using

Table 3.9: Material properties presented by Markasis et al. 2020

Parameter	Value	Unit	Description
λ_{ground}	2.7	$[W/(m*K)]$	Thermal conductivity of ground
ρ_{ground}	2400	$[kg/m^3]$	Density of ground
$C_{pground}$	830	$[J/(kg*K]$	Specific heat capacity of ground
$T_{farfield}$	19.50	$[°C]$	Average annual ground temperature
$\lambda_{concrete}$	2.1	$[W/(m*K)]$	Thermal conductivity of concrete
$\rho_{concrete}$	2250	$[kg/m^3]$	Density of concrete
$C_{pconcrete}$	890	$[J/(kg*K]$	Specific heat capacity of concrete
λ_{fluid}	0.58	$[W/(m*K)]$	Thermal conductivity of carrier fluid
ρ_{fluid}	998	$[kg/m^3]$	Density of carrier fluid
C_{pfluid}	418.5	$[J/(kg*K]$	Specific heat capacity of carrier fluid

continuity. It is also mentioned that the modeling is different depending on whether is the air moving or not. In the first approach, air velocity was set to zero, and adiabatic condition is applied to the wall-air boundaries, this scenario is not common since air is rarely stagnant. The author considered this condition in order to investigate the system behaviour. The author assumed different velocities in order to represent a poor ventilation space and a common ventilation space, assuming 0.01 $[m/s]$ and 0.50 $[m/s]$ respectively. The initial temperature of the air is set to 21ºC and all simulations were set to 25 years of operation. The results for all simulations are presented in Figure 3.13, plots (a) and (b) represent unbalanced thermal load response, and (d) and (c) balanced ones. Plot (a) and (c) thermal insulation was adopted, however, for (b) and (d) the air was modeled with different velocities.

Adopting thermal insulation to model the wall and slab boundaries, the results presented that it is the better approach since applying defined wall temperature to the wall can lead to unconservative results. When the underground space is ventilated thermal insulation should be considered in order to create a separation between the underground building space and the sources of heat. Setting a defined temperature or forced ventilation can lead the heat into the underground space and that may be an ineffective system. The author also states that when the underground space is unventilated or poorly ventilated, if the thermal load is balanced, thermal insulation can be a good approach as well. Markasis and Narsilio (2020), shows that when a defined temperature is applied to the boundary condition the wall won't be submitted to realistic condition because there needs to be an assumption of heat transfer through the wall and it does not affect the temperature.

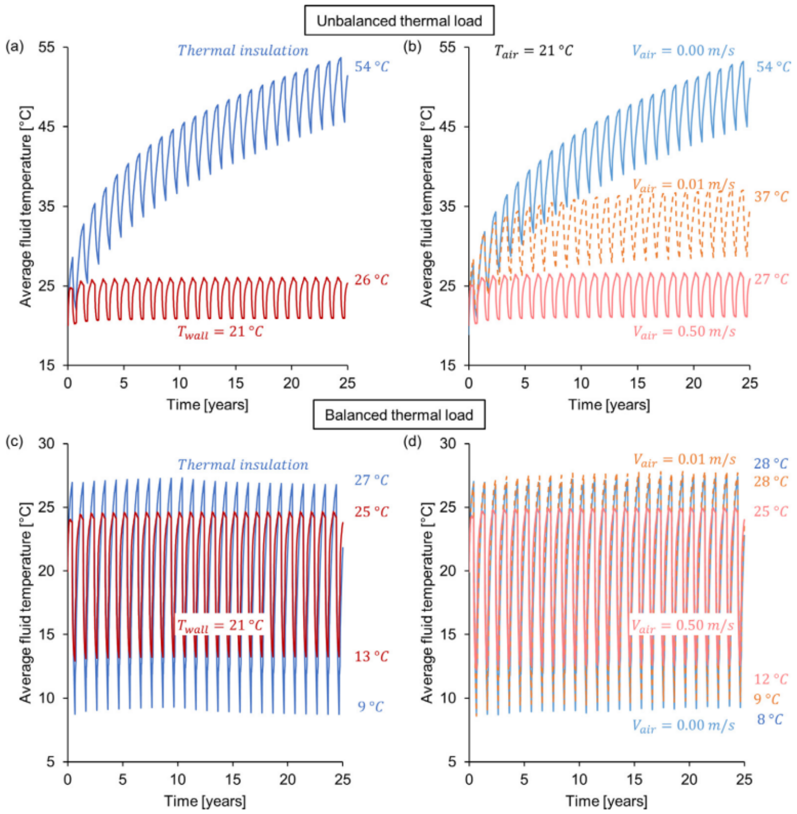

Figure 3.13: Results obtained by the author; a) applying thermal insulation or a defined temperature and the unbalanced thermal load, b) modelling the air for different air velocities and the unbalanced thermal load, c) applying thermal insulation or a defined temperature and the balanced thermal load and d) modelling the air for different air velocities and the balanced thermal load.

3.3.6 Dong et al. 2019

Dong et al. (2019) presented a study of a thermal-mechanical behaviour of energy diaphragm wall through numerical modeling of a physical small-scale energy diaphragm wall section installed in dry sand. To perform the monitoring of the physical energy wall's behavior a number of sensors were placed inside the wall and in the surrounding soil. Strain, pressure cells, and temperature sensors were applied. During this process, with the aid of FEA it was possible to predict the thermo-mechanical behavior of this wall and allowed a better understanding of this subject.

The physical model was 2.00 m high, 1.80 m wide, and with a thickness of 0.20 m. It was installed in a steel box and was exposed to one indoor air with a controlled temperature between 8ºC to 12ºC. Additionally, the heat convection established on air-surface was set to natural convection. The pipes of this wall are high-density polyethylene pipes, with an external diameter of 10 mm and 8 mm of internal diameter. The pipe configuration consists of a continuous connected single U-shaped tubes, it is important to notice that the pipe spacing was 0.17 m. Circulating water originated a heat transfer to the wall since the water had a temperature of 50ºC and a flow rate of 0.03 $[m^3/h]$. The test had a duration of 75 hours and as mentioned before, with the help of different sensors it was possible to record all the temperature, strains, and earth pressures at the soil/wall interface as well as inside the wall.

The author presents an additional study with the main objective to predict the mechanical behavior of the wall during the experiment just mentioned. Therefore, a finite element software named ANSYS was used to reproduce a 2D mesh with different thermo-mechanical boundary conditions. For the mechanical, the left and right boundary were restrained as well as the bottom boundary. However, the top boundary was set free which allowed displacement. For the thermal boundary conditions, the two sides and bottom were set to be adiabatic, although the top boundary was set with an air temperature of 10ºC and the coefficient of convective heat transfer was set to 2.5 $[W/(m^2.K)$ In addition, this numerical study had important governing laws that influenced the model itself:

- The heat transfer was set to be conduction only.
- The wall and the soil had a thermo-mechanical behavior of linear elastic
- With the Drucker-Prager yield criterion it was possible to consider an elasto-plastic mechanical behavior of the soil and linear elastic to the wall.

For the results, the author concluded that the heating leads to an expansion of the wall, this causes an increase of the earth pressure at the soil/wall interface. Although, this originates an increase in the vertical stress inside the wall and an increase of the mobilized shaft friction along the wall. The short-term heating showed to have a more significant temperature gradient across the thickness of the wall, therefore, stress/strain variation is generated in the first hours of the experiment. Additionally, some discrepancy between the numerical model and experiment was found, although using an elastic law is a good approach to predict the behavior of the wall under thermal loading if the law is set for the thermo-mechanical behavior of soil. Another conclusion that the author states was the usage of a Two-dimensional (2D) numerical model should be appropriate to analyze the thermo-mechanical behavior observed by the physical model, since the difference between the inlet and outlet temperature induces a non-uniform temperature distribution on the interior of the wall.

3.3.7 Silva (2020)

Silva (2020) reported a numerical study about the use of retaining walls in shallow geothermal energy systems. The author used the finite element software FEFLOW, to develop a 3D model, where the influence of different parameters were studied for a long term analysis. The parameters studied in this parametric study were wall geometries, pipe configurations, soil thermal conductivity, several boundary conditions, and the inlet temperature of the fluid. Firstly, for the wall geometry and pipe configuration, the author established three and two different configurations respectively, the wall also included a slab attached to the retaining wall. Figure 3.14 and table 3.10 presents the different assumptions.

Table 3.10: Different wall geometries established by Silva in the parametric study

Geometry	Wall depth, $Dw[m]$	Excavation depth, $De[m]$	Panel width, $W[m]$	Wall surface area, $Aw[m^2]$	Wall thickness, $Tw[m]$	Slab thickness, $Ts[m]$
G1	15	10	1.6	24	0.6	0.6
G2	25	20	1.6	40	0.9	0.9
G3	35	30	1.6	56	1.2	1.2

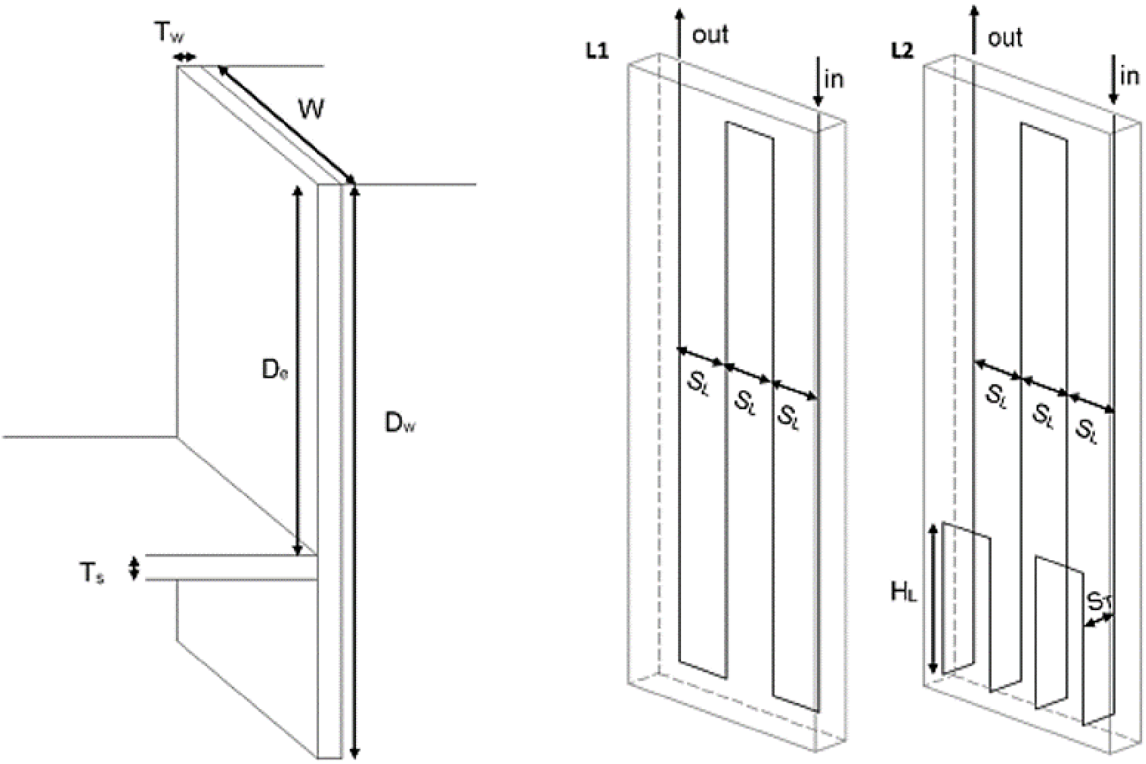

Figure 3.14: Wall and heat exchanger loop geometry adopted by Silva

As for the material properties, all were considered constant throughout the study, except for the soil thermal conductivity, where values of 1.0, 2.0, and 3.0 were assumed in order to study its impact.

The initial temperature defined for the wall and soil was a constant value of 17ºC, and the time length of the analysis was set to 3 years (1095 days). However, for the boundary conditions, the author adopted a range of values, which are calculated with a sinusoidal periodic function to recreate the summer and winter seasons. The boundaries were separated between inlet node, interior space boundary, and exterior boundary. The interior space boundary was set to the excavated part of the wall, the exterior boundary was set to the top part of the model. The outlet node was set free and the rest of the model no heat flux boundary was established. As can be seen, by table 3.11, some additional profiles were defined and the respective sinusoidal equations are presented.

Table 3.11: Different boundary conditions established by Silva in the parametric study

Assigned boundary	Case	Temperature	Equation
Inlet node	In_1	17 ± 10	$T_{in}(d) = 17 + 10sin(2\pi d/365)$
	In_2	20 ± 7	$T_{in}(d) = 20 + 7sin(2\pi d + 25.7294 * 2\pi/365)$
	In_3	14 ± 7	$T_{in}(d) = 14 + 7sin(2\pi d + 25.7294 * 2\pi/365)$
Slab and wall surface	Int_1	17 ± 3	$T_{int}(d) = 17 + 3sin(2\pi d/365)$
	Int_2	23 ± 5	$T_{int}(d) = 23 + 5sin(2\pi d/365)$
Top boundary	Ext_1	17 ± 6	$T_{ext}(d) = 17 + 6sin(2\pi d/365)$

For the results, Silva concluded that for the parameters, the soil thermal conductivity presented a huge impact, the heat transfer rate increased approximately 23.3% between a soil thermal conductivity of 1.0 $[W/mK]$ and 3.0 $[W/mK]$. Wall geometry presented a relation, where the deepest geometries provided more energy when compared to shallower geometries. Another parameter with a significant impact is the interior space boundary condition, a decrease of approximately 42% was verified when insulation between the wall and the space is considered. However, the temperature of the top boundary, inlet temperature boundary of the water and pipe configuration presented a limited impact for the long term analysis of 3 years.

3.4 Summary of previous numerical studies

Regarding the numerical studies presented in this Chapter Table 3.12 was made with the parameters studied from each author. A lot of authors performed numerical studies with different pipe configurations in order to understand its impact on the energy wall. A considerable number of authors presented that this parameter is extremely important regarding the thermal performance of the energy walls at a short and long term analysis (Di Donna et al (2017); Barla et al. (2020); Markasis and Narsilio (2020); Silva (2020)). Several authors state that installing the pipes in the horizontal may affect the energy wall construction and lead to significant delays (Barla et al. (2020) and Markasis and Narsilio (2020)) however, horizontal configuration presented a better thermal performance of the energy wall. The most adopted pipe configuration was the W-shaped loop piping, and in all studies presented a good thermal performance. The thermal conductivity of the concrete, this parameter presented different values for all numerical studies as well as the initial temperature of the model, the majority of the authors presented that the concrete thermal conductivity is a major parameter as well as the initial temperature of the wall and soil (Di Donna et al. (2017) and Markasis and Narsilio (2020). Regarding Di Donna et al. (2020) presented that soil thermal conductivity was an important parameter, Silva (2020) obtained that conclusion as well.

Table 3.12: Summary of the parameters analysed by the authors.

Parameters	Barla et al. 2020	Di Donna et al. 2017	Di Donna et al. 2020	Markasis et al. 2020	Markasis and Narsilio 2020	Silva 2020
Run time	4 years	3, 5, 30 and 60 days	30 days	25 years	20 days	3 years
#Wall geometries	1	2	1	1	1	3
Fluid velocity [m/s]	0.6	0.6	0.4	0.5 and 0.01	5.5 [L/m]	0.6
Initial temp.	14	Soil - 16.3 Wall - 23	-	Soil -19.5 Air - 21	-	17
Concrete thermal conductivity	2.19	2.34	2.3	1.8	2.1	2
Soil thermal conductivity	2.55	1.74	Table 3.7	1.9	2.2	1/2/3
#Pipe configuration	3	2	1	1	2	1
Boundary condition	Temp. and adiabatic	Temp. and adiabatic	Temp	Temp. and adiabatic	Temp. and adiabatic	Temp. and adiabatic

Chapter 4

Numerical analysis: model validation

4.1 Finite element software FEFlow

In this thesis, the finite element software FEFlow is used to perform the numerical analysis. This software is commonly used to solve saturated and unsaturated groundwater flow equations as well as mass and heat transport in fractured and porous materials. In addition, the software has the ability to simulate heat transfer by conduction and forced convection, in this work a three-dimensional model is created. The following sections and chapters will detail the model used in this study.

4.1.1 Model generation using FEFlow

In the first place, a finite-element mesh has to be generated to reproduce one viable model domain, therefore, a vertical cross-section needs to be defined first. In this phase, the user uses nodes and lines to define the dimensions and limits of the model. Every line needs to have a node at each end, and are used to establish a continuous alignment of mesh element edges that will be visible in the mesh after its generation. Afterward, the type of mesh needs to be defined by the user, this thesis will focus on triangular elements only since the triangle has a better performance with complex geometries and the simulations run faster.

In this phase, there is also the option of doing some mesh refinement. Following this process, the 2D model is converted into a 3D model, this process occurs with the insertion of a layered configuration. These layers are also known as slices. The distance between slices can be changed by the user, the sum of these distances represents the model width. The 2D triangular elements are now prismatic six-node 3D elements.

After the 3D model is generated the next step is always to define the problem class. In this phase, it's when the different settings of the project need to be provided in order to represent the 'reality'. Therefore, the flow was simulated with via standard groundwater-flow equation (saturated), and only transport of heat in a transient state was considered. When this is all set, the task of assigning model parameters occurs. Initial temperature, boundary conditions, material properties are assigned to the elements and element nodes. Finally, by selecting element edges it is possible to assign 1D special elements named Discrete features, it represents a high-conductivity feature that can be used to represent tunnels, pipes, fractures and drains. These features are governed by three different flow laws: Manning-Strickler, Hagen-Poiseuille, and Darcy. The details of the three laws are presented in Table 4.1. For this study, the Hagen-Poiseuille law was considered since the pipes adopted in the models are cylindrical with constant cross-sections. The governing laws can be consulted in Appendix A.

Table 4.1: Discrete features laws presented in the FEFLOW software

Law	Details
Manning-Strickler	Describes the average fluid velocity in free surface.
Hagen-Poiseuille	Describes a flow of an incompressible and Newtonian fluid flowing through a cylindrical pipe of the constant cross-section.
Darcy	Describes the fluid flow through a porous medium.

4.2 Validation against existing numerical study

The following section will focus on a numerical analysis and model validation. The software was tested with the values and model geometry established by Sailer (2020), an author that performed a parametric study based on the field test performed at the Shanghai Museum of Natural History by Xia et al. (2012). This analysis relies a lot on time-steps and mesh refinement, due to the forced convection discrete features used to represent the pipes. With the help of the finite element software FEFLOW, it was possible to design different meshes to represent the model.

4.2.1 Model geometry and pipe configuration

This section will focus on the values assumed for the geometry and material properties used in this model. The model geometry is based on the literature that examined in this specific case study, Di Donna et al. (2017) and Sailer (2020). Both used the following dimensions to represent the model: 40 m high, a width of 2.25 m and length of 10 m, and the wall geometry was 38 m high, 1 m thickness, and a width of 2.25 m, as presented in Figure 3.5. The excavation depth at the time when the test was undertaken was set to 18.5 m. The shape of the pipework installed was a U-shaped pipe. The pipes were installed 10 cm from the soil side and the spacing between the inlet and outlet nodes was set to

0.75 m. However, Xia et al. (2012) does not state, a distance between the wall base and the horizontal pipe branch. Therefore, it was decided to use the same distance assumed by Di Donna et al. (2017) and Sailer (2020), 0.25 m. Details of the pipe modelled are summarized in Table 4.2. Figure 4.1 illustrates a cross-section of the top of the wall and the heat exchanger pipes layout.

Table 4.2: Geometric parameters of the pipes

Total cross sectional area, $A[mm^2]$	346.851
Pipe outer diameter, $d_0[mm]$	25
Pipe inner diameter, $d_i[mm]$	20.4
Pipe length, $L[m]$	76.25

4.2.2 Material properties and heat carrier fluid properties

The parameters applied to the fluid that runs through the heat exchanger pipes are presented in Table 4.3. Xia et al. (2012) and Sailer (2020) reported the use of water as a heat carrier fluid. The velocity of the liquid was set to 0.6 m/s, where the inlet and outlet node were assigned a negative and positive value, respectively. The thermo-physical properties of the model used by Sailer (2020) are all presented in Table 4.3. In fact, the values used for the bulk thermal conductivity, λ considered for the concrete are not typical, and the majority of studies use values greater than 2.0 $[W/m/K]$ (Barla et al. 2020; Di Donna et al. 2017; Di Donna et al. 2021; Markasis et al. 2020). The simulations performed do not consider groundwater flow.

Table 4.3: Material properties of the wall and soil presented by Sailer et al. 2020

	Geostructure	Soil	Heat Carrier Fluid
Porosity $n[-]$	0	0.25	-
Horizontal hydraulic conductivity, $k_x = k_z[m/s]$	0	10^{-4}	-
Vertical hydraulic conductivity, $k_y[m/s]$	0	10^{-4}	-
Bulk volumetric heat capacity, $c\rho[MJm^{-3}K]$	2.615	2.656	4.2
Bulk thermal conductivity, $\lambda[Wm^{-1}K^{-1}]$	1.6	2.1	0.6
Bulk density, $\rho[kgm^{-3}]$	2500	2000	1000

4.2.3 Initial temperature and boundary conditions

In the field tests performed by Xia et al. (2012), it is reported a use of three different inlet water temperatures, 32ºC, 35ºC, and 38ºC. For this study, a constant value of 35ºC was considered. The author also reported an average soil temperature of 16.3ºC, and an average temperature of 23ºC for the wall

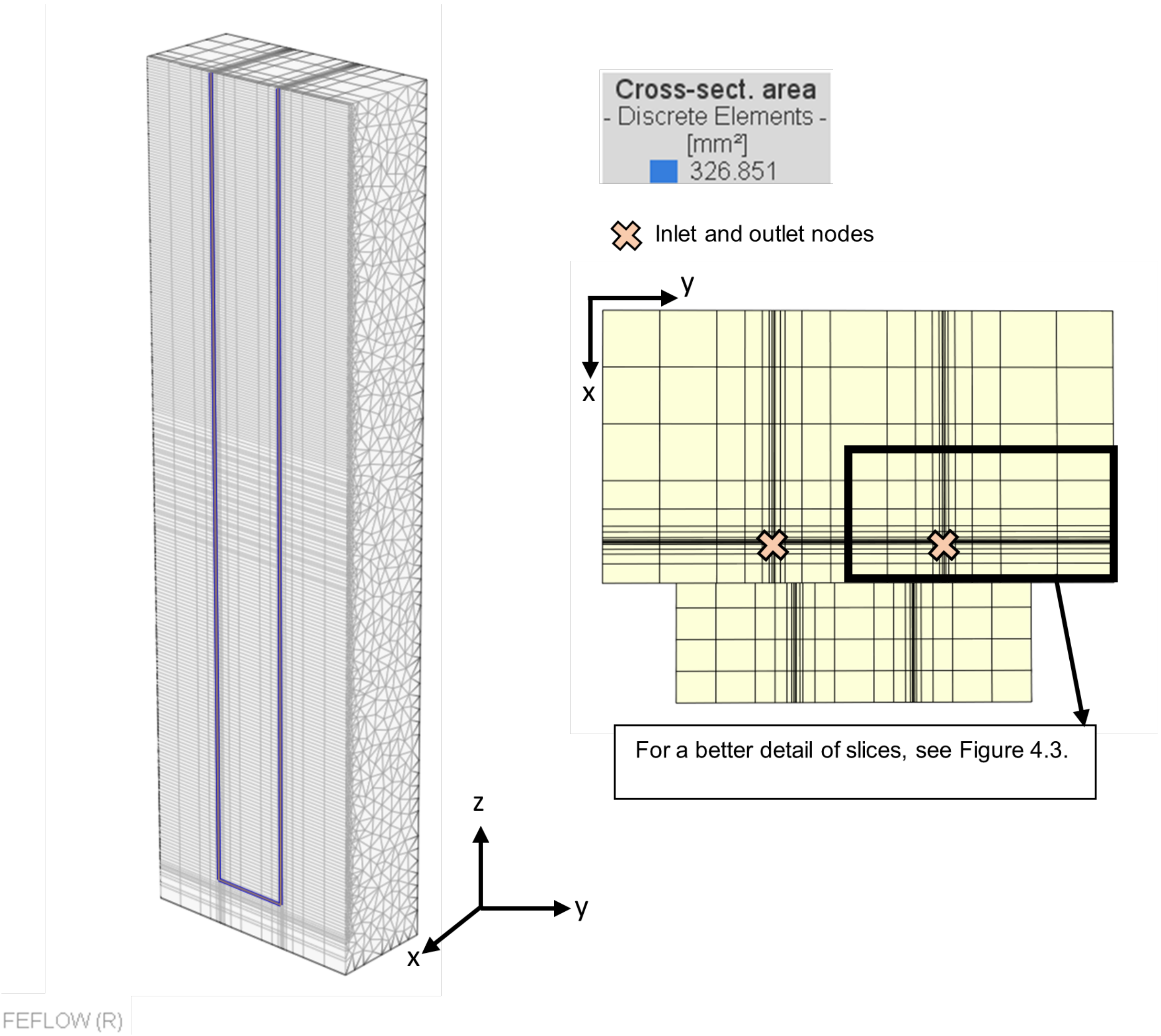

For a better detail of slices, see Figure 4.3.

Figure 4.1: Heat exchanger pipe layout and top cross section of the model with inlet and outlet nodes highlighted

at the beginning of the field test. However, Sailer (2020) assumed an initial temperature of both the wall and soil of 23ºC, therefore, these values were used as a reference. For the boundary conditions, the use of the temperature boundary conditions was considered, this means assuming temperatures to the boundary of the model since, FEFLOW software assumes all model boundaries to be adiabatic if no boundary is installed, therefore, energy cannot flow into or out of the model. A heat-flux boundary condition was considered over a fixed temperature boundary condition. This boundary presupposes a fixed heat flux across a model boundary (Neumann boundary condition). Additionally, all boundaries were set to 0 $[J/m^2/d]$ excepting the inlet and outlet node. For the inlet node it was set with a fixed, constant temperature of 35ºC, and at the outlet node no boundary condition was applied.

4.2.4 Meshes reproduced and time-step length

After some simulations, it was possible to notice that the refinement and the amount of elements are crucial parameters and can have a huge impact on the results. Therefore, a different set of meshes were reproduced. Using the parameters presented in the previous sections, it was possible to understand the impact of these two variables in the accuracy and stability of the results. Table 4.4 presents the different properties of each mesh. The refinement was focused around the heat exchanger pipe and on the wall itself. To help the refinement, some continuous alignments were defined closer to the heat exchanger pipe with different distances. Therefore, Figure 4.3 shows the different three-dimensional (3D) geometries, while figure 4.2 presents the two-dimensional configurations adopted for each mesh in this study.

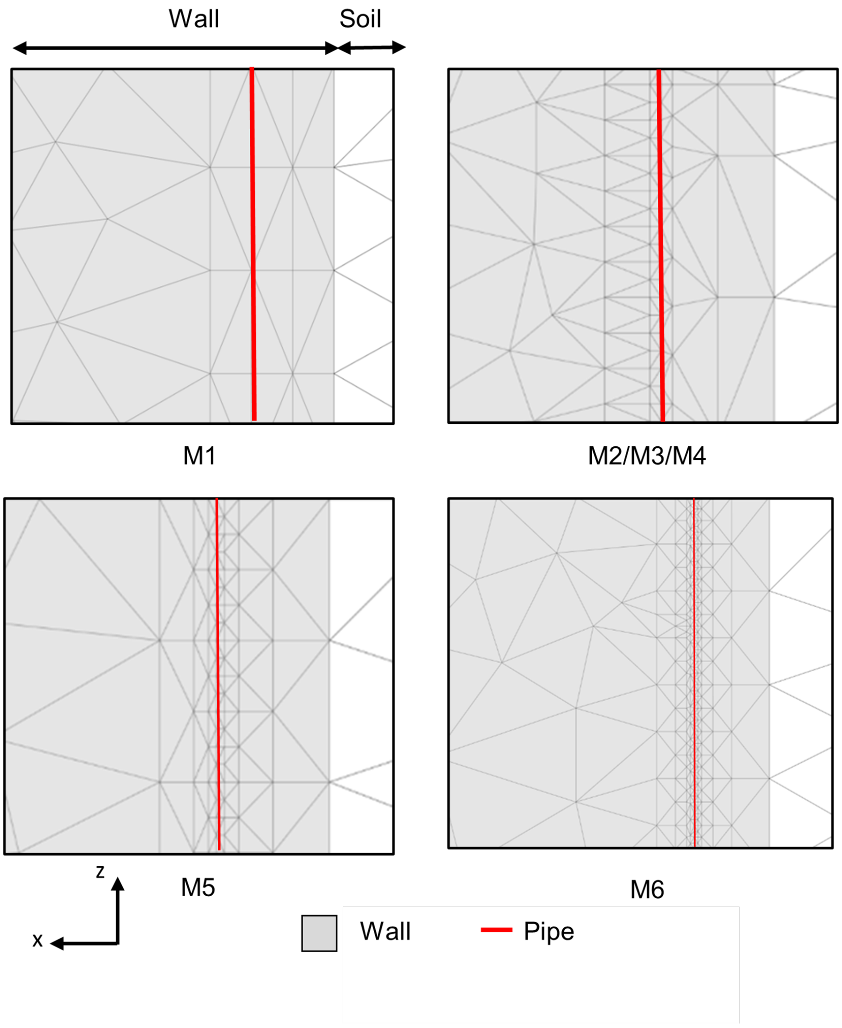

Figure 4.2: Schematic representation of the meshes in the 2D configuration from M1 to M6

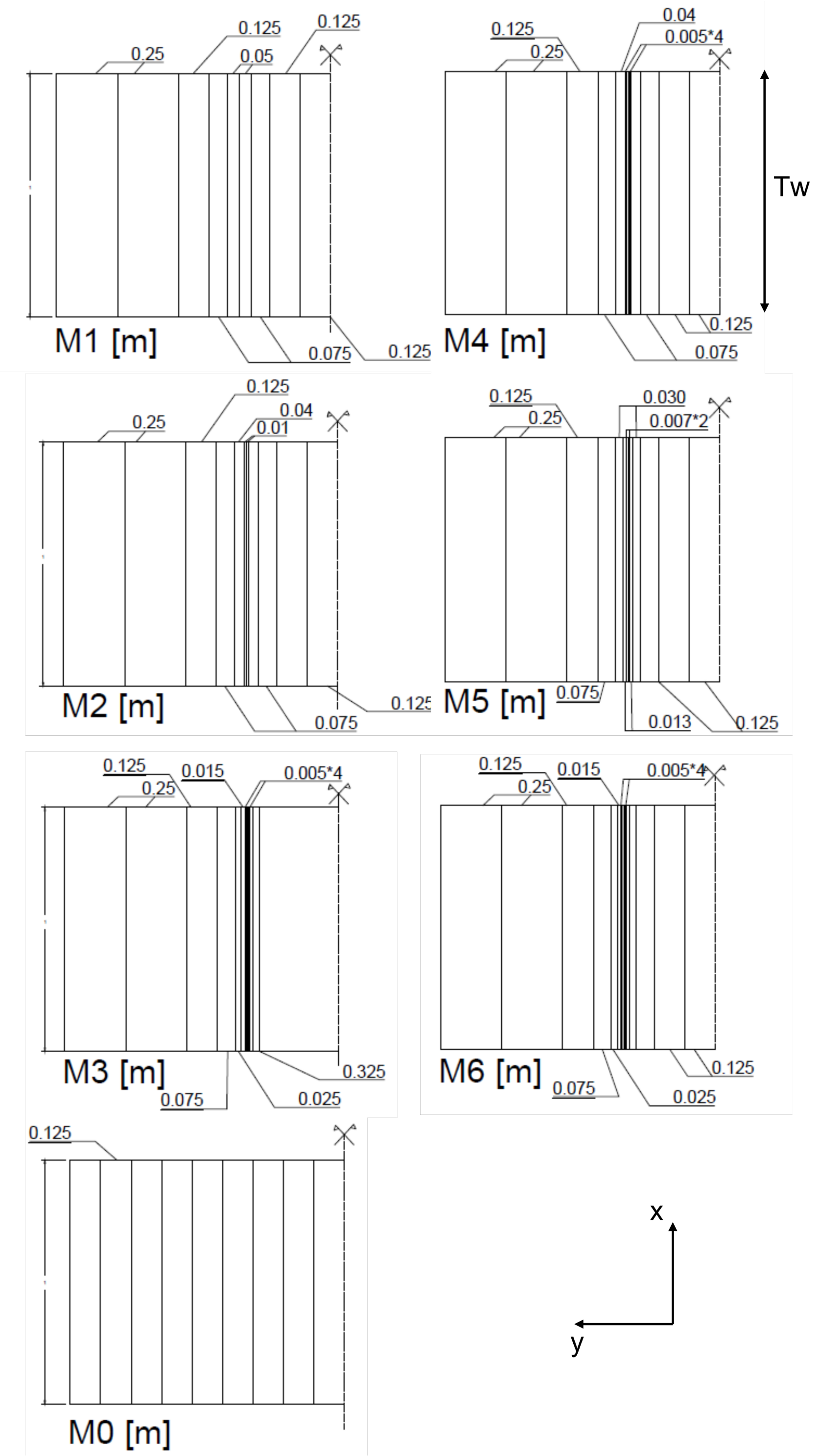

Figure 4.3: Plan view of wall section, illustrating slice locations in plane of wall.

In addition, considering that the heat exchanger pipe is installed 0.1 m from the soil side, the meshes that were generated, had different continuous alignments that were applied close to the pipe, in order to generate a better mesh and simplify the software modulation due to forced convection and high temperature gradients. Therefore, the three-dimensional layer was set to have these continuous alignments as well with the same distances. However, meshes M3 and M4 were reproduced with different distances in the 2D configuration when compared to the 3D layers configuration. Therefore, we can consider these meshes to be unsymmetrical.

Table 4.4: Properties of the meshes used in this study.

Mesh	#Elements	#Nodes	#Nodes per slice	#Slices	Refinement	Approx. Run Time
M0	143388	77919	4101	19	Wall and pipe	0.25 hours
M1	166732	90414	5023	18	Wall and pipe	1 hour
M2	463092	245278	11149	22	Wall and pipe	1 day
M3	551300	289874	11149	26	Wall and pipe	1.5 days
M4	507196	267576	11149	24	Wall and pipe	1 day
M5	587350	307346	11821	26	Wall and pipe	2 days
M6	1554951	806640	26888	30	Wall and pipe	10% at 2 weeks

Since the mesh is more refined and the simulation is set to 2 days, it is necessary to take into account the time-step duration and the number of time-steps. The first, represents the length of each single time step in default time unit. As for the latter, it represents the number of time steps that need to be calculated to solve the system of equations in FEFlow. Additionally, these simulations have high temperature gradients and works in a forced convection environment, therefore convergence problems can be expected. To solve this, the insertion of a smaller time-step length increases the simplicity and the software can easily calculate the progression of the high temperature gradients. Considering that the meshes used in this study have a considerable amount of elements and nodes a custom time-step length was inserted manually to the minimum and maximum time-step lengths used by the software. Table 4.5 shows the initial, minimum and maximum time-step length used for the simulations.

Table 4.5: Time steps adopted in days

Time-step	Initial time-step length	Minimum time-step length	Maximum time-step length
T1	$10^{-12}[d]$	$10^{-12}[d]$	$10^{-8}[d]$

4.3 Results and discussion

The effect of the meshes and results that were investigated are discussed and presented in the following subsections. There is a comparison between the heat transfer values obtained by the modelling and the values presented by Sailer (2020) in order to understand the mesh refinement impact.

4.3.1 Heat transfer rate

The results of the simulations are presented in terms of outlet temperature. Therefore, the exchanged power, $Q[W]$ and the heat transfer rate per meter of pipe, $q[W/m]$ can be calculated using the following equations:

$$Q = mc_w(T_i - T_o) \tag{4.1}$$

$$q_L = \frac{Q}{L} \tag{4.2}$$

Where c_w represents the specific heat capacity of the fluid $[J/(kg/K)]$; T_{in} and T_{out} are the inlet and outlet fluid temperatures; and m is the mass flow rate in the pipes $[kg/s]$.

4.3.2 Influence of the mesh

After some simulations, it was possible to notice some inconsistency in the results depending on the mesh that was being used. Therefore, a comparison was made with the results obtained from Sailer (2020). Due to the fact that this work back analysed the case presented by Xia et al. (2012). The mesh used is extremely refined and the software used by Sailer (2020) allows the use of transition elements. This type of elements are secondary elements normally placed between elements to help the software to perform with higher precision. The simulations performed used the same time-step lengths presented in order to have always the same time increment, presented in section 4.2.4.

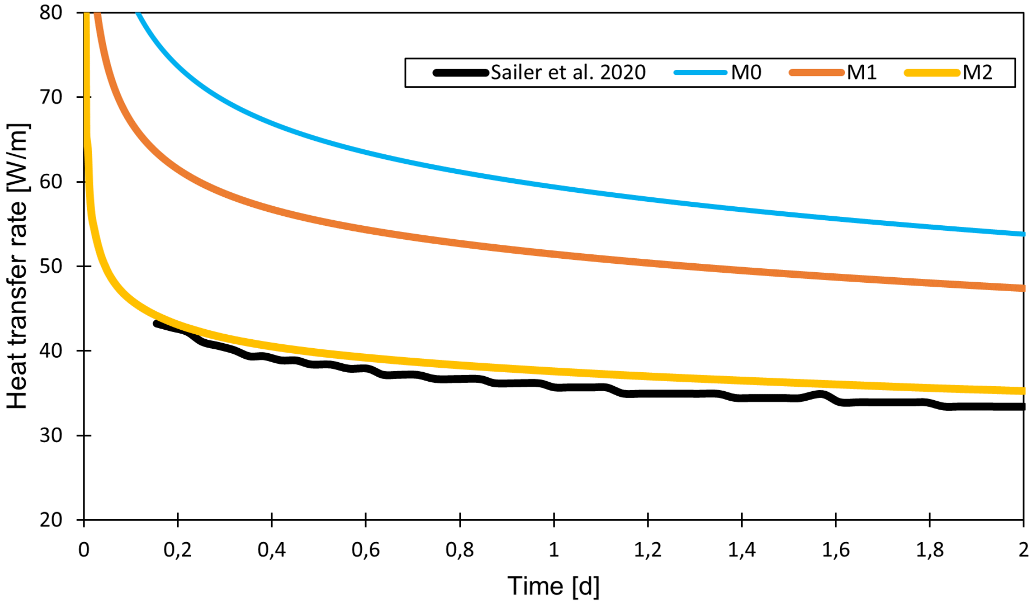

Figure 4.4: Results obtained for 2 days of simulation for M0, M1 and M2 when compared to the results presented by Sailer et al. 2020

The first simulation was performed with the mesh type M0 a simple mesh, the 3D configuration of this mesh was set to be slice equally spaced with a width of 2.25m. Subsequently mesh type M1 was simulated, a refined mesh but with a lower number of elements when compared with other authors (Di Donna, 2021). Figure 4.4, presents the evolution of the heat transfer rate for 2 days of simulation, and it is possible to notice a considerable difference when compared to Sailer (2020), the values obtained for the heat exchange rate after 2 days were 53.8$[W/m]$ and 47.4$[W/m]$ for meshes type M0 and M1 respectively. These values were 30.4% and 38.5% larger than reported by Sailer (2020), for mesh MO and M1 respectively. Therefore, a third simulation was performed considering mesh M2, this mesh has a number of elements almost three times greater than mesh type M1 (Table 4.4). The results are also presented in Figure 4.4, and show a better agreement with the results presented by Sailer (2020), and the final heat exchange rate obtained is only 6.4% greater.

4.3.3 Results for the meshes reproduced

Taking into account this behaviour, four additional simulations were performed using meshes M3, M4, M5 and M6. However, performing the analysis with mesh type M6 was not possible, due to the high amount of elements and nodes the computational requirements were too high, therefore, M6 results are not presented in the following charts.

Figure 4.5 focuses only on the combination of mesh types M2, M3, M4 and M5, when compared to the values obtained by Sailer.

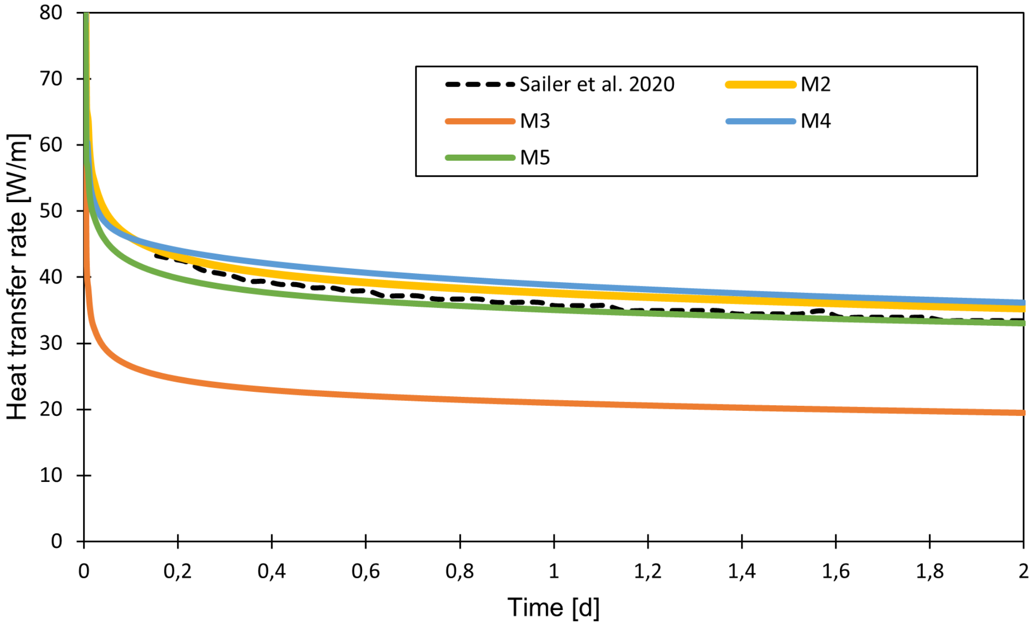

Figure 4.5: Results obtained for 2 days of simulation for M2, M3, M4 and M5 when compared to the results presented by Sailer et al. 2020

It is possible to notice that all meshes showed good convergence with the considered time-steps when comparing to the 2 day mark Table 4.6, M5 differed by only 1.4% (33.05$[W/m]$) from Sailer (2020). On the other hand, M3 and M4 showed a difference of 15.4% (39$[W/m]$) and 8.7% (36.14$[W/m]$) respectively. The performance of meshes M2 and M5 showed a better agreement with the results presented by Sailer (2020).

Table 4.6: Numerical results of outlet temperature, heat transfer rate and error percentage compared with Sailer values

Mesh	Outlet temperature, $T_{out}[C]$	Heat transfer rate, $q_L[W/m]$	Error $[\%]$
Sailer (2020)	31.95	33.00	-
M0	32.52	53.81	38.5
M1	32.81	47.41	30.4
M2	33.37	35.27	6.4
M3	33.20	38.99	15.4
M4	33.33	36.13	8.7
M5	33.47	33.04	1.4
M6	-	-	-

4.3.4 Conclusions

Through the previous results, it is possible to conclude that meshes with lesser elements and a 3D configuration with unsymmetrical characteristics when compared to the mesh plane tend to have the worst software performance (M0, M1, M3 and M4). Therefore, when working with problems with high thermal gradients and fluid flows it is important to refine the areas where these phenomema occur, in this case, the heat exchanger pipes. Another important factor, that should always be taken into consideration is to keep a symmetrical configuration between the two-dimensional (2D) plane and the three-dimensional (3D) plane.

4.4 Validation with field test

Taking into consideration that the amount of field tests performed is limited, the field test reported by Xia et al. (2012) at the Shanghai Museum of Natural History was used as a reference in the following section. This subsequent part, will take into consideration new values for several parameters of the model and study the impact of them in the numerical simulation results when comparing them with the results presented by Xia. These simulations will be undertaken using mesh type M5 and time-step lengths, presented in Section 4.3.3.

The following simulations were performed alternating three parameters: initial temperature of the wall and soil, boundary conditions and thermal conductivity of the energy wall.

4.4.1 Initial temperature and boundary conditions

The values adopted for the initial temperature and boundary conditions of the study are presented in the following section. Xia et al. (2012) reported different temperature values of 12.2ºC, 25.0ºC, and 21.2ºC at 9 m, 25 m, and 35 m from the top of the wall, one day before the field test. Therefore, some of the numerical simulations performed considered a different initial temperature in the exposed part and embedded part of the wall, as presented in Figure 4.6 a). The author also mentions that at the beginning of the experiment the average temperature of the diaphragm wall and soil is 23.0 ºC and 16.3 ºC respectively. The temperature of the wall for the exposed part is compatible with the air temperatures of Shanghai. The average temperature of Shanghai for the summer and winter is respectively 29.5 ºC and 9.5 ºC, therefore, for subsequent simulations these values were considered to boundaries of the model. Figure 4.6 b) presents the different boundaries of the model, each of them is associated to a different letter from A to F. Boundaries A, B and F are subject to variation due to their contact with the air, boundaries C, D, and E assume a No heat flux (NHF).

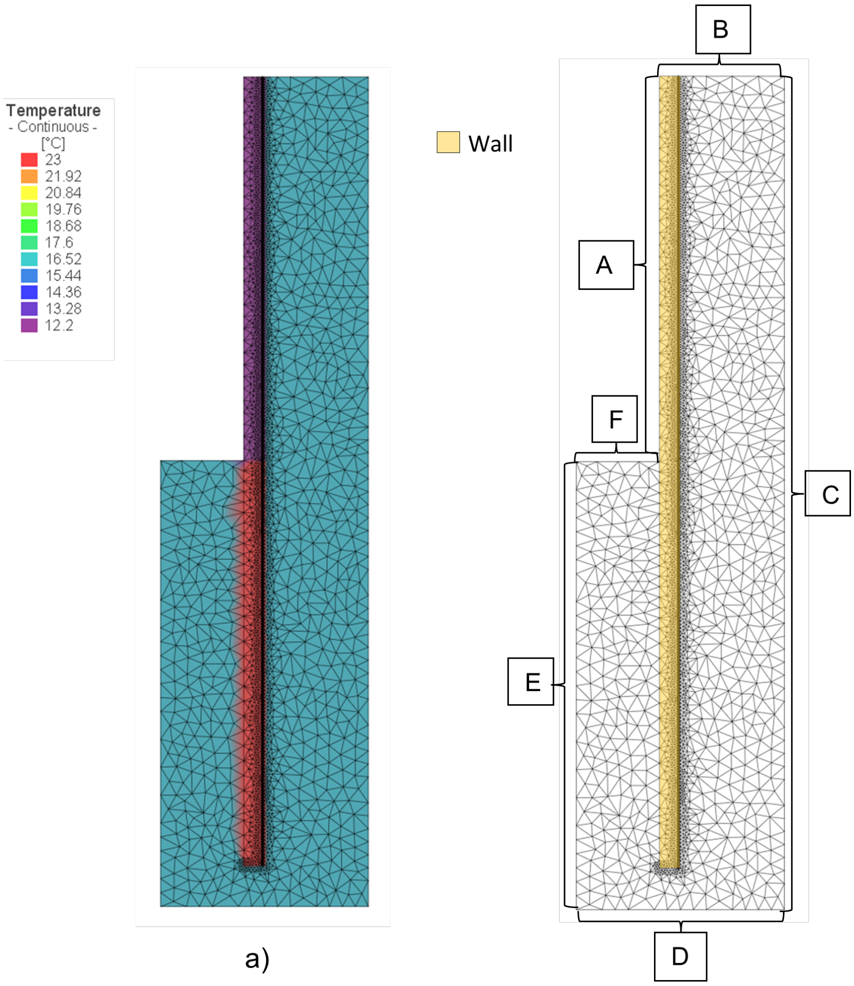

a)

b)

Figure 4.6: Influence of initial temperature and boundary conditions: a) Initial temperature distribution along the model; b) definition of the different boundary conditions of the model.

4.4.2 Energy wall and soil parameters

Table 4.3 lists the thermal-physical properties of the model, assumed in this study and used by Sailer (2020).

One of the most important energy wall parameters, to take into consideration is the thermal conductivity of the concrete. A number of studies, adopt values over 2.0 $[W/m/K]$ (Barla et al. 2020; Di Donna et al. 2017; Di Donna et al. 2021; Markasis et al. 2020). However, in this study the same value used by Sailer (2020) was adopted, 1.6 $[W/m/K]$. This assumption is adopted since Xia et al. (2012) does not provide specifications on the aggregate used, and the choice was also based on Tatro (2006).

4.4.3 Simulations performed

The simulations that were performed are presented in Table 4.7.

Table 4.7: Simulations performed in this study

Run	T_{soil}: $[C]$	T_{top}: $[C]$	T_{bot}: $[C]$	A	F	B	λ_{conc}: $W/m/K$
Base	23	23	23	NHF	NHF	NHF	1.6
1 summer	23	23	23	29.5	29.5	NHF	1.6
1 winter	23	23	23	9.5	9.5	NHF	1.6
2 summer	23	23	23	29.5	29.5	29.5	1.6
2 winter	23	23	23	9.5	9.5	9.5	1.6
3	23	12.2	23	NHF	NHF	NHF	1.6
4	16.3	23	23	NHF	NHF	NHF	1.6
5	23	23	23	NHF	NHF	NHF	2.0
6	23	12.2	23	NHF	NHF	NHF	2.0
7	16.3	12.2	23	NHF	NHF	NHF	2.0
8	16.3	12.2	23	NHF	NHF	NHF	1.6
9 summer	23	12.2	23	29.5	29.5	NHF	2.0
9 winter	23	12.2	23	9.5	9.5	NHF	2.0
10 summer	16.3	12.2	16.3	29.5	29.5	NHF	2.0
10 winter	16.3	12.2	16.3	9.5	9.5	NHF	2.0
11 summer	16.3	12.2	23	29.5	29.5	NHF	2.0
11 winter	16.3	12.2	23	9.5	9.5	NHF	2.0

4.5 Results and discussion

The following subsection will focus on comparing the values obtained with the field tests obtained by Xia et al. (2012) and the values obtained in this study. Table 4.8 presents the values obtained for outlet temperature and heat transfer rate as well its accuracy in percent when compared to Xia's 50 $[W/m]$ value, for an U-shaped pipe configuration and Sailer's numerical results, 33.41 $[W/m]$.

4.5.1 Influence of boundary conditions

The first two simulations performed took into consideration the values of the average annual temperature of Shanghai for the summer and winter seasons. Considering that Xia performed this field test in the period between March and July, it is expected that the accuracy of the results for the summer season

Table 4.8: Validation against field test analysis results

Run	Outlet temperature	Heat transfer rate	Diference to Xia	Diference to Sailer
#	$T_{out}[C]$	$q_L[W/m]$	[%]	[%]
1 summer	33.50	32.31	35.38	-3.4
1 winter	33.42	34.19	31.63	2.27
2 summer	33.51	32.20	35.60	-3.75
2 winter	33.40	34.48	31.04	3.1
3	33.10	41.06	17.87	18.64
4	33.14	40.25	19.5	17
5	33.19	39.08	21.84	14.51
6	32.73	48.99	2.02	31.8
7	32.34	57.53	-15.06	41.92
8	32.83	46.78	6.44	28.58
9 summer	33.87	46.08	7.83	27.5
9 winter	32.71	49.45	1.09	32.44
10 summer	32.47	54.64	-9.27	38.85
10 winter	32.14	61.75	-23.50	45.89
11 summer	32.47	54.62	-9.25	38.84
11 winter	32.41	55.97	-11.95	40.31

should be higher. Therefore, run 1 summer and 1 winter took into consideration different boundary conditions. To the boundaries that are exposed to the exterior environment (A and F), constant temperature boundary conditions were applied while boundary B was maintained as adiabatic. For the first run, summer temperature was applied 29.5ºC and for the second winter 9.5ºC. However, the inlet temperature of the heat exchanger pipe was unchanged, 35ºC with a fluid velocity of 0.6$[m/s]$. For simulation 2 summer and 2 winter, boundaries A, B and F, the same constant temperature boundary conditions were adopted. The results obtained for both sets of simulations are compared to the values obtained by Xia et al. (2012) in Figure 4.7. The heat transfer rate for summer at the end of the simulation, yielded a decrease of 3.3% and 3.6% for runs 1 and 2 respectively relative to the result of Sailer (2020). However, an increase was found for the winter cases, 2.27% for run 1 and 3.1% for run 2. When comparing runs 1 and 2, it is also noticed a small discrepancy, which means that there is an influence of the top boundary of the model (B). But since this parameter was not significant to the results after 2 days of simulation, no comparison was made with the field test data presented by Xia.

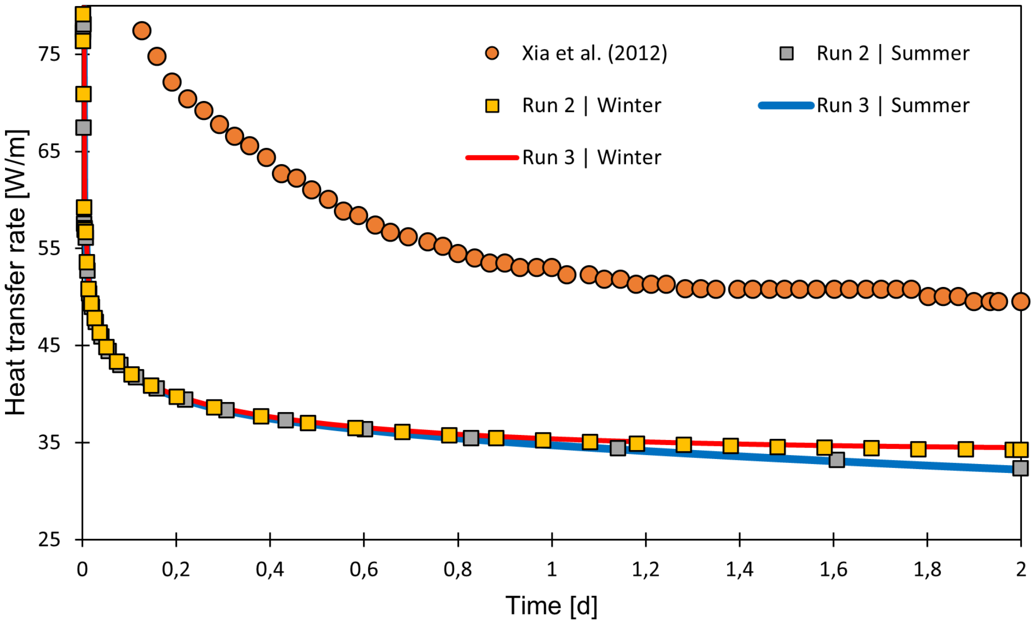

Figure 4.7: Results obtained for 2 days of simulation for runs: 1 summer, 1 winter, 2 summer and 2 winter.

4.5.2 Influence of initial wall and soil temperature

While previous numerical studies simply assumed the average wall temperature reported by Xia et al. (2012), it was appointed that the upper part of the wall was at a lower temperature than the bottom part which is buried in the ground. Therefore, runs 3, 4, and 8 were performed to take this into consideration. Xia et al. (2012) reported different temperature values of 12.2ºC, 25.0ºC and 21.2ºC for 9 m, 25 m, and 35 m depth of the wall one day before the field test. Therefore, the initial temperature for the soil and upper part of the wall were set to values presented in Table 4.7, while the embedded part of the wall was assigned an initial temperature of 23ºC. Therefore, since these were the real values before the field tests, for all simulations it was adopted a value of 23ºC (also reported by Xia) for the bottom wall temperature.

After analysing the results with the help of Figure 4.8, for the first 0.7 days the results are dissimilar. Run 4 presented an earlier stabilization of the values, as for run 3 and 8 it took more time. For the 2 day mark a significant increase of the values can be observed when compared to Sailer's results. Run 3 presents an increase of 18.6% almost the same increase as run 4 (17%). In run 8 higher heat exchange rates were obtained compared to the previous runs, this increase of 29% lead to a better agreement with the field results presented by Xia, an accuracy of 93.5% was achieved.

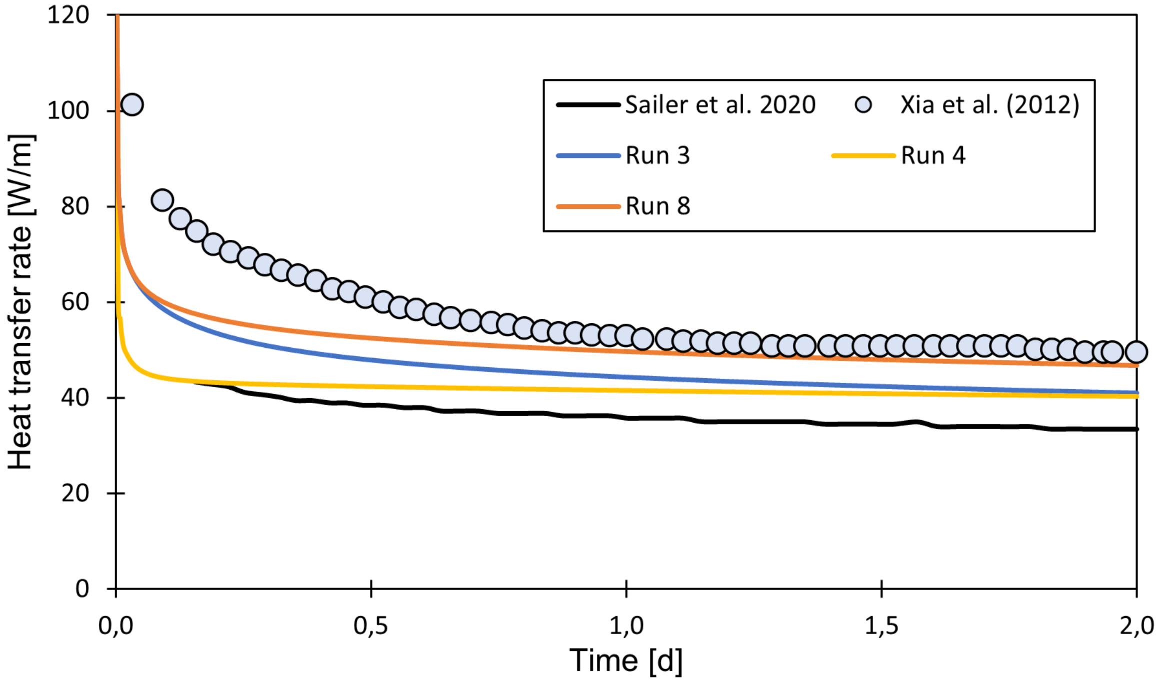

Figure 4.8: Results obtained for 2 days of simulation for runs: 3, 4 and 8

4.5.3 Influence of thermal conductivity of the concrete

The thermal conductivity of the concrete is a parameter that is not constant to all projects, since its properties can vary significantly. In order to understand the importance of this parameter, runs 5, 6 and 7 were performed. These runs adopted the same values as previous simulations to certain parameters, such as initial temperature and boundary conditions, presented on Table 4.7 Figure 4.9 presents the impact of the thermal conductivity of the concrete.

In run 5 the heat exchange rate increases approximately 15.7%, when compared to Sailer's results, and it shows a 78% accuracy when compared to Xia. Subsequently, run 6 presented a heat exchange rate of 48.9$[W/m]$, an increase of 16% when compared to run 3, and an accuracy of 98% was achieved with respect to the field tests performed in Shanghai. In the previous subsection run 8 combined the changes for run 3 and 4 and yielded a close comparison with the results of Xia et al. (2020). In run 7, which analysed the same conditions as run 8 but with an increased concrete thermal conductivity, a value of 57.53$[W/m]$ was obtained at the end of the 2 days of simulation. This represents an increase of 18.7% when compared to run 8, and an accuracy of only 87% when compared to Xia's.

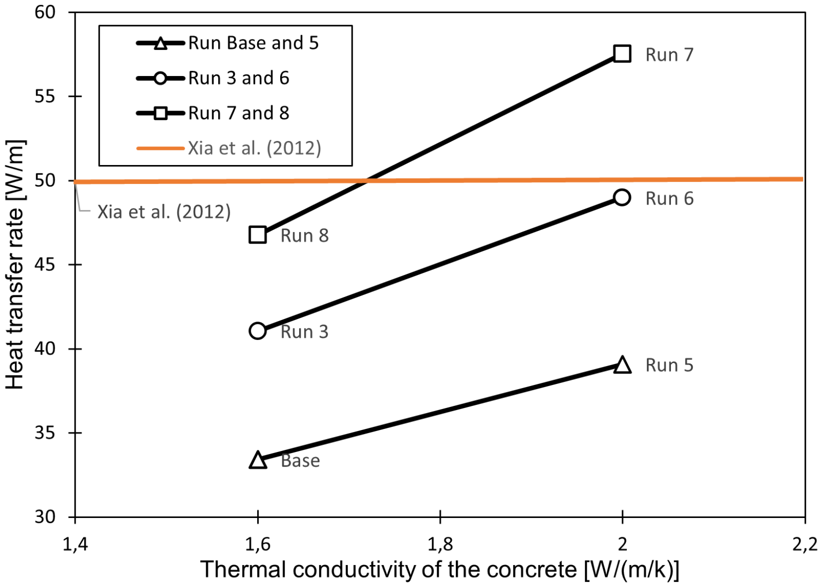

Figure 4.9: Results obtained for 2 days of simulation for concrete thermal conductivity variation

4.5.4 Extra simulations performed

Due to the results obtained, three extra simulations were performed, runs 9, 10, and 11. These runs took into consideration the boundary conditions of summer and winter, the initial temperature configuration presented in figure 4.10 as well as, the value of 2$[W/m]$ for the thermal conductivity of the concrete. The main objective of these simulations is to study the effect of the three parameters at the same time.

Run 9 with winter boundary presents an increase of 1.4% when compared to run 6. As for the summer boundary a decrease of 6.3% is verified. The most important aspect to take into consideration with simulation number 9 is, the accuracy presented by this particular simulation. Run 9 with winter boundary conditions presented an accuracy of 98.9%, the summer boundary in contrast only showed a 92.1%. The same scenario was performed for run 11 and run 7. However, for this case the values obtained for the temperature boundary conditions lead to a decrease in the heat exchanger rate. A total of, 5% and 2.7% are verified for the summer and winter respectively.

The last simulation performed, was not compared to any other simulation, since this specific simulation took into consideration one value that is not justified by Xia. Therefore, the initial temperature to the bottom part of the wall is merely adopted just to see the behaviour of the model to this particular change. When comparing this simulation with the field tests performed by Xia, the accuracy of the values is a bit lower when compared to other simulations. The winter boundary presented only 81%, and summer 92% when compared to Xia et al. (2012).

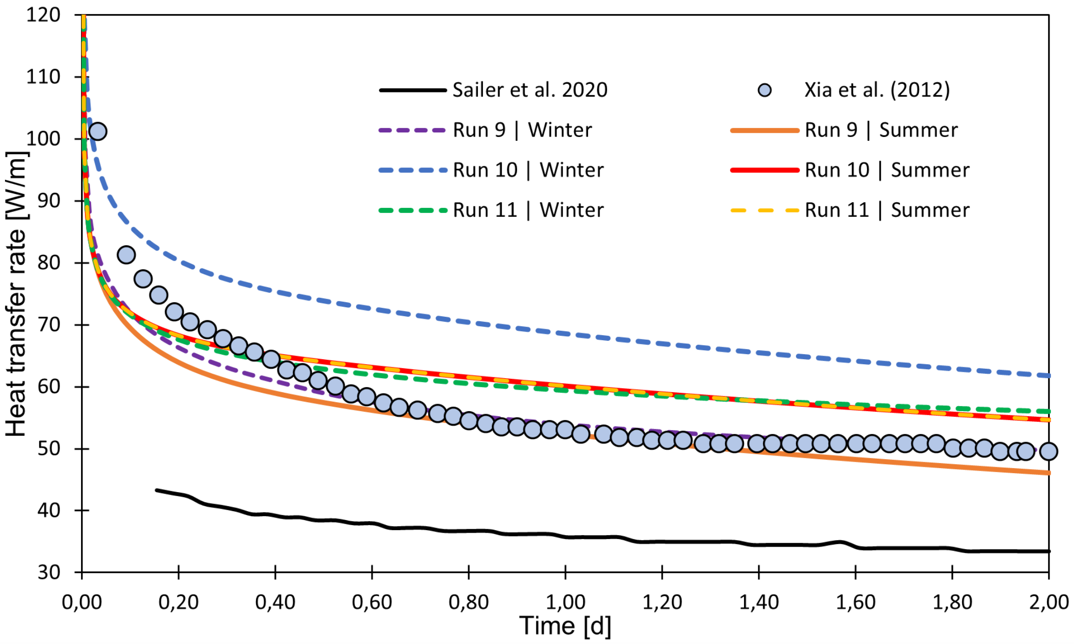

Figure 4.10: Results obtained for 2 days of simulation for runs: 8, 9 and 10 for winter and summer boundaries

4.6 Soil characterization

The soil parameters that need to be inserted in FEFlow in order to do a full characterization are porosity, hydraulic conductivity, the volumetric heat capacity of the solid, volumetric heat capacity of the liquid and thermal conductivity of both solid and liquid. Therefore, considering the location of the Shanghai Museum of Natural History a research was made in order to find geotechnical profiles already established by other authors, close to this location, to obtain these soil parameters. Huo et al. (2011) performed a study on the deformation of a retaining structure of pit-in-pit excavation at the Shanghai Museum of Natural History and at Metro Line 13. The author presented the soil layers and their properties, including the void ratio. With this parameter, it is possible to determine the porosity of the layers. This dimensionless parameter can be calculated with the following equation:

$$\eta = \frac{V_v}{V} = \frac{e}{1+e} \tag{4.3}$$

Where n represents the porosity, V_v represents the volume of voids and V, the total volume of soil. Considering the computational requirements needed to perform the simulations a simplification of the layers was designed. Instead of having seven different layers, Figure 4.11 presents the profile adopted for the model and the respective layers which were reduced to three: silty clay, soft silty clay and sand. The values adopted for the porosity were simplified as well.

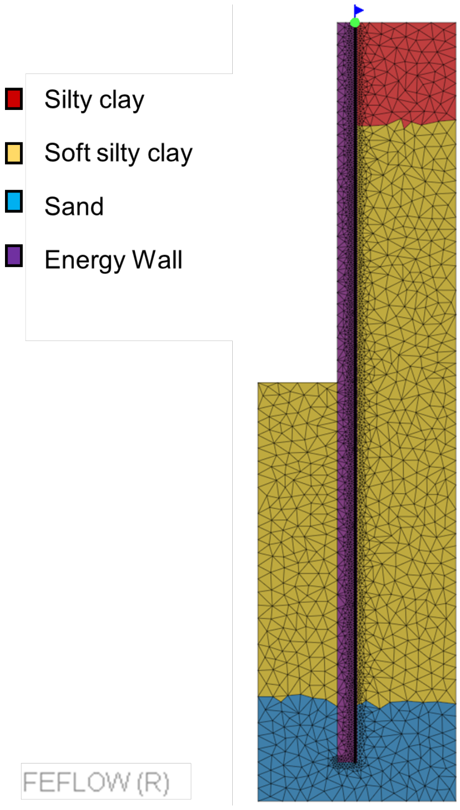

Figure 4.11: Schematic representation of the model adopted

The volumetric heat capacity of the soil is another parameter required by FEFlow. According to Rees (2000), the heat capacity of the soils can be calculated with the following equation:

$$c = \chi_1\rho_1c_1 + \chi_2\rho_2c_2 + \chi_3\rho_3c_3 \tag{4.4}$$

Therefore, the calculation for the sand layer and clay layer were made. The values of χ_1, χ_2 and χ_3 represent volume fractions of three constituents of soil, solid, water and air respectively. These parameters can be determined with the help of the following equations:

$$\chi_1 = 1 - \eta \tag{4.5}$$

$$\chi_2 = \eta(S_1) \tag{4.6}$$

$$\chi_3 = \eta(1 - S_1) \tag{4.7}$$

Since the soil is considered to be fully saturate S_1 is considered unitary. The values of ρ_1, ρ_2 and

ρ_3 and c_1 c_2 c_3 were set to solid, water and air as well. Table 4.9 presents the values adopted for each variable of the equation for the layers and the values obtained.

Table 4.9: Values adopted for the calculation of the specific heat capacity of the soil

	Sand	Clay	Designation
χ_1	0.5	0.5	Porosity
χ_2	0.5	0.5	
χ_3	0	0	
ρ_1	1700	1760	Density $[kg/m^3]$
ρ_2	1000	1000	
ρ_3	1.25	1.25	
c_1	780	878	Specific heat capacity $[J/(Kg * K)]$
c_1	4186	4186	
c_1	1.256	1.256	
c	2.75	2.87	Volumetric heat capacity $[J/K/m^3]$

The thermal parameter values for the thermal conductivity of the soil were defined with the aid of an investigation performed by Chen et al. (2018) and a study presented by Côté and Konrad (2005). Chen et al. (2018) investigated the thermal conductivity of soft clays that are present in Shanghai. Soil samples were obtained from a construction site in Shanghai, including silty clay. The test performed on the soil was employed with the aid of a KD2 Pro thermal property analyzer. Chen et al. (2018) also presents, that the thermal conductivity of these soils have a relationship with the void ratio, water content and temperature of the soil.

Therefore, considering the void ratios and water content presented by Huo (2011) and a temperature range of 25-75 ºC it was possible to deduce a value of approximately 1.3 $[W/m/K]$ for the thermal conductivity of the silty clay and soft silty clay. As for the last layer of soil considered, Côté and Konrad (2005), mention that Johansen (1975), gave the best prediction to calculate the thermal conductivity for sands. It presents several equations used to determine the thermal conductivity of fine sands. From which a thermal conductivity of the sand of approximately 1.0 $[W/m/K]$ was obtained. Therefore, the values adopted for the soil configuration presented in figure 4.11 are presented in table 4.10.

Table 4.10: Values adopted in the simulation

Layer	Depth [m]	$\lambda_{soil}[W/m/K]$	$k_{yy} = k_{zz} = k_{xx}[m/s]$	$c[J/kg/K]$
Silty clay	8	1.3	10^{-8}	2.80
Soft silty clay	30	1.3	10^{-8}	2.87
Sand	12	1.0	10^{-4}	2.75

4.7 Results and Discussion

Some runs were reproduced once again with the new soil configuration, Figure 4.12 presents the results with and without the soil profile inserted. Base run performed by Sailer and run 6 were tested in this study.

Therefore, the chart presented represents the accuracy of the various simulations when compared with the field tests performed by Xia. No significant changes were observed for the short term period of 2 days. For Sailer's run, an increase of 0.2% was verified, as for run number 6 approximately 0% was verified.

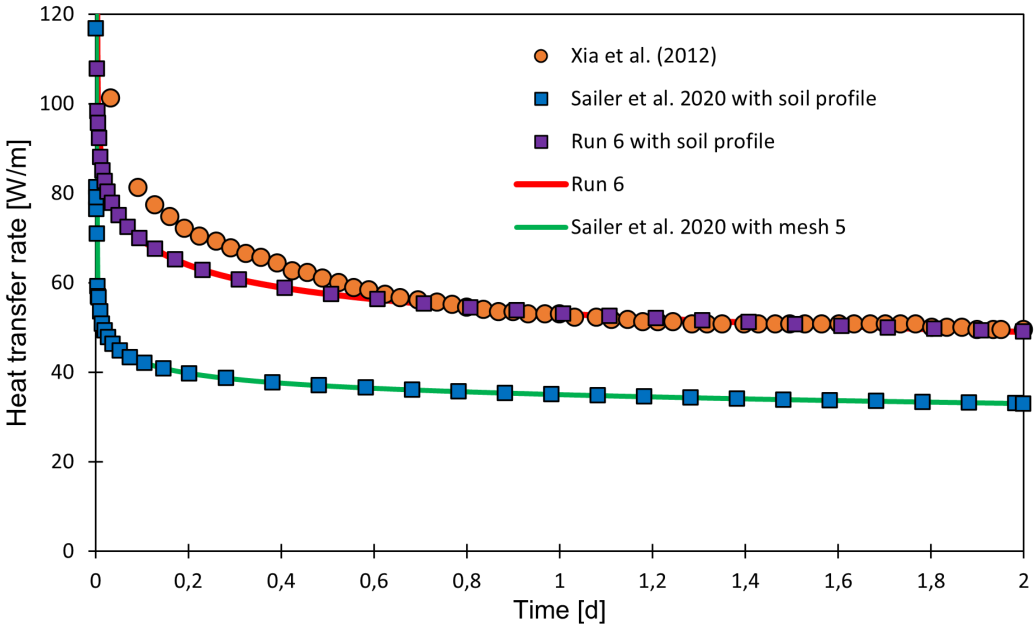

Figure 4.12: Results obtained for 2 days of simulation for runs 6 and base with and without soil profile against Xia et al. (2012) values

4.8 Conclusion

From the previous analysis, only simulations with a time frame of 2 days were performed, same time of the results presented by the field tests performed by Xia et al. (2020).

It is possible to conclude that when recreating a field test through numerical analysis, a large number of parameters can impact the results obtained. Therefore, the validation of the software response against field data is extremely important. It was possible to percieve that:

- The refinement of the mesh is extremely important when dealing with high temperature gradients;
- When working with meshes with a higher number of elements, more time is requires to run the

simulation;

- Dealing with numerical analysis with high temperature gradients and fluid discrete features, the three-dimensional configuration needs to present a similar presentation with the two-dimensional mesh, to obtain a higher accuracy on the results output.

For the parameters studied in this section, the influence of the boundary conditions is not as significant as expected, since we are dealing with a short-tterm analysis of only two days. However, winter boundary conditions presented a closer agreement with the results presented by Xia et al. (2012). Additionally, the results obtained for the simulation where the top boundary had a temperature boundary condition applied, showed better results when compared with the field tests. As for, the initial temperature of the model, for short-term simulations the results presented to be significant for the two days of simulation, however, in long-term this may not be verified. The thermal conductivity of the concrete also presented accurate and considerable results when varying the values. In addition, the soil profile performed for the model presented no significant changes to the results for short-term analysis.

Chapter 5

Numerical analysis: parametric study

5.1 Numerical analysis

The following chapter focuses on the parametric study of heat exchange through energy walls, where the thermal performance of several parameters is studied through numerical analysis. Initially, a mesh study is performed similarly to Chapter 4, adopting some simulations already performed by Silva et al. (2020). Subsequently, the main parameters studied in this chapter are the wall geometry, heat exchanger pipe configuration, and thermal conductivity of the soil.

5.2 Numerical model

The following section focuses on the numerical model established to perform the parametric study and the parameters studied.

5.2.1 Model geometry

The model geometry is proven to be one of the parameters with the biggest impact on the thermal performance of the wall, therefore, three different geometries were defined. Table 5.1 presents the values adopted for each geometry considered in this study. The geometries adopted considered different distances for values of excavation depth, however, for the buried part of the wall a value of 5 m was adopted. Unlike Chapter 4, the diaphragm wall is incorporated with a base slab to simulate real life scenarios such as underground parks and underground metro stations. Figure 5.1 a) presents a schematic representation of the energy wall. For the 3D configuration of the model, 16 layers (17 slices) for a model width of 1.6 m was considered which leads to a distance of 0.1 m per layer. The overall geometry of the model and key dimensions are shown in Figure 5.2

Table 5.1: Geometric parameters of the wall for the parametric study

Geometry	Excavation depth	Wall depth	Wall thickness	Slab thickness	Wall surface area
-	$D_e[m]$	$D_w[m]$	$T_w[m]$	$T_s[m]$	$A_w[m^2]$
G10_5	10	15	0.6	0.6	24
G20_5	20	25	0.9	0.9	40
G30_5	30	35	1.2	1.2	56

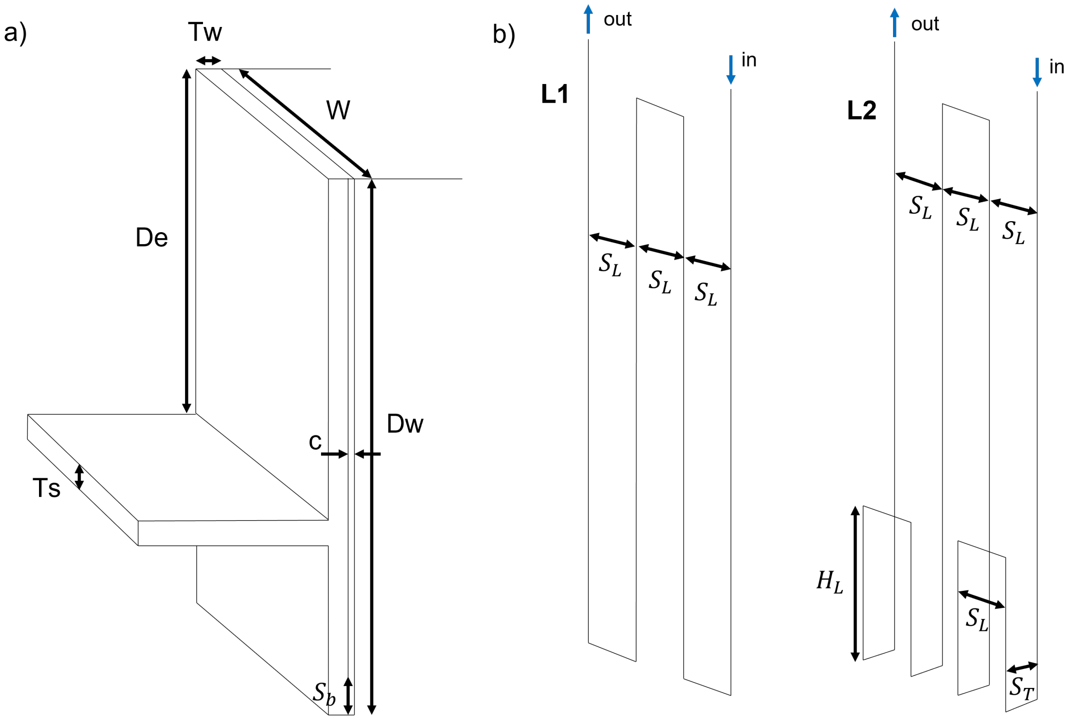

Figure 5.1: Schematic representation: a) Diaphragm wall and slab and b) Pipe configuration L1 and L2

5.2.2 Pipe configuration

According to Di Donna et al. (2017), the spacing of the heat exchanger pipes presented a significant impact, therefore, a new heat exchanger pipe layout was for seen for the parametric study. As mentioned in section 3.3.4, the layout that has the best thermal performance is not always the simpler to install during the construction of the energy diaphragm wall. Therefore, considering the work presented by Barla et al. (2020), for this chapter a W-shaped layout was considered (L1). In addition, a second layout was considered with an extra pipe in the embedded part of the wall (L2), both layouts are presented in figure 5.1.

The parameters endorsed for the heat exchanger layouts were the spacing between vertical pipe, S_p, a value of 0.4 m was adopted. Similarly to Chapter 4, the concrete cover to the pipes, c, was set to be 0.1

m and the distance from the bottom slab face, S_b, is 0.5 m. For the highest longitudinal pipe a distance of 1 m from the top boundary, S_l was adopted. For layout L2, the values adopted for the transverse spacing between vertical pipe branches S_T and the distance of the vertical loop on the embedded part of the wall S_H, are defined depending on the geometry adopted. Therefore, the equations used to determine the values of these parameters are presented:

$$S_T = T_W - 2C \tag{5.1}$$

$$H_L = D_W - D_e - T_s - S_b \tag{5.2}$$

The geometric parameters inserted in the software for the discrete features are presented in Table 5.2 as well as a summary of the parameters mentioned above.

Table 5.2: Geometric parameters of the pipes

Cross sectional area, $A[mm^2]$	346.36
Pipe outer diameter, $d_0[mm]$	25
Pipe inner diameter, $d_i[mm]$	20.4
Spacing between vertical pipe, $S_L[m]$	0.4
Concrete cover to the pipes, $c[m]$	0.1
Distance from the bottom slab face, $S_b[m]$	0.5
Longitudinal pipe a distance from the top boundary, $S_l[m]$	1

5.2.3 Material properties

This subsection presents the values adopted for the material properties of the soil, heat carrier fluid, and energy wall. The velocity of the liquid was set to 0.6 m/s and no groundwater flow was considered. Table 5.3 presents the parameters adopted. In the parametric study, the value of the thermal conductivity of the soil will assume values of 1.0, 2.0, and 3.0 W/m.K, the other material parameters are constant and the values assigned to the wall are the same for the slab.

5.2.4 Initial temperature and Boundary conditions

Firstly, for all the analyses, the same constant initial temperature of 17ºC is applied for the wall and soil. As for the boundary conditions, Figure 5.2 presents the boundaries assigned to each part of the model, only the top part of the wall and the exposed part of the wall and slab were set with a temperature boundary condition, a no heat flux conditions were applied to the remaining boundaries.

Table 5.3: Material properties of the wall, soil and heat carrier fluid adopted in the parametric study

	Geostructure	Soil	Heat Carrier Fluid
Porosity $n[-]$	0	0	-
Horizontal hydraulic conductivity, $k_x = k_z[m/s]$	0	0	-
Vertical hydraulic conductivity, $k_y[m/s]$	0	0	-
Bulk volumetric heat capacity, $c\rho[MJm^{-3}K]$	2.25	2.0	4.2
Bulk thermal conductivity, $\lambda[Wm^{-1}K^{-1}]$	2.0	1.0/2.0/3.0	0.6
Bulk density, $\rho[kgm^{-3}]$	2500	2000	1000

Since all simulations performed in the parametric study have a duration of 1095 days (3 years) a set of varying temperatures were considered for the temperature boundary conditions. To each, a sinusoidal equation was adopted, the main reason for these equations is to make the numerical analysis represent the thermal behaviour of the energy wall for heating (winter) and cooling (summer) demand, which both depend on the external air temperature. Table 5.4 presents the assigned boundary, the temperature range for each boundary, and the sinusoidal equation considered, where d represents the time in days (between 0 and 365).

Table 5.4: Temperature boundary conditions adopted for the parametric study

Location	Boundary	Temperature $[C]$	Equation
Exterior	Top boundary	17 ± 6	$T_{ext}(d) = 17 + 6sin(2\pi d/365)$
Interior	Slab and wall surface	17 ± 3	$T_{int}(d) = 17 + 3sin(2\pi d/365)$
Inlet	Inlet node	17 ± 10	$T_{inlet}(d) = 17 + 10sin(2\pi d/365)$

5.3 Meshing

Taking into consideration the mesh study presented in Chapter 4, the same approach was adopted in the parametric study, three different meshes were considered. The original mesh without 2D and 3D refinement mesh type MI, and since the software is highly sensitive to mesh refinement, the same configuration has mesh type M2 and type M5 were adopted for this study, in the parametric study they are mentioned as MII and MIII respectively. Both of these meshes presented better results in Chapter 4, these values can be observed in Table 5.5 for the three geometries considered for the parametric study. However, when reproducing simulations with mesh type M5 used in Chapter 4, the time that the simulations took were too high, due to the high number of elements, mesh refinement, and time of simulation, therefore, in this part of the study only mesh type M2 was considered.

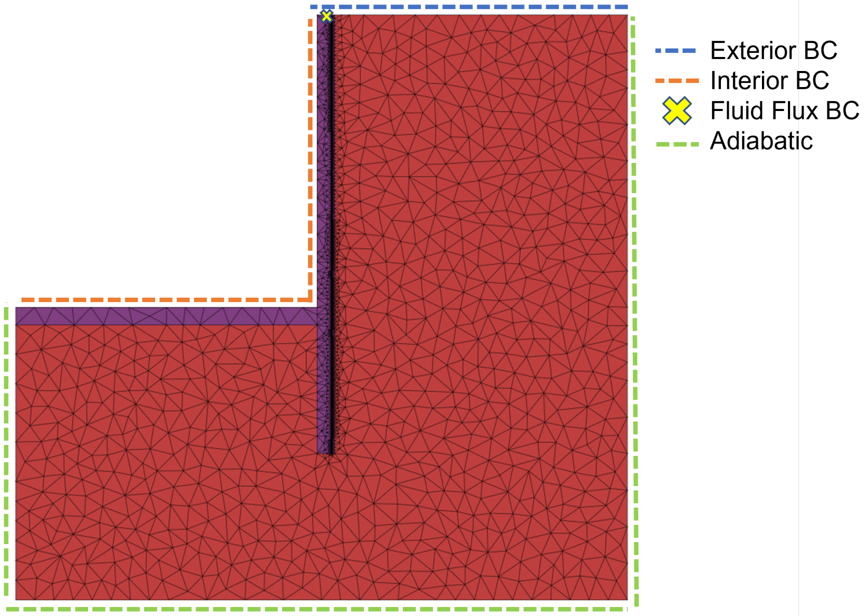

Figure 5.2: Schematic representation of the boundary conditions adopted in the parametric study

Table 5.5: Properties of the meshes used in the parametric study.

Mesh	#Elements	#Nodes	#Nodes per slice	#Slices	Refinement
G10_5-MI	86768	48178	2834	17	Wall and pipe
G20_5-MI	106672	59364	3492	17	Wall and pipe
G30_5-MI	139552	76959	4527	17	Wall and pipe
G10_5-MII	220714	116262	4306	27	Wall and pipe
G20_5-MII	347464	182142	6746	27	Wall and pipe
G30_5-MII	549952	289872	10736	27	Wall and pipe
G20_5-MIII	758320	395158	9638	41	Wall and pipe

5.4 Runs performed

The parametric study will contain several simulations with the parameters presented in the previous sections. Table 5.6 summarises the different combinations that are adopted in this study, the geometry, mesh type, heat exchanger layout, soil thermal conductivity and the case name of the simulation are presented. In the case name column, G1, G2 and G3 stand for G10_5, G20_5 and G30_5.

Table 5.6: Cases performed in the parametric study

Geometry	Mesh Type	Heat Exchanger Layout	Thermal Conductivity of the soil, $\lambda [W/m/K]$	Case Name
G1	MI	L1	1.0	G1_MI_L1_1.0
			2.0	G1_MI_L1_2.0
			3.0	G1_MI_L1_3.0
		L2	1.0	G1_MI_L2_1.0
			2.0	G1_MI_L2_2.0
			3.0	G1_MI_L2_3.0
	MII	L1	1.0	G1_MII_L1_1.0
			2.0	G1_MII_L1_2.0
			3.0	G1_MII_L1_3.0
		L2	1.0	G1_MII_L2_1.0
			2.0	G1_MII_L2_2.0
			3.0	G1_MII_L2_3.0
G2	MI	L1	1.0	G2_MI_L1_1.0
			2.0	G2_MI_L1_2.0
			3.0	G2_MI_L1_3.0
		L2	1.0	G2_MI_L2_1.0
			2.0	G2_MI_L2_2.0
			3.0	G2_MI_L2_3.0
	MII	L1	1.0	G2_MII_L1_1.0
			2.0	G2_MII_L1_2.0
			3.0	G2_MII_L1_3.0
		L2	1.0	G2_MII_L2_1.0
			2.0	G2_MII_L2_2.0
			3.0	G2_MII_L2_3.0
G3	MI	L1	1.0	G3_MI_L1_1.0
			2.0	G3_MI_L1_2.0
			3.0	G3_MI_L1_3.0
		L2	1.0	G3_MI_L2_1.0
			2.0	G3_MI_L2_2.0
			3.0	G3_MI_L2_3.0
	MII	L1	1.0	G3_MII_L1_1.0
			2.0	G3_MII_L1_2.0
			3.0	G3_MII_L1_3.0
		L2	1.0	G3_MII_L2_1.0
			2.0	G3_MII_L2_2.0
			3.0	G3_MII_L2_3.0

5.5 Results and discussion

The results of simulations regarding the performance of the meshes and parameters are discussed and presented in the following subsections.

5.5.1 Influence of the mesh

Considering Table 5.6, the simulations used in this subsection to perform the mesh influence adopted the heat exchanger layout L1 and constant soil thermal conductivity of 2 $[W/mK]$. As expected, the values obtained for both meshes were different and with a considerable discrepancy. Figure 5.3 presents the results for the third year of simulation (from 730 days to 1095 days), in terms of heat transfer rate. Mesh type MII gave lower heat exchange values when compared to mesh type MI, in order to study these results the peak values for summer (cooling) and winter (heating) seasons were considered.

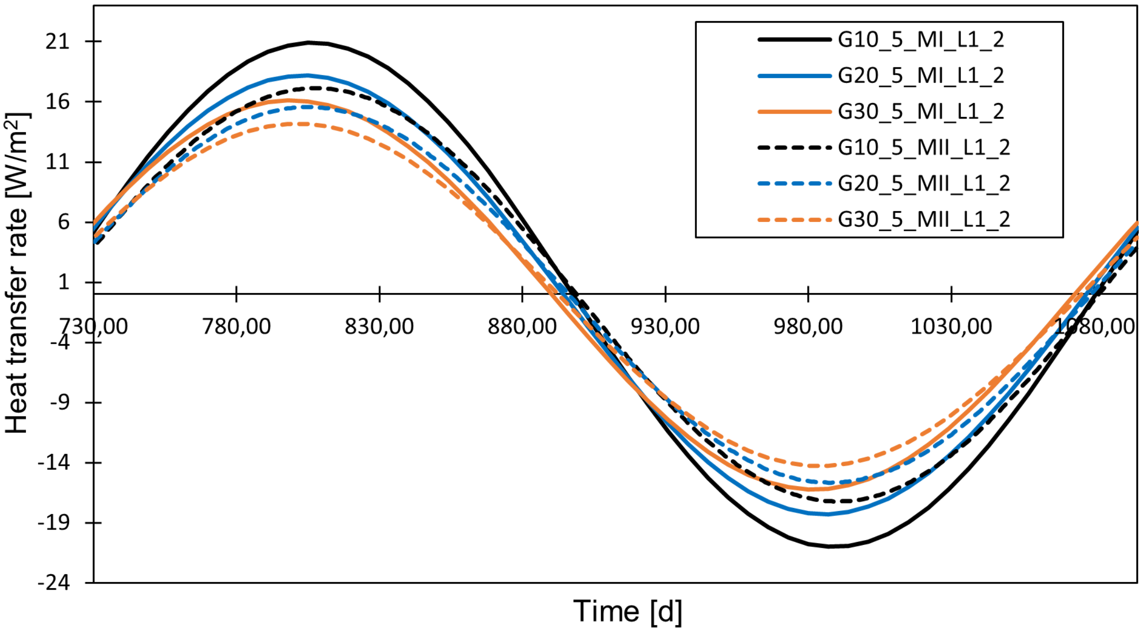

Figure 5.3: Heat transfer rate evolution for the third year of simulation for mesh type MI and mesh type MII

Considering the different meshes and geometries adopted the peak may vary with a range of 1 to 10 days. The peak values for heating and cooling are presented in Figure 5.4 for the three geometries in study. For cooling (summer) conditions a decrease of heat transfer rate is verified for each geometry, 21.9%, 16.7% and 14%, for heating (winter) properties the same behaviour was verified, 21.9%, 16.8% and 13.9% was verified to geometries G1, G2 and G3, respectively. The geometry with less excavation depth presented a bigger discrepancy of the values when compared to the others, a possibility for this outcome is that a greater excavation depth leads to a greater exposure to the exterior space boundary, which can lead to a stabilization of the values. The difference between cooling and heating is not significant, but considering the values obtained the following parameters studied the mesh type MII was adopted, in the subsequent analyses.

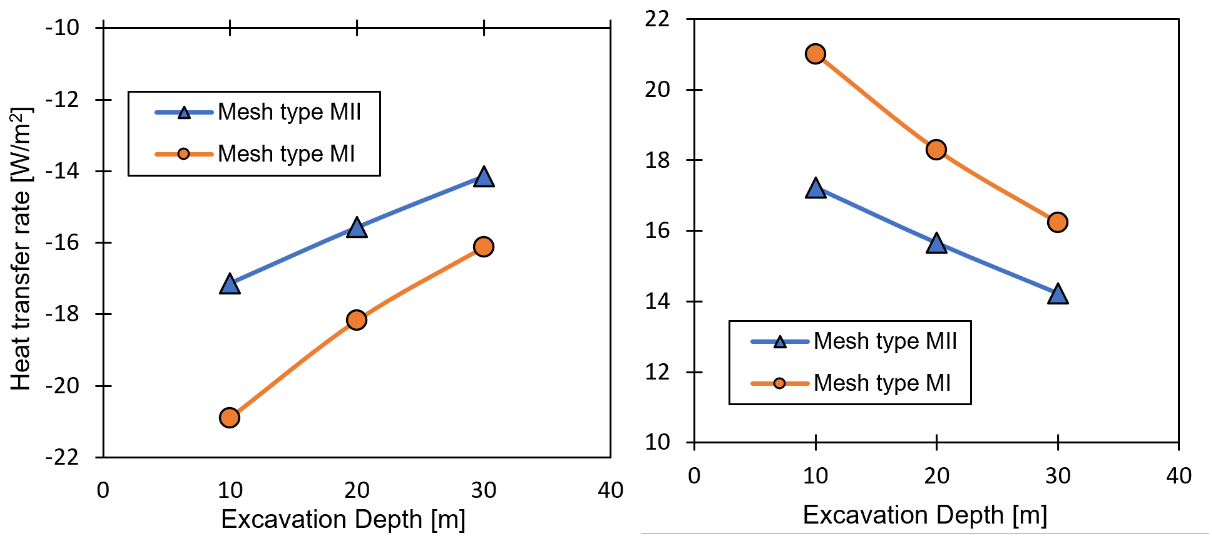

Figure 5.4: Heat transfer rate evolution for the peak values of heating (left) and cooling (right) for third year of simulation for mesh type MI and mesh type MII

5.5.2 Influence of the heat exchanger pipe

Adopting the configurations presented in Figure 5.1 and the geometries presented in Table 5.1, the influence of the heat exchanger pipe was studied. Figure 5.5, presents the evolution of the heat transfer rate for the third year of simulation and Figure 5.6 the results for the peak values for heating and cooling. Due to a high simulation duration the simulations regarding geometry 30_5 were not performed. Both pipe configurations were adopted for each geometry with the same thermal conductivity of the soil, and therefore, it was possible to calculate the difference between results.

For the geometry G10_5, an increase of 4.2%, 6.3%, and 7.9% (heating and cooling) from pipe configuration L1 to L2 was verified for a soil thermal conductivity of 1.0, 2.0 and 3.0$[W/mK]$, respectively. For geometry G20_5 an increase of 3%, 4.6%, and 5.8% (heating and cooling) was observed for the same thermal conductivities 1.0, 2.0 and 3.0$[W/mK]$. In general, the values for heat transfer rate for heat exchanger layout L2, presented higher values when compared to L1, also, when geometry G20_5 was performed the increase was slightly lower when compared to geometry G10_5. In addition, as expected the values obtained for higher soil thermal conductivity presented a higher increase since the fluid spends more time inside the tubes.

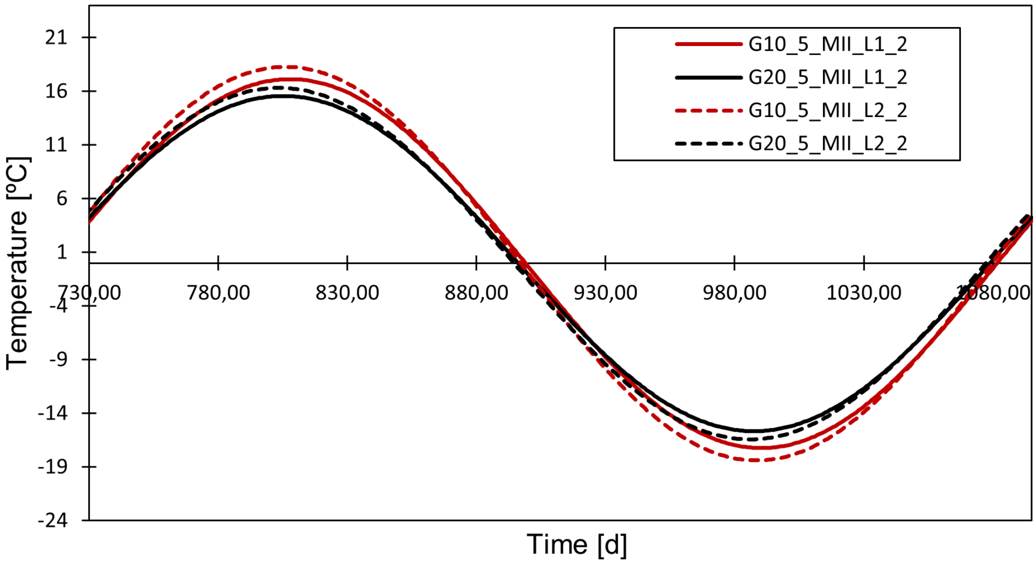

Figure 5.5: Heat transfer rate evolution for the third year of simulation for heat exchanger layout L1 and L2

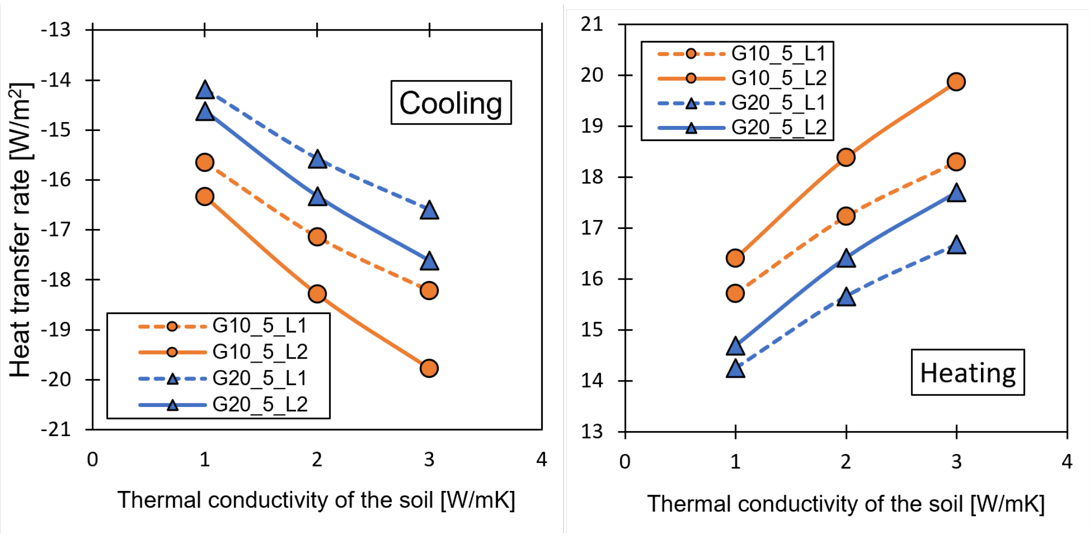

Figure 5.6: Heat transfer rate for the peak values of the third year of the simulation for heat exchanger layout L1 and L2

5.5.3 Influence of the thermal conductivity of the soil

The parametric study considered the study of parameters that may influence the performance of diaphragm walls. Therefore, as mentioned before, to study the impact of the soil's thermal conductivity a set of varying values were adopted, 1.0$[W/mK]$, 2.0$[W/mK]$ and 3.0$[W/mK]$ with geometries G10_5, G20_5 and G30_5. Similarly to Section 5.5.1, to study the impact of the parameters the peak values for heating (winter) and cooling (summer) in the final year of simulation were compared. Additionally, these simulations were performed for heat exchanger layout L1 and L2. As for configuration L1, it was possible to obtain Figure 5.7, which translates the values obtained for heat transfer rate for the peak values, with the varying soil thermal conductivity and wall geometries mentioned above. As expected, for a higher soil thermal conductivity a higher value of heat transfer rate was verified, it is possible to observe an almost linear increase.

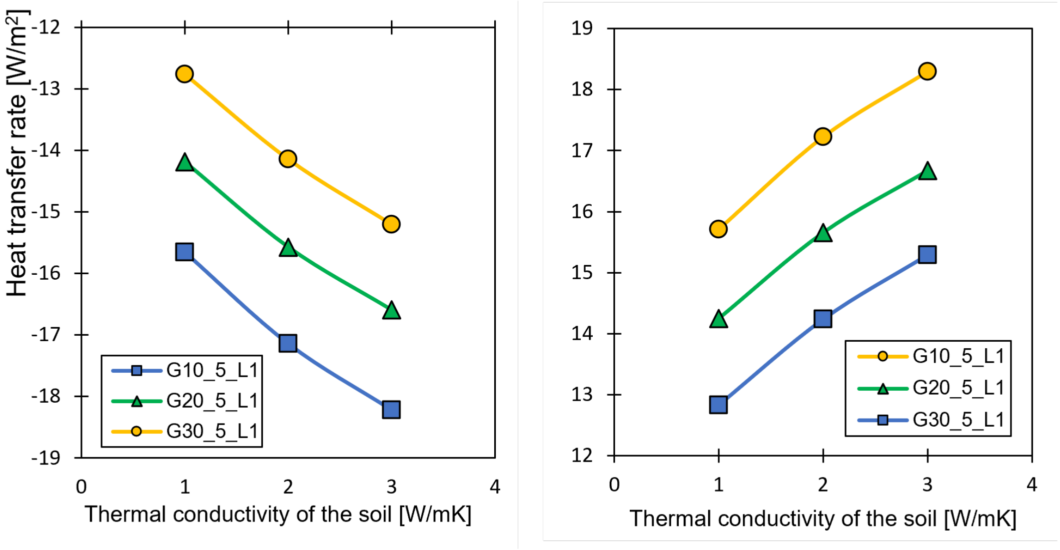

Figure 5.7: Heat transfer rate for the peak values of the third year of the simulation for the different thermal conductivities and heat exchanger layout 1

Taking the simulations with soil thermal conductivity equal to 1.0 $[W/mK]$, when this value is increased to 2.0 $[W/mK]$, for cooling (summer) geometries G10_5, G20_5, and G30_5 presented an increase of 8.7%, 8.9%, and 9.8% respectively and for heating (winter), the same geometries present a similar increase, 8.8%, 9%, and 9.9%, respectively. For the increase of 50% of the soil thermal conductivity, 2.0 $[W/mK]$ to 3.0 $[W/mK]$, an increase in heat transfer rate of 5.9%, 6.1%, and 7% (cooling) and 5.9%, 6.1%, and 6.9% (heating) is verified for G10_5, G20_5 and G30_5 respectively. However, as mentioned before for pipe configuration L2 due to computational requirements, simulations with wall geometry G30_5 were not performed. Therefore, Figure 5.8 only presents values for G10_5 and G20_5. The values for thermal conductivity increase from 1.0 $[W/mK]$ to 2.0 $[W/mK]$ presented an increase of 10.7% and 10.4% (cooling), and of 10.8% and 10.5% (heating) for geometries G10_5 and G20_5 respectively. For 2.0 $[W/mK]$ to 3.0 $[W/mK]$, this increase translate into 7.5% and 7.3% (heating and cooling) for G10_5 and G20_5. It can be recognized that the variation of the peak values obtained with the pipe configuration L2 was slightly higher, which can conclude that if the water spends more time in the tubes, the thermal conductivity of the soil has a bigger impact.

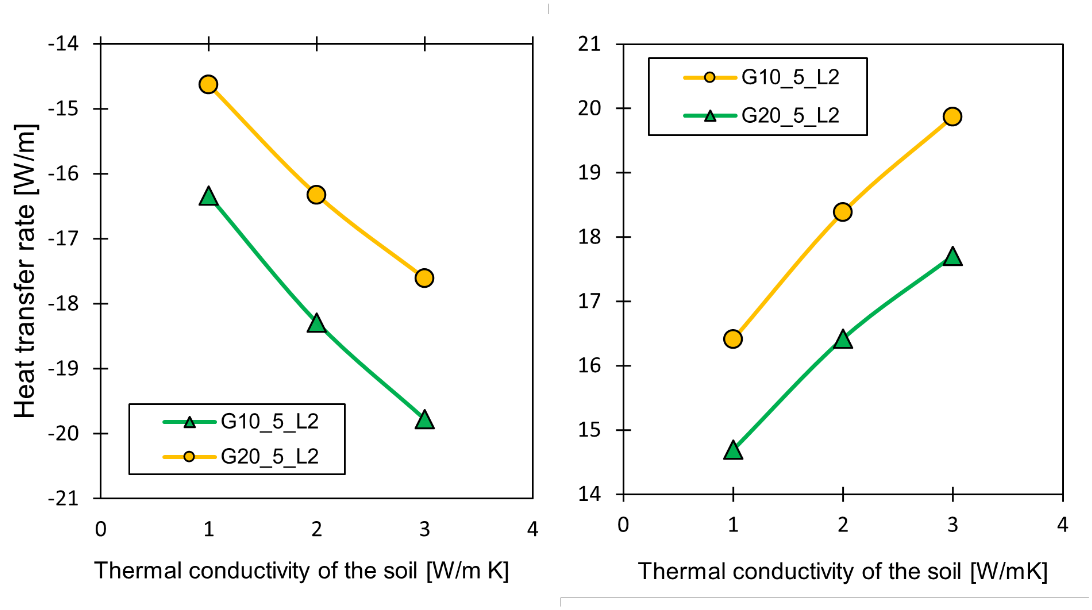

Figure 5.8: Heat transfer rate for the peak values of the third year of the simulation for the different thermal conductivities and heat exchanger layout 2

5.5.4 Influence of the thermal conductivity of the wall and soil together

Several authors present studies where the conductivity of the concrete is one of the most important parameters regarding energy walls (Di Donna, 2017; Di Donna, 2021). A baseline value of concrete thermal conductivity of 2.0 $[W/mK]$ has been used previously and here values of 1.0, 2.0, and 3.0$[W/mK]$ were utilised. In Figure 5.9, the results (coloured lines) are compared to the analyses where only the soil thermal conductivity was varied (black lines), and as the cooling values presented no significant differences when compared to the heating, the same conclusions can be made. Upon analyzing the chart, it can be observed a huge impact for the decrease of thermal conductivity of the wall from 2.0 $[W/mK]$ to 1.0 $[W/mK]$ and heat exchanger layout L1, a decrease of 59%, 54% and 46% was observed for geometries G10_5, G20_5, and G30_5 respectively.

As for, the increase of the thermal conductivity of the wall from 2 $[W/mK]$ to 3 $[W/mK]$ an increase of 24%, 22%, and 20% for geometries G10_5, G20_5, and G30_5, respectively, for heat exchanger layout L2, the variation presented approximately the same range.

The variation of the values obtained for thermal conductivity of 1.0$[W/mK]$ presented to be extremely impactful, however for thermal conductivity of 3.0$[W/mK]$ the values presented to be significant as well. One important relation was found, less excavation depth leads to a higher influence on the results, which means less wall length and less time that fluid spends inside the exchanger pipes.

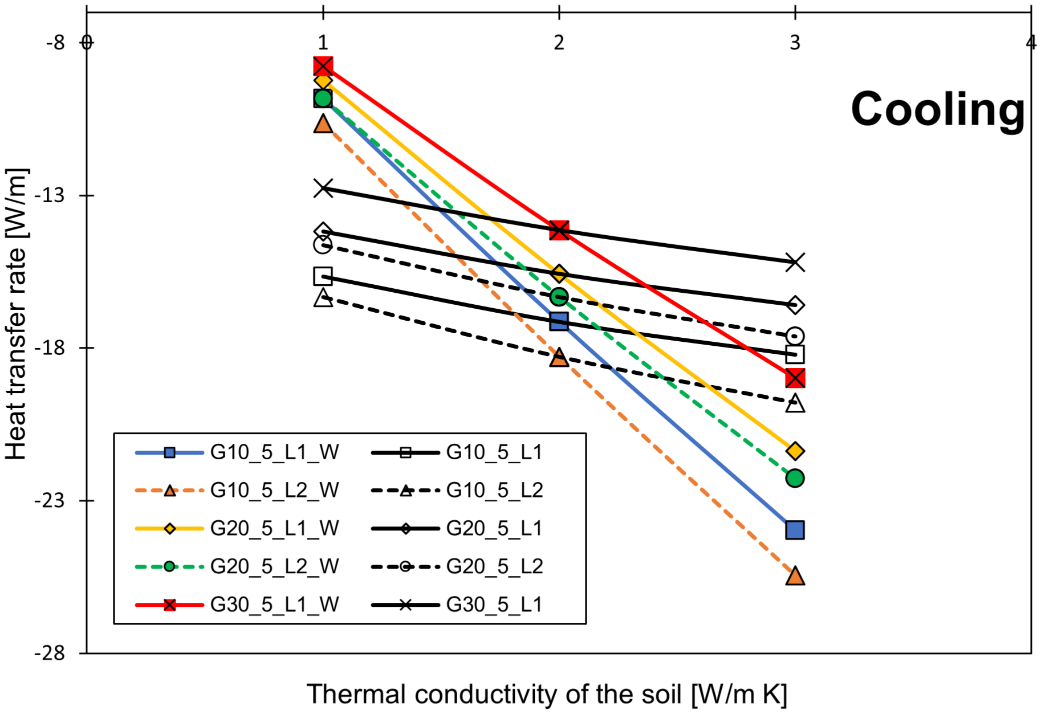

Figure 5.9: Heat transfer rate for the peak values of the third year of the simulation for the different thermal conductivities of the wall

5.5.5 Influence of the wall geometry

To assess the impact of the geometry in the thermal performance of the diaphragm wall, a new set of simulations was performed. For each of them, mesh type MII is used as well as the heat exchanger layout L1, for soil and wall thermal conductivity a constant value of 2 $[W/m/K]$ is established. The aim was to reproduce different model configurations in order to understand the impact of each parameter, wall thickness T_w, and ratio between excavation depth and buried depth (De/Db) are studied. Therefore, values for T_w of 0.6$[m]$, 0.9$[m]$ and 1.2$[m]$ were used, and for De/Db values of 0, 1, 2, 4, 6 and infinite were considered. Table 5.7 presents the new geometries and their specifications for excavation depth (D_e), buried depth (D_b), ratio between excavation depth and buried depth studied (De/Db), wall surface area (A_w) and wall thickness (T_w).

Table 5.7: Properties of the geometries adopted in the parametric study

Case name	Excavation Depth	Buried Depth	Ratio	Wall surface area	Wall thickness
-	$D_e[m]$	$D_b[m]$	D_e/D_b	$A_w[m^2]$	$T_w[m]$
G10_0_0.6	10	0	INF	16	0.6
G0_10_0.6	0	10	0	16	0.6
G10_5_0.6	10	5	2	24	0.6
G10_10_0.6	10	10	1	32	0.6
G16_4_0.6	16	4	4	32	0.6
G20_0_0.6	20	0	INF	32	0.6
G0_25_0.6	0	25	0	40	0.6
G20_10_0.6	20	10	2	48	0.6
G20_0_0.9	20	0	0	32	0.9
G16_4_0.9	16	4	4	32	0.9
G20_5_0.9	20	5	4	40	0.9
G20_10_0.9	20	10	2	48	0.9
G10_10_0.9	10	10	1	32	0.9
G30_5_1.2	30	5	6	56	1.2
G28_7_1.2	28	7	4	56	1.2
G20_0_1.2	20	0	INF	32	1.2
G0_25_1.2	0	25	0	40	1.2

The results are presented in Figure 5.10, to which trend lines for each value of T_w were inserted for each thickness, to represent the results obtained for De/Db=infinity the value of 10 was adopted. As expected, the values for wall thickness of 1.2$[m]$, lead to a greater distance between the heat exchange pipes and the interior boundary condition, therefore, less variation and lower values for heat exchanger rate when compared to thicknesses of 0.6$[m]$ and 0.9$[m]$ are verified. For T_w=1.2m the difference between De/Db=1 to De/Db=Infinite presented a value of only 1.3%. For geometries with higher De/Db ratio, a higher heat exchanger rate was verified, since greater ratios led to a higher exposure of the wall to the interior space boundary. Regarding the T_w=0.9$[m]$, a smaller wall thickness led to higher heat exchanger rate values, the same relations mentioned above were verified. However, a larger increase was verified when comparing lower De/Db ratio with higher values, the difference between De/Db=1 to De/Db=Infinite was 8.1% . For the smallest wall thickness, the dissimilarity between heat exchange values as a function of De/Db was further accentuated, values with less exposure to the interior space (De/Db) presented lower heat transfer rate, nevertheless, for the other De/Db relations, the amount of heat transferred is higher when compared to the other thicknesses.

Figure 5.10 presents the exchanged power, Q$[W]$ and temperature gradient, [ºC], for both geometries at the middle of the wall for the peak day at summer season. As mentioned before, the values of heat transfer rate for winter and summer do not present any major differences. Therefore, at this precise time the values for inlet temperature, top boundary condition and interior space boundary condition are 27ºC, 23ºC and 20ºC, respectively.

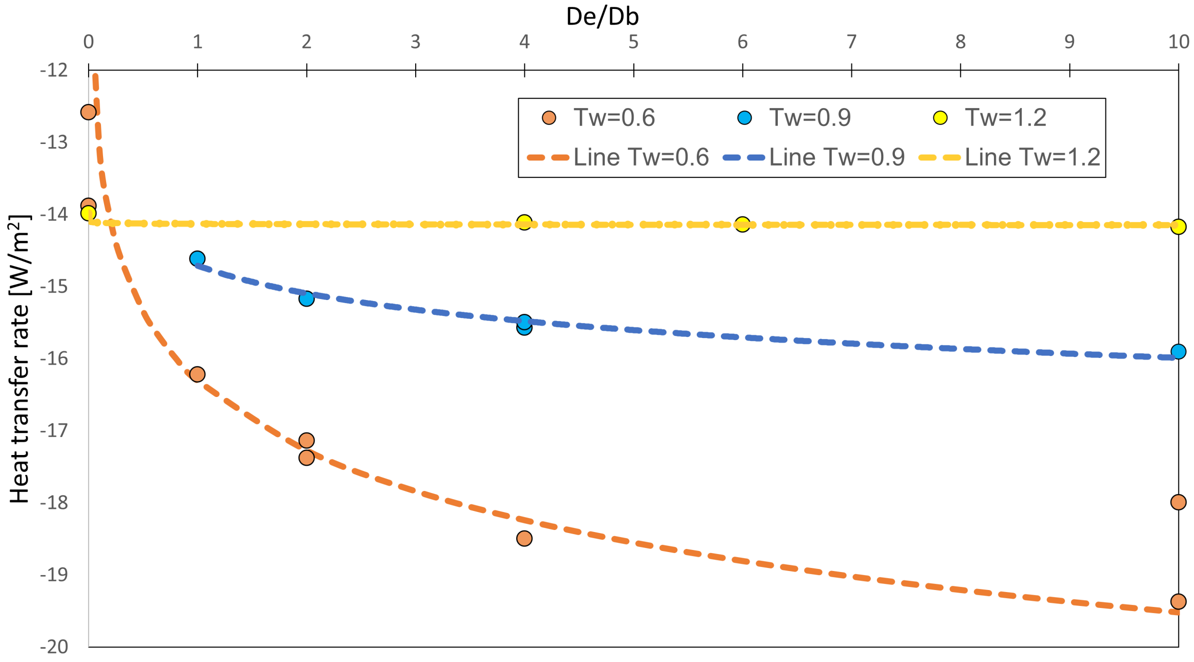

Figure 5.10: Effect of the different wall geometries in the heat exchanger rate.

Figure 5.11 represents screen shots of heat flow field for Case G10_0 (a) and G20_0 (b). For this plots, the coloured marks represent the heal flow (W) at each node which depends on the adjacent elements size. The interior boundary the marks are in the green-light blue range for G10_0, and represent lower heat flow values than case G20_0 (light blue and dark blue), Figure 5.11. The arrows added to the figure illustrate the direction of the heat flow at the boundaries, i.e. into the soil from the top surface and from the wall to the interior space. This is consistent with the temperature fields shown in Figure 5.12 (a) and (b). Comparing the temperature fields for the two cases, it appears that the ground is warmer, further from the pipes to the soil and thus, would help explain the reduced heat exchanged. It is not entirely clear why the heat exchange to the interior is reduced but it may be due to a general warming of the wall section as well as the soil, and reduced thermal gradients in this direction as well.

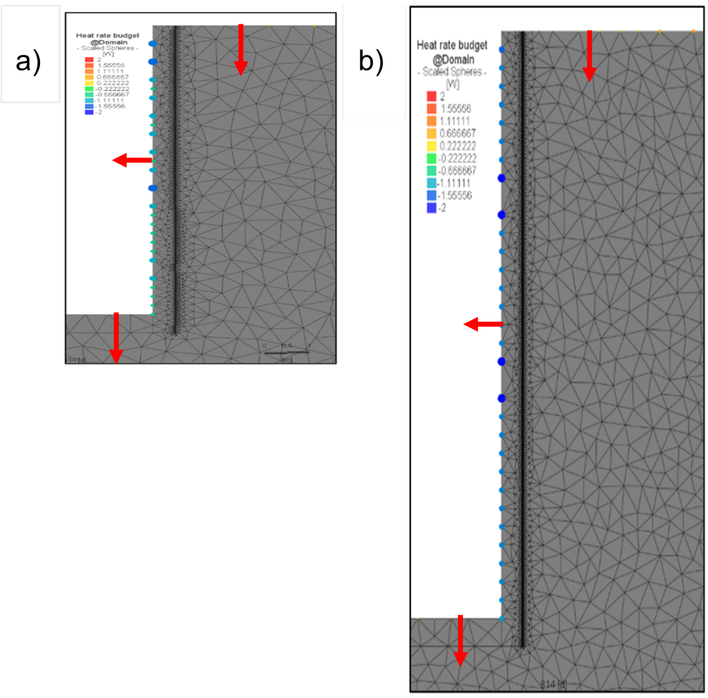

Figure 5.11: Heat transfer rate for geometry: G10_0 (a) and G20_0 (b)

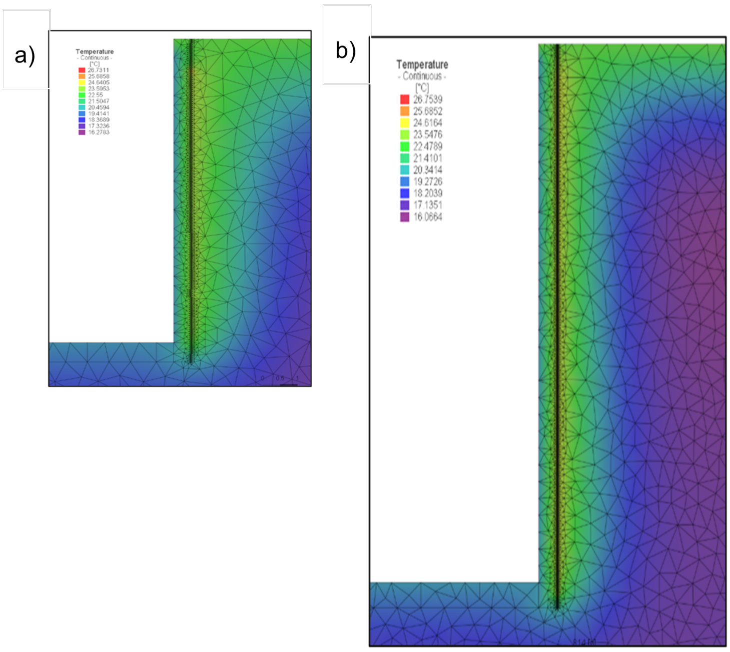

Figure 5.12: Temperature gradient for geometry: G10_0 (a) and G20_0 (b)

Chapter 6

6.1 Conclusions and future developments

The objective of the research presented in this thesis was to assess the thermal performance of energy diaphragm walls thorough numerical analysis using the finite element software FEFLOW provided by DHI. The interest in this energy geostructure is recent, which means that there is a considerable lack of field, laboratory and numerical studies.

In a extensive literature review, it was possible to highlight the different types of geothermal energy, SGE and DGE, the ways to extract them and the most recent devices used. Subsequently, the comparison between energy walls and other energy geostructures was performed, a brief characterization of the operation modes of these foundation elements was presented. Considering the work of several authors a brief summary regarding the study of field, numerical and laboratory studies was outlined and considering the most recent studies a set of numerical analyses was planned to understand the impact of certain parameters. The mesh when performing 3D modelling, the use of different heat exchanger layouts, soil thermal conductivity, wall thermal conductivity and the wall geometry. Therefore:

- The meshes with more nodes, elements and symmetrical characteristics (three-dimensional configuration needs to present a similar presentation with the two-dimensional mesh) presented more precision in the results, a difference of only 1.4% was verified between the finer and more complex meshes.

- When working with meshes with a higher number of elements, more time is requires to run the simulations;

- Heat exchanger layouts presented that for the pipes with more tube the fluid spent more time inside the wall and that leads to a higher temperature output when compared to other pipe configurations with less pipe tubing.

- The soil thermal conductivity presented to be a significant parameter regarding energy diaphragm walls, an average increase of 10.6% between 1.0$[W/mK]$ and 2.0$[W/mK]$ and 7.4% between 2.0$[W/mK]$ and 3.0$[W/mK]$;

- Changing the concrete thermal conductivity affects the heat transfer rate in a considerable way, where an average increase of 54% between 1.0$[W/mK]$ and 2.0$[W/mK]$ and 22% between 2.0$[W/mK]$ and 3.0$[W/mK]$;
- The wall geometry, presented that the energy walls with higher ratio between excavated depth and panel depth (De/Db) provide an increase of heat transfer rate. This parameter presented a relation with the thickness of the wall, for higher thicknesses the ratio De/Db was less predominant when compared to thinner walls. For geometries adopting total exposure to the interior space (zero embedment, Db-De=0), the deepest walls presented higher values of heat exchanger rate since there is a higher wall area. The difference between De/Db for total exposure and total embedment of the wall for higher thicknesses was near 1%, however, for smallest thickness presented in this study an increase of 34% was verified. For the walls fully embedded on the soil, the values presented a similar difference in percentage when compared to the total exposured.

Additionally, thermo-mechanical 3D analysis are still not that common since there is the need of too much time to perform the simulations. In this thesis several meshes were too refined and too complex, some simulations were not possible to perform therefore, additional studies should be performed in this field.

Subsequently, considering the results presented above, future work should be developed regarding the parameters studied:

- A different set of boundary conditions should be considered to represent the different annual temperatures of other countries to understand the behavior of parameter in long-term analyses;
- A variation of the initial temperature of the soil and wall should be considered, this study presented a maximum of three different temperatures per run. Therefore, a more complex temperature layout should be foreseen for future models;
- A study regarding different positions of heat exchanger pipes within the wall should also be included as well as the fluid velocity.
- The entirety of this thesis, the interior space of the wall is not modelled, since this is a simplification to facilitate the computational needs however, some works presented in the literature presented the air modulation and a difference is verified.

Lastly, a full economical study of the energy wall is a necessary step to increase the deployment of this infrastructure therefore, an interaction between material and cost to ensure viability from both thermal and structural behavior.

Bibliography

Agemar T, Weber J and Schulz R (2014). Deep geothermal energy production in Germany, *Energies* **7**(7), 4397–4416.

Angelotti A and Sterpi D (2018). On the performance of energy walls by monitoring assessment and numerical modelling: a case in Italy, *Environmental Geotechnics* **7**(4), 266–273.

Banks D (2012). *An introduction to thermogeology: ground source heating and cooling*, John Wiley & Sons.

Barla M, Di Donna A and Santi A (2020). Energy and mechanical aspects on the thermal activation of diaphragm walls for heating and cooling, *Renewable Energy* **147**, 2654–2663.

Brandl H (2006). Energy foundations and other thermo-active ground structures, *Géotechnique* **56**(2), 81–122.

Chen B, Huang Y, Ye W, Cui Y and Xu Z (2018). Investigation on the Thermal Conductivity of Shanghai Soft Clay, *in GeoShanghai International Conference*, Springer, pp. 984–992.

Côté J and Konrad J M (2005). A generalized thermal conductivity model for soils and construction materials, *Canadian Geotechnical Journal* **42**(2), 443–458.

Di Donna A, Cecinato F, Loveridge F and Barla M (2017). Energy performance of diaphragm walls used as heat exchangers, *Proceedings of the Institution of Civil Engineers-Geotechnical Engineering* **170**(3), 232–245.

Di Donna A, Loveridge F, Piemontese M and Barla M (2021). The role of ground conditions on the heat exchange potential of energy walls, *Geomechanics for Energy and the Environment* **25**, 100199.

Dong S, Li X, Tang A M, Pereira J M, Nguyen V T, Che P and Xiong Z (2019). Thermo-mechanical behavior of energy diaphragm wall: Physical and numerical modelling, *Applied Thermal Engineering* **146**, 243–251.

Huo J S, Chen J, Gong Q M and Zhou S H (2011). Study on the deformation of retaining structure of pit-in-pit excavation, *in Advanced Materials Research*, Vol. 243, Trans Tech Publ, pp. 2903–2908.

Johansen O (1975). Varmeledningsevne av jordarter (Thermal conductivity of soils), *CRREL Draft English Translation* **637**.

Laloui L and Loria A F R (2019). *Analysis and design of energy geostructures: theoretical essentials and practical application*, Academic Press.

Makasis N and Narsilio G A (2020). Energy diaphragm wall thermal design: The effects of pipe configuration and spacing, *Renewable Energy* **154**, 476–487.

Makasis N, Narsilio G A, Bidarmaghz A, Johnston I W and Zhong Y (2020). The importance of boundary conditions on the modelling of energy retaining walls, *Computers and Geotechnics* **120**, 103399.

Rees S (2016). *Advances in ground-source heat pump systems*, Woodhead Publishing.

Rees S, Adjali M, Zhou Z, Davies M and Thomas H (2000). Ground heat transfer effects on the thermal performance of earth-contact structures, *Renewable and Sustainable Energy Reviews* **4**(3), 213–265.

Sailer E (2020), Numerical modelling of thermo-active retaining walls, PhD thesis, PhD thesis. Imperial College London.

Silva D (2020), Use of Retaining Walls in Shallow Geothermal Energy Systems, PhD thesis, MsC thesis. Instituto Superior Técnico.

Sun M, Xia C and Zhang G (2013). Heat transfer model and design method for geothermal heat exchange tubes in diaphragm walls, *Energy and buildings* **61**, 250–259.

Tatro S B (2006). Thermal properties, *in Significance of tests and properties of concrete and concrete-making materials*, ASTM International.

Wu D, Liu H, Kong G and Ng C W (2020). Interactions of an energy pile with several traditional piles in a row, *Journal of Geotechnical and Geoenvironmental Engineering* **146**(4), 06020002.

Xia C, Sun M, Zhang G, Xiao S and Zou Y (2012). Experimental study on geothermal heat exchangers buried in diaphragm walls, *Energy and Buildings* **52**, 50–55.

Appendix A

Governing laws for Hagen-Poiseuille

This appendix provides a short summary of the governing equations for mass and heat transfer in the discrete features used in the analyses reported in this thesis. More complete details may be found in Diersch (2014).

Upon considering a discharge through the tube the relation starts to be expressed by the hydraulic radious r_{hydr}, when this value is equal to R/2 the average velocity is given with the following equation:

$$v_z = -[\frac{r^2_{hydr}}{2 * \mu}] * [\frac{d\rho}{dz} - \rho * g_z] \tag{A.1}$$

where v_z is the fluid velocity along z-axis $[m/s]$; μ is the dynamic viscosity of the fluid $[Pa * s]$; ρ fluid density kg/m^3; g_z is the gravity along z-axis $[m/s^2]$; R is the radious of the pipe and r is the radial coordinate. The Hagen-Poiseuille laws for axisymmetric flow can be represented with linear relationships with respect to the pressure gradient and gravity.

When using the FEFLOW software the heat transfer is commonly assumed has a forced convection law. Normal convection is known as a general flow phenomena, where the fluid motion is influenced with fluid density changes. However, when dealing with forced convection the fluid motion is generated by an external force, this leads to a complex method when representing this phenomena. When dealing with a incompressible fluid flow in a pipe, the difference of the inlet and outlet nodes helps to understand a convective heat transfer rate with the following equation:

$$q_{conv} = m * c_p(T_o - T_i) \tag{A.2}$$

where m is the mass flow rate [kg/s]; c_p is the fluid specific heat capacity at constant pressure; the outlet temperature is given by T_o in [K] and the inlet temperature T_i in [K].